# THE WHEEL-RAIL CONTACT PROBLEM IN VEHICLE DYNAMIC SIMULATION

## MODELING OF TRAIN-TURNOUT INTERACTION

# THE WHEEL-RAIL CONTACT PROBLEM IN VEHICLE DYNAMIC SIMULATION

MODELING OF TRAIN-TURNOUT INTERACTION

**Proefschrift**

ter verkrijging van de graad van doctor
aan de Technische Universiteit Delft,
op gezag van de Rector Magnificus prof. ir. K.C.A.M. Luyben,
voorzitter van het College voor Promoties,
in het openbaar te verdedigen op dinsdag 5 januari 2016 om 10:00 uur

door

**Nico BURGELMAN**

Burgerlijk werktuigkundig ingenieur, Universiteit Gent, België
MSc. Solid and fluid mechanics, Chalmers University of Technology, Sweden
geboren te Gent, België.

Dit proefschrift is goedgekeurd door de:

promotor: Prof. dr. R.P.J.B. Dollevoet
copromotor: Dr. Z. Li

Samenstelling promotiecommissie:

| | |
|---|---|
| Rector Magnificus, | voorzitter |
| Prof. dr. ir. R.P.J.B. Dollevoet, | Technische Universiteit Delft |
| Dr. Z. Li, | Technische Universiteit Delft |
| *Onafhankelijke leden:* | |
| Prof. S. Iwnicki | University of Huddersfield |
| Dr. I.Y. Shevtsov | ProRail |
| Dr.ir. A.L. Schwab | Technische Universiteit Delft |
| Prof.dr.ir. D.J. Schipper | Universiteit Twente |
| Prof.dr. A. Scarpas | Technische Universiteit Delft |
| Prof. dr. ir. R.F. Hanssen | Technische Universiteit Delft, reservelid |

This dissertation was supported by:

TU Delft Delft University of Technology ProRail

*Keywords:* Railways, Wheel/rail Contact, Vehicle Dynamics, Non-Elliptical Contact Models, Turnouts

*Printed by:* CPI Koninklijke Wöhrmann

*Cover:* Front: The local slip in the contact area calculated with the FastSim method & Back: a visualization of the wheel profile and the contact locus



ISBN 978-94-6203-976-6

An electronic version of this dissertation is available at
http://repository.tudelft.nl/.

*For science, for technology and last but not least, for better railway systems.*

Nico Burgelman

# SUMMARY

One of the major costs incurred by railway companies is the maintenance of turnouts. This situation occurs because the large dynamic forces between the wheels of a train and the rails of a turnout cause excessive wear, rolling contact fatigue and rapid degradation of other components. A thorough understanding of the dynamic interaction between a train and a turnout could lead to a better design of the vehicle and track structures, deeper insight into the damage mechanisms and subsequently to smarter maintenance planning.

To properly model the interaction between a train and a turnout, three important issues need to be considered:

1. Track flexibility: The rails, the fastening, the sleepers and the ballast are not rigid but can move and absorb or transmit vibrations. This factor is especially relevant when impact between the wheel and the rail occurs, which is always the case in a turnout.

2. Wheel/rail contact: In a turnout the rail geometry is complex at the switch blade and at the frog. Therefore, some of the assumptions commonly made in contact models used in vehicle dynamic software are no longer valid when considering those contacts.

3. Effect of train coupling: In a turnout the forces acting between the vehicles through the couplers have a significant effect on the vehicle dynamics. This is especially true when traction or braking is considered.

The first issue has been extensively covered in the literature, and flexible track models are available in modern commercial software for vehicle dynamic simulation. Therefore, the issue is not further investigated in this dissertation.

The second issue can be approached in two ways. One can use contact models online for the vehicle simulation, which are advanced while still being fast and robust. Alternatively, one can use a simple contact method to evaluate the contact forces online during the vehicle simulation. Then, a more sophisticated method can be employed offline resolving the contact problems and obtaining a more accurate estimate of the local stress and slip distribution in the contact area. In the latter case, the balance of forces is not necessarily fulfilled as the contact force calculated with the more advanced method are not coupled back to the vehicle dynamic simulation; therefore generating an error. This error from the offline approach is investigated in this thesis for the determination of the contact point location and for the calculation of the tangential contact forces. A fast analytical method for calculating the longitudinal contact location was validated, but the effect of the contact point location on the wheelset's yaw angle was found to be negligible.

To quantify the effect of different solution methods of the tangential contact forces, we compared four models: FastSim (the reference model, currently used most often in multibody simulations) and three non-elliptical models based on interpenetration: Kik-Piotrowski, Linder and Stripes. These models were applied in a co-simulation between the vehicle dynamic software and Matlab, simulating hunting motion and steady curving. It was concluded that the interpenetration methods predict a better curving behaviour (lower creepages and lower creep forces). The simulations performed using the Kik-Piotrowski method resulted in a slightly shorter hunting wavelength.

Although the above-mentioned interpenetration methods are more advanced than FastSim, they still make a number of assumptions that may not be satisfied under some certain contact conditions. Therefore, a new contact method is introduced based on Kalker's full theory with the addition of varying spin creepage. This new method was applied offline in a multibody simulation of a wheel-rail contact in a turnout. The resulting stress and slip distributions were realistic. Moreover, the method converged even in the most difficult contact cases. Thus the method is suitable for online application.

The question regarding how the contact models can be validated through measurements is a difficult one, as the local stress and slip in the contact area cannot be measured directly. Many methods measuring the consequences of the stress and slip in the contact area have been proposed in the literature. One possibility is to measure the energy dissipated in the wheel/rail contact. This dissertation presents and compares several methods calculating the dissipated energy, it then compares the results obtained from vehicle dynamic simulations with measured energy values. It is concluded that although the approach is promising, there is room for improvement for both the simulations and the measurements.

The third issue is especially relevant for long trains with a braking locomotive at the front or a tractive locomotive at the rear. In these configurations the couplers will be compressed. Because of the curvature of the track in a curve or a turnout, there will be a misalignment between the couple and the adjacent carbodies. This misalignment produces an outwards lateral force, which combines with the lateral centripetal force to create a large force on the wheels. The magnitude of this force needs to be below a certain limit for derailment safety. In this dissertation, an existing method for calculating the coupler angles in curves with a constant radius is extended to calculate the coupler angle in curve transients and turnouts. With the knowledge of the coupler angle, quasi-statics can be used to estimate the lateral wheel rail force and thus the risk of derailment. The results obtained from the quasi-static approach are compared to results obtained from vehicle dynamic simulations. This comparison allows for the definition of a dynamic multiplication factor to be applied to the quasi-static results to obtain a first estimate of the dynamic lateral forces. Such a fast method could be useful when a quick and dirty estimate of the derailment risk is required for a non-daily train configuration or in the early stages of a new vehicle/track design.

The analysis of the contact models in this dissertation will help researchers choose between the different models and between implementing the model offline or online. This should enable researchers to accurately model the contact in turnouts so that the deterioration mechanisms underlying the excessive wear and RCF in turnouts can be understood. In turn, this understanding should lead to better maintenance and associated

cost savings.

# SAMENVATTING

Het onderhoud van spoorwissels is een belangrijke kostenpost voor spoorweguitbaters. Dit komt doordat de hoge krachten tussen wielen van de trein en de spoorstaaf in het wissel hoge slijtage en vermoeiing veroorzaken. Een diepgaand inzicht in de dynamische interactie tussen de trein en het wissel kan een beter ontwerp van het wissel mogelijk maken. Ook zorgt een beter inzicht in de dynamische interactie voor een beter begrip van de slijtagemechanismen, wat op zijn beurt weer leidt tot een slimmere onderhoudsplanning.

Om de dynamische interactie tussen trein en wissel accuraat te modelleren moeten de volgende drie factoren in acht genomen worden:

1. de elasticiteit van het spoor: de spoorstaven, de dwarsliggers en het ballastbed kunnen bewegen en zo trillingen absorberen of doorgeven. Dit is zeker van belang als er sprake is van impact tussen het wiel en de spoorstaaf, wat in een wissel altijd het geval is.

2. het wiel/spoorstaafcontact: in een wissel is de spoorstaafgeometrie complex, zowel bij de tong als bij het puntstuk. Hierdoor zijn sommige veronderstellingen die vaak gemaakt worden in de contactmodellen voor voertuigsimulaties niet langer geldig.

3. de invloed van de treinkoppeling: in een wissel hebben de krachten in de koppeling tussen de wagenbakken een significante invloed op de voertuigdynamica. Dit wordt nog belangrijker als ook rekening gehouden wordt met de tractie of het remmen van het voertuig.

Het eerste punt, de elasticiteit van het spoor, is uitvoerig beschreven in de vakliteratuur. Verscheidene modellen voor het modelleren van deze elasticiteit zijn beschikbaar in commerciële software voor voertuigsimulaties. Daarom wordt dit punt niet verder behandeld in dit proefschrift.

Het tweede punt, het wiel/spoorstaafcontact in het wissel, kan op twee manieren benaderd worden. Ofwel wordt een tamelijk geavanceerd contactmodel gebruikt, online in de voertuigsimulatie. Dit contactmodel moet dan snel en robust genoeg zijn. Een tweede benadering bestaat eruit om een voertuigsimulatie te doen met een relatief eenvoudig contactmodel, waarna de contactproblemen opnieuw worden opgelost met een geavanceerd contact model, om zo een betere benadring van de contactspanningen en de locale slip te verkrijgen. In dit geval worden de contactkrachten berekend met het geavanceerde model niet teruggekoppeld naar de voertuigsimulatie, waardoor het krachtenevenwicht niet gegarandeerd wordt. De fout die hierdoor ontstaat werd in dit proefwerk onderzocht voor wat betreft de locatie van het contact punt en voor de berekening van de tangentiële contactkrachten. Er werd een snelle analytische methode voor

de berekening van de locatie van het contact punt gevalideerd door vergelijking met een numerieke methode. Hieruit werd geconcludeerd dat alhoewel de anlytische methode inderdaad een meer accurate locatie van het contact punt vindt, de invloed van de contact locatie op de voertuigsimulatie miniem is.

Om de invloed van het tangentiële contactmodel op de vuirtuigsimulatie te quantificeren werden vier contactmodellen toegepast in een co-simulatie. De modellen waren: FastSim (gebruikt als referentiemodel, tegenwoordig het meest gebruikte model voor voetuigsimulaties) en drie niet-elliptische modellen gebaseerd op interpenetratie: Kik-Piotrowski, Linder and Stripes. In de co-simulatie werd de sinusloop en de passage door een boog gesimuleerd, waarbij VIRail gebruikt voor de voertuigsimulatie en Matlab voor de contactmodellen. De conclusie was dat de interpenetratiemodellen een beter booggedrag simuleren (minder kruip en kleinere kruipkrachten). Het Kik-Piotrowski model voorspelde een iets kortere golflengte van de sinusloop.

Hoewel de bovenvernoemde modelen geavanceerder zijn dan FastSim gaan zij nog steeds uit van een aantal veronderstellingen die geschonden worden in het geval van contact in een wissel. Daarom werd een nieuw contactmodel geïntroduceerd, dat gelijkvormig contact en een variërende rotatiekruip toelaat. Eerst werd een simpel model (FastSIM) gebruikt tijdens de voertuigsimulatie, vervolgens weren alle contactsituaties herberekend met het nieuwe model. De resulterende spanning- en slipverdeling was realistisch, bovendien convergeerde de methode in alle gevallen. Dit laatste is het bewijs dat het model robuust genoeg is om tijdens de voertuigsimulaties gebruikt te worden.

Een empirische validatie van de contactmodellen is moeilijk, omdat de spanning en slipverdeling in het contactoppervlakte niet rechtstreeks gemeten kunnen worden. Daarom zijn er veel methodes ontwikkeld on de gevolgen van de spanning en slip in het contact oppervlak te meten. Een van deze gevolgen is het energieverlies door wrijving in het wiel/spoorstaafcontact. Dit proefschrift presenteert en vergelijkt een aantal methoden om dit energieverlies te berekenen, waarna het berekende energieverlies vergeleken werd met gemeten waarden. De conclusie was dat, alhoewel de methode veelbelovend is, er verbetering nodig is van zowel de inputwaarden van de simulatie, als van de meetmethoden.

Het derde punt, de invloed van de koppeling tussen de wagenbakken, is in het bijzonder relevant voor lange treinen met een duwende locomotief achteraan of een remmende locomotief vooraan. In deze configuraties worden de koppelingen tussen de wagons ingedrukt. In een boog of een wissel ontstaat dan een hoek tussen de koppeling en de aangrenzende wagons. Deze hoek zorgt ervoor dat de drukkrachten in de koppeling bijdragen tot de zijdelingse kracht van de wielen op het spoor. Om het ontsporingsrisico te beperken moet deze zijdelingse kracht onder een bepaald niveau blijven. In dit proefschrift werd een bestaande methode om de koppelingshoek te berekenen in bogen met een constante boogstraal, uitgebreid voor transitiebogen en wissels. Als de koppelingshoek bekend is, kan quasi-statica aangewend worden om de zijdelingse krachten en zo het ontsporingsrisico te berekenen. De resultaten verkregen met de quasi-statica werden vergeleken met resultaten van voertuigsimulaties. Deze vergelijking laat ons toe om een vermenigvuldigingscoëfficiënt te bepalen die kan gebruikt worden met de resultaten van de quasi-statica om een eerste schatting te bekomen van de dynamische zijdelingse krachten. Deze werkwijze kan gebruikt worden om een snelle schatting te krijgen van

het ontsporingsrisico, bijvoorbeeld voor een treinsamenstelling die van de dagelijkse afwijkt of om een eerste schatting te hebben in de eerste fase van een nieuw ontwerp van het train/spoor systeem.

De hier gepresenteerde studie van de contactmodellen zal onderzoekers helpen met die keuze tussen de verschillende contactmodellen. Dit zal onderzoekers toelaten om het contact tussen wiel en spoorstaaf in een wissel correct te modelleren en zo de schademechanismen beter te begrijpen. Dit beter begrip kan bijdragen aan het verminderen van de onderhoudskosten.

# CONTENTS

# 1

# INTRODUCTION

## 1.1. OVERVIEW OF TRACK COMPONENTS

This section introduces basic railway concepts and definitions intended for readers who are not in the field. There are two types of tracks: ballasted track and slab tracks. In Europe, most tracks are ballasted, whereas slab tracks are used mainly in tunnels and for metros. Figure 1.1 shows the main components of a ballasted track [1]:

- The ballast consists of stones with sharp edges. Friction with those edges causes energy dissipation and thereby reduces vibrations/noise of the tracks.
- A sleeper is a beam that serves two purposes: it holds the rails at a predefined distance from each other, ensuring a constant gauge, and it transfers the force from the rails to the ballast stones.
- The fastening system fixes the rails to the sleeper. To do so, the fastening consists of metal clamps, and a rubber pad, called a railpad, between the rail and the sleeper to provide flexibility and damping.
- The rails provide the running surface for the wheels. They have an optimized profile to ensure the wheel runs over them with the lowest amount of wear and resistance possible.
- The wheelset is a rigid construction of two wheels and an axle.

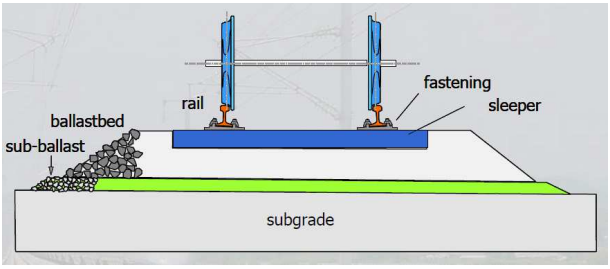


Figure 1.1: The components of a ballasted track [1].

The interface between the wheel and the rail is of special importance. The wheel profile, shown in Figure 1.2, can be divided into the wheel flange, which contacts the rail at the gauge corner in curves or turnouts, and the tread, which contacts the rail top.

## 1.2. MODELLING OF TRAIN-TURNOUT INTERACTION

A turnout (switch and crossing, S&C) is an important part of railway infrastructure. It allows for trains to switch from one track to another. However, to switch between tracks the rails must be interrupted. These discontinuities in the rail are responsible for high impact loads from the wheels on the rail. These high loads cause wear and damage to the turnout. Therefore, the turnout is a maintenance-intensive component for rail infrastructure managers. Not only do the discontinuities cause problems but the geometry of the turnout does not allow for track inclination (cant). Therefore, the centrifugal

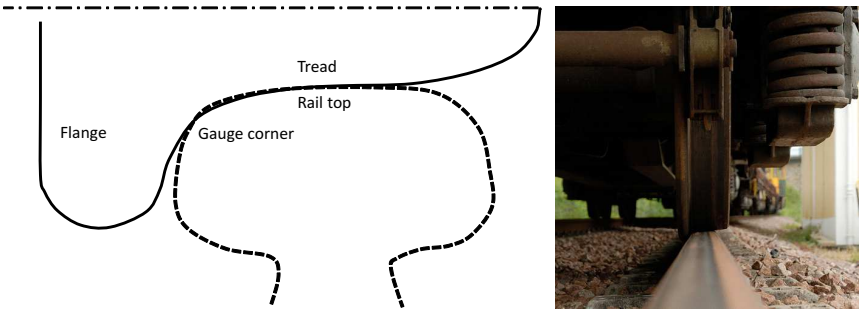


(a) (b)

Figure 1.2: Profiles of a wheel and rail.



force of a train taking the diverging route of a turnout has to be transferred laterally to the track. This behaviour generates high lateral loads on the fastenings of the rail and between the sleepers and the ballast. Moreover, passengers experience this centrifugal force. Therefore, the speed at which a train runs through the turnout is limited.

A few important components of a turnout are shown in Figure 1.3. The switch blade (shown Figure 1.4a), operated by a switching machine transfers the wheels of the train from one rail to another. The rails cross each other at the frog (shown in Figure 1.4b). Here, the rail is discontinuous to make room for the wheel flanges of a train taking the other route to pass. This discontinuity means that the wheels are not supported uniformly at all times; therefore, there is an impact at the discontinuity. The corresponding impact forces are the cause of large extents of material wear and rolling contact fatigue that are often observed at frogs.

A train can pass the turnout along a straight trajectory, called the through route, or take the curve, called the diverging route. This thesis focuses on the simulation of trains taking the diverging route, because in that route the wheel/rail contact forces and corresponding damages are most severe.

Because turnouts are essential to railway networks, they have been studied extensively, both experimentally and by numerical modelling. To date, it hase been impossible to build a numerical model that can cope with all aspects of the vehicle-turnout interaction; therefore, different models that focus on different aspects have been developed. The following key areas can be defined:

- The flexibility of the turnout itself can be modelled by using beam elements in combination with springs, dampers and rigid masses. Alternatively a 3D finite element (FE) model of the entire turnout can be built.
- A train can be modelled as a single vehicle coasting through the turnout or as a train of vehicles, including the interaction between the vehicles through the couplers. Traction and braking can also be included in the analysis
- The wheel rail contact can be modelled using a range of contact models available

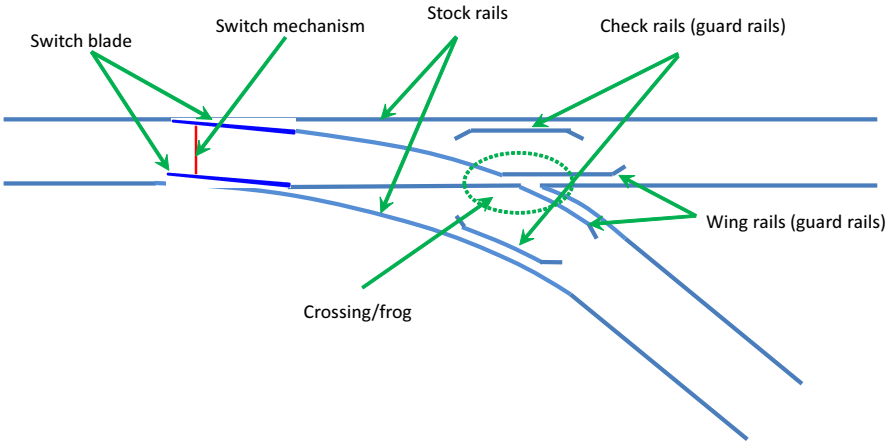


Figure 1.3: The components of a railway turnout.

(a) (b)

Figure 1.4: (a) A switch blade and (b) a crossing nose (or frog).

in the literature, starting from simple but fast and robust models to advanced and accurate but computationally expensive models.

Herein, track flexibility is discussed shortly in Section 1.3. The main focus is on the train-turnout interaction (Section 1.4 and Chapter 6) and on the wheel/rail interface (Section 1.5, and Chapters 4 and 5).

## 1.3. TRACK FLEXIBILITY IN VEHICLE SIMULATIONS

In vehicle dynamic simulations it is common to simulate a vehicle modelled by rigid bodies running over a rigid track. Although this approach is sufficiently accurate for most vehicle simulations, it does not suffice if high dynamic forces between the wheel and the rail are expected. The latter is the case with the wheels of a train switching

from the stock rail to the switch blade in a turnout or when the wheels ride over the frog. Therefore, researchers who have investigated the interaction between trains and turnouts have used a flexible track model. The simplest and most computationally efficient way of modeling a flexible track is by using a co-travelling model for each wheelset [2, 3].

Another way of modelling a flexible track is to model the rails using beam elements supported by spring-damper systems representing the railpads [4]. The sleeper can then be modelled either as a rigid body or by using beam elements whereas the connection between the sleeper and the subsoil is modelled using springs and dampers. This model generates many more degrees of freedom than the co-travelling method, and thereby requires greater computational effort. Therefore, often only a short section of a track around the point of interest is modelled as flexible while the rest of the track is modelled as rigid. The parameters needed in the flexible track model can be obtained through comparison with the eigenmodes of a section of the track using a finite elements model [5].



Both the co-traveling track method and the flexible track section method are currently available through commercial software. An example of the lateral wheel/rail contact force in a turnout obtained through a flexible track method is shown in Figure 1.5.

The most sophisticated option so far for modeling a flexible track is to couple a vehicle dynamic simulation with a full finite element model of the track by co-simulation [6].

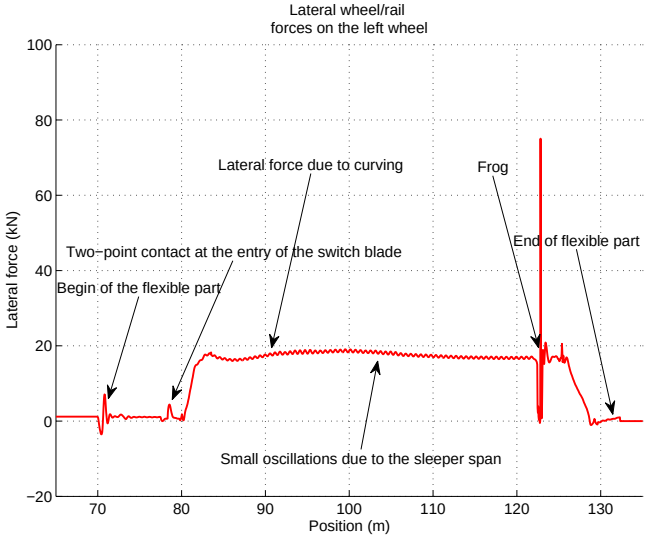


Figure 1.5: The lateral force on the outer wheel of the leading bogie of a vehicle running through a turnout modelled as a flexible track with beam elements [7].

## 1.4. LATERAL FORCES IN THE COUPLING BETWEEN WAGONS

In a train, the motion of one vehicle affects that of the others through the couplers between the vehicles. When a rear-running locomotive brakes or a front-running locomotive applies traction, the longitudinal forces in the couplers will be tensile. When a front-running locomotive brakes or a rear-running locomotive applies traction, the longitudinal forces will be compressive. For a train along a curve, tensile longitudinal forces in the couplers will produces a lateral force in the couplers pulling the vehicles inwards, whereas compress coupler forces will produce a lateral force pushing the vehicles outwards. Trains typically operate with cant deficiency such that inertia pushes the vehicles outwards. This inertia force combines with the lateral force from the couplers and must be carried by the wheels.

The effects of braking and traction on long trains have often been studied from the perspective of longitudinal dynamics [8]. The longitudinal problem can be modelled with just one degree of freedom per vehicle, thereby limiting the computational effort even for long trains. Many authors have published longitudinal coupler models that include non-linear springs, slack and/or friction [9–13]. Others have studied the combination of longitudinal and vertical problems [14], including wheel unloading due to bogie or carbody pitch and bounce. The pitch and bounce modes are excited because the centres of gravity of the vehicles are often higher than the couplers, particularly when the wagons are loaded [8].

The lateral forces in long trains were first studied by El-Sibaie [15], who conducted an experimental analysis of the problem. The lateral coupler forces on one test wagon were controlled by actuators on the adjacent vehicle. Then, as the train ran through a curve, the forces on the wheels were measured using an instrumented wheelset. This approach allows for the relationship between vehicle speed and coupler force to be monitored, and for the derailment quotient to be determined. Cole et al. [16] (among others) combined simulations of longitudinal train dynamics with quasi-statics to obtain the lateral forces; the coupler angles, for curves with a constant radius, were calculated using an approach suggested by [17]. Xu et al. [18, 19] combined a detailed model of three vehicles with a simple model (one degree of freedom) for all other vehicles; this approach reduced the total number of degrees of freedom and thus the computational effort. The vehicles modelled in detail were the locomotives and the adjacent wagons because it is between them that the highest coupler forces occur. The authors concluded that the rotation limit for the coupler best be set to 4°.

An extension of the approach of [17] to transient curves is presented in Chapter 6 together with a comparison between results obtained through the quasi-static approach and results obtained through vehicle simulations.

## 1.5. WHEEL/RAIL CONTACT

The contact between the wheel of a train and the rail is a rolling contact between two bodies, the wheel and the rail, which are stiff, meaning that the deformation of the bodies is small compared to the size of the bodies. Because of the small deformation in the contact bodies, the contacting area is also small compared to the size of those bodies. This makes the nature of this contact very different than, for example, the contact be-

tween a car tire and a road. Owing to the small deformations, the energy loss in the contact area is also small compared to that for road vehicles. However, the small contact area needs to carry a large load, which results in large contact stresses. These stresses, together with the local slip between the wheel and the rail materials, cause the material wear of the wheel and rail and may cause material fatigue, or so-called Rolling Contact Fatigue (RCF).

Models have been developed to relate the relative location and velocity of a wheel to the contact forces, the stress and slip in the contact area. Most methods divide the rolling contact problem into three sub-problems: the contact location problem, the normal contact problem and the tangential contact problem. Only more advanced methods such as Kalker's full theory [20], derivations thereof [21] and finite element models [22, 23] can consider the coupling between the normal and the tangential problems.



### 1.5.1. CONTACT POINT LOCATION

Most contact methods require a reference point to start from. Planar contact methods then assume that the entire contact area is on the plane tangential to the rail surface through that point. Moreover, most methods determine the relative motion between the wheel and the rail from the motion at that point. There can be multiple contact areas per wheel/rail pair. These contact areas can be treated as sub-contact areas with the same reference point (interpenetration methods [24], Kalker's full theory [20]). In this case, it is assumed that the sub-contact areas are in the same plane. Another possibility is to define a different reference point for each contact. In this case there are multiple contact problems per wheel/rail contact, which are solved separately but are coupled through the position of the wheelset (determining the overlap between the wheel and rail profile and thereby the penetration depth) and the resulting contact forces, which must fulfil the equilibrium of force of the wheelset.

In a vehicle simulation, the total resultant force and resultant moments of all contact points at the centre of the wheelset are to be known. For the resulting moments, it is necessary to know the location of the contact forces. Although it would be possible to calculate the moments by integrating the normal and tangential stresses in the contact areas, it is more common to first calculate the resultant forces at each contact point and then calculate the resulting moments using the contact points' locations. It is commonly assumed that the contact areas are in the vertical plane through the wheel axis; this assumption is further investigated in Chapter 2.

## 1.6. THE NORMAL CONTACT PROBLEM

First, there is the normal contact problem, in which the relation between the position of the two contact bodies (i.e., wheel and rail) and the normal pressure distribution between the bodies must be determined. The position between the bodies is often defined using the penetration depth (Figure 1.6a), the maximum distance of the overlap of the bodies if they were considered undeformable.

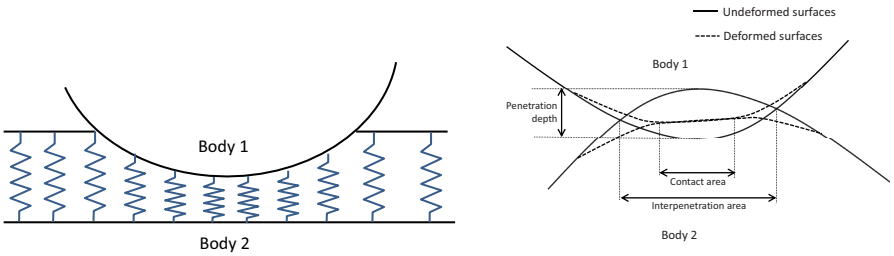


(a) (b)

Figure 1.6: (a) A Winkler foundation, and (b) the penetration depth and the deformed and undeformed surfaces of the contacting bodies.



### 1.6.1. WINKLER FOUNDATION

A simple method for determining the contact pressure would be to assume that the local contact pressure is proportional to the local penetration depth (Figure 1.6b). For two spheres pressed against each other, this assumption would result in a parabolic contact pressure distribution. This approach is, however, never used for wheel/rail contacts as it is experimentally and analytically proven to be inaccurate. Moreover, there is no need for such a method, because the Hertzian method (explained in the next section) already offers a calculation time short enough for any application.

### 1.6.2. HERTZIAN CONTACT

In 1881, Hertz published his theory on the contact between elastic bodies [25]. The main assumptions of the theory are as follows:

- The material of the bodies is elastic. The two bodies may each have a different set of material properties.
- The stress field in the bodies can be approximated by stress fields in infinite half-spaces.
- The contact area is small compared to the local curvature of the contacting bodies.
- The curvatures are constant inside the contact patch.

Then, the Hertzian theory predicts a planar, elliptical contact patch and an ellipsoidal contact pressure. The size of the contact area and the penetration depth can be calculated from the normal contact force and the local curvatures of the contacting bodies (see [26]).

### 1.6.3. INTERPENETRATION METHODS

The interpenetration methods estimate the contact area based on an area in which the bodies overlap if they are considered undeformable (Figure 1.6a). This area is larger than

the real contact area. This problem is solved by employing a virtual penetration depth instead of the real penetration depth. This virtual penetration depth is assumed to be proportional to the real penetration. The contact area is then assumed to be the area in which the two bodies overlap when they approach each other by the virtual penetration depth.

It is then assumed that the contact pressure distribution is elliptic in the longitudinal distribution and proportional to the contact patch width in the lateral distribution.

The Piotrowski [27] and Linder [28] methods use the contact pressure based on the interpenetration area, with a virtual penetration 0.55 times the real penetration. The Linder method uses this area directly, whereas the Piotrowski method first applies a correction function on the obtained area. The Stripes method [29] does not use a fixed virtual penetration but one dependent on the local curvatures of the wheel and the rail.

More details about the implementation of the interpenetration methods can be found in Appendix A.2.3.



#### COMPARISON OF THE INTERPENETRATION METHODS

The interpenetration methods were compared with each other and with Kalker's full methods by Sichani et al. [24] with respect to the shape of the contact area. The contact patch and the stress distribution were compared with those by Kalker's complete theory implemented in the computer code CONTACT. The results obtained from the interpenetration models were more similar to those of the reference (CONTACT [20]) than to the Hertzian results. However, it was concluded that further improvement with respect to the contact patch and pressure distribution estimation is required.

## 1.7. THE TANGENTIAL CONTACT PROBLEM

Once the normal contact pressure is known, the tangential problem may be solved. The tangential problem consists of the relation between the relative motion of the two bodies and the tangential stresses/forces on the contact surfaces. This motion is the slip between the wheel and the rail. For the dry frictional contact between a wheel and a rail, it is often assumed that the tangential contact problem is independent of the vehicle speed, such that the tangential forces depend on the relative slip, the so-called creepage, rather than the real slip.

### 1.7.1. CREEPAGE

Creepage is the relative slip between the wheel and the rail. The longitudinal ($\eta$), lateral ($\nu$) and spin ($\psi$) creepage can be defined as follows:

$$\nu_x = \frac{V_w - \omega R_{loc}}{V_{\text{ref}}} \tag{1.1}$$

$$\nu_y = \frac{V_{\text{lat}}}{V_{\text{ref}}} \tag{1.2}$$

$$\psi = \frac{\Omega_n}{V_{\text{ref}}} \tag{1.3}$$

were:

- $V_{\text{ref}}$ is the reference speed, normally the forward velocity of the centre of mass of the wheelset.
- $V_w$ is the forward velocity of the wheel.
- $\omega$ is the rotational velocity of the wheelset
- $R_{\text{loc}}$ is the local rolling radius of the wheel.
- $V_{\text{lat}}$ is the lateral velocity of the wheel.
- $\Omega_n$ is the projection of the rotational velocity of the wheelset on the normal to the local rail surface.

When the vehicle is steadily curving without traction or braking the creepages can be approximated as follows:

$$\nu_x = \pm\left(\frac{y\gamma}{R_w} - \frac{l}{2R_{\text{curve}}}\right) \tag{1.4}$$

where $\pm$ is positive for the outer wheel and negative for the inner wheel in the curve. $R_w$ is the nominal radius of the wheel, $R_{\text{curve}}$ is the curve radius and $l$ is the track width. This equation assumes a constant conicity, $\gamma$, of the wheel and a linear relation between the longitudinal creepage and creep force. It also requires the knowledge of $y$, the lateral displacement of the wheelset (positive for displacements towards the outside of the curve).

$$\nu_y = \frac{\alpha}{\cos\delta} \tag{1.5}$$

$$\psi = \frac{\sin\delta}{R_w} \tag{1.6}$$

where:

- $\alpha$ is the yaw angle of the wheelset.
- $\delta$ is the contact angle.

Equation 1.5 is often reported in the literature (e.g., [26]) as $\nu_y = \alpha$. However, $\alpha$ is the horizontal/lateral component of slip of the wheel on the rail, whereas we are interested in the slip in the plane tangential to the contact area, hence the division by $\cos\delta$. The division by $\cos\delta$ does not require much computational effort, as the contact angle needs to be known in any case to solve the contact problem. Moreover this addition makes the formula more versatile: It covers not only tread contact but also flanging contact.

### 1.7.2. CALCULATION OF THE RIGID SLIP

The rigid slip is the local slip that would occur between the two contacting bodies if they were considered undeformable. For most contact methods (except the analytical ones presented in Section 1.7.4) the rigid slip needs to be known at each point in the contact area. Assuming the contact area is planar, the rigid slip can be calculated from the creepages at one reference point. Figure 1.7 shows that the rigid slip $(c_x(x,y), c_y(x,y))$

can be calculated when the creepages $(v_{x0}, v_{y0}, \Psi_0)$ at the origin of the reference frame are known:

$$c_x(x,y) = V(v_{x0} + y\Psi_0) \tag{1.7}$$

$$c_y(x,y) = V(v_{y0} - x\Psi_0) \tag{1.8}$$

In addition to calculating the local slip from the slip at the reference point, these equations also change a dimensionless parameter (creepage) into a parameter with the dimension of velocity (the rigid slip). This transformation is performed because in the following sections we define equations using the displacements and velocities rather than their dimensionless counterparts, as some other authors do. The dimensionless counterpart of the rigid slip is referred to as local creepage. Note that these equations are only valid when the contact area is planar; the rigid slip for conformal contact is further discussed in Chapter 4.



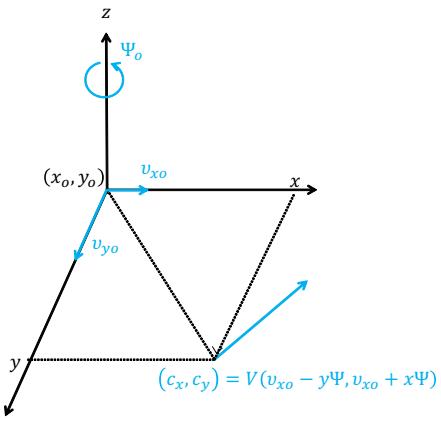


Figure 1.7: Schematic drawing of the rigid slip $(c_x, c_y)$ as a function of the creepages $(v_{x0}, v_{y0}, \Psi_0)$ at the origin of the reference frame.

### 1.7.3. CREEP-FORCE–CURVE

The relation between the creepages and the creep force can be obtained experimentally through a twin-disk test. This test es easiest to perform for the longitudinal creepage/creep force. The creep curve in Figure 1.8, shows that at low creepage the relation is linear; therefore, the creep force reaches a maximum and then becomes constant or decreases slightly with the creepage. In the linear regime, the contact area is partially in slip, in that part of the area there is adhesion, no slip. This situation occurs normally on the leading edge of the contact area, whereas the other part is in slip. After the creep force reaches its maximum, the contact area is in full slip. For this case, often Coulomb friction is used such that the tangential force equals the friction coefficient times the normal force. Alternatively, a speed-dependent friction coefficient might be used to match the falling creep force observed experimentally.

In railways, during traction or braking of a train, it is desirable to reach the maximum tangential force and the corresponding creepage. For all other cases, the creepages are desired to be small because they cause slip and hence energy loss.

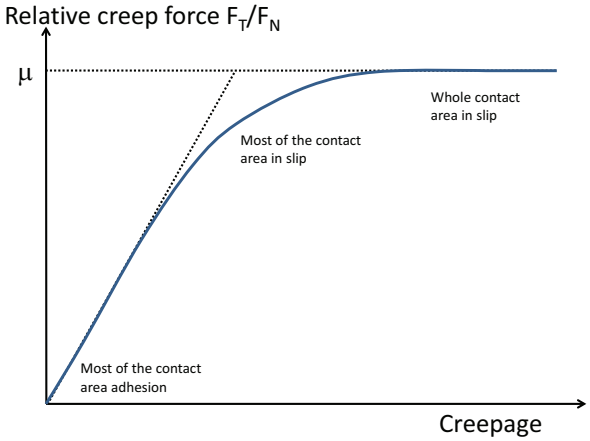


Figure 1.8: The creep force relative to the normal force as a function of the creepage.

### 1.7.4. ANALYTICAL METHODS

Analytical methods provide a quick estimate the creep force as a function of the creepages. The basic methods assume that the creep forces are proportional to the creepages [20], whereas other methods assume more complicated relations [20, 30, 31].

### 1.7.5. FASTSIM

FastSim is based on the simplified theory of Kalker [32, 33]; its two main assumptions are as follows:

- The tangential contact stress is proportional to the local tangential displacement. The ratio between them is called the flexibility parameter. This assumption is the tangential equivalent of the Winkler foundation (Section 1.6.1).
- The tangential stress at the leading edge is zero; from there, the algorithm proceeds in the longitudinal direction and builds up the stress. This procedure is performed line per line in the lateral direction till the whole contact area is covered.

More details about the implementation of FastSim can be found in Appendix A.3.6.

#### MODIFIED FASTSIM FOR INTERPENETRATION METHODS

The interpenetration methods introduced in Section 1.6.3 can also be used for the solution of the tangential contact problem. All these methods rely on an extension of the FastSim method; specifically, they apply the FastSim algorithm on the contact pressure

distribution found using the interpenetration approach. There are two main factors to consider: the flexibility parameter and the rigid body slip.

- The flexibility parameter is either held constant throughout the entire contact area (the Kik-Piotrowski method [34]), or the contact area is divided into longitudinal strips, each with its own flexibility parameter (the Linder [28] and Stripes [29] methods).
- The Kik-Piotrowski and the Linder method calculate the rigid body slip using equations 1.7 and 1.8, as in the original FastSim method, whereas the Stripes method accounts for non-planar contact areas using a varying spin creepage.

More details about the implementation of FastSim for the interpenetration methods can be found in Appendix A.3.6.1.



### 1.7.6. KALKER'S FULL THEORY

Kalker's full theory was developed by Kalker over a long period, beginning with publications in 1966 and 1968 [35, 36] and culminating in the publication of a book in 1990 [20]. In 2001, Kalker wrote a summary of his work for a course at the International Centre for Mechanical Sciences [37].

To solve the normal and the tangential problems, a relation between the local displacements and stresses must be established. Whereas in the simplified theory the local stress is proportional to the local displacement, in the full theory the local displacement is a function of the stress at all other points in the contact area. This relationship is achieved using influence numbers. The influence numbers provide a linear relation between the displacement in one direction at one point and the stress in three directions in all other points of the contact area. To determine this relation, Kalker used the Boussinesq-Cerruti solution for a half-space [38, 39]. In the half-space assumption the boundary conditions are for the real body but the elasticity equations are solved for a half-space. This assumption is a good approximation as long as the contact area is small with respect to the minimum radius of curvature of the contacting bodies near the contact area. As long as the half-space assumption holds and the contacting bodies have the same material properties, the normal and the tangential problem are decoupled.

The influence numbers together with the contact conditions allow for the contact problem to be solved through the iterative process described in Appendix A.3.7.

### 1.7.7. CONFORMAL ROLLING CONTACT

Conformal contact is a contact situation in which the contact angle changes substantially within the same contact area, or where two contact areas are treated together with a different contact angle in each (see Section 1.5.1). Conformal contact is a frequent problem for railways, especially in the arcs of turnouts and in curves. This type of contact causes excessive wear and possible rolling contact fatigue originating from the large tangential stresses and local slip between the wheel and rail. Despite their practical importance, curved contact patches have rarely been addressed in the literature. Li [21] extended Kalker's full theory by employiing quasi-quarter spaces in place of half spaces (See Chapter 4). A. Alonso et al. [40] performed a finite element analysis of the normal

contact problem of planar and curved contact patches and concluded that the influence on the contact pressure distribution is small. However, they did not consider the tangential problem. A. Bhaskar et al. [41] extended the model of Johnson [42] for perturbation analysis to account for a constant radius of the rail profile when calculating the change in longitudinal creepage between two points shifted in the lateral direction.

To solve the tangential contact problem numerically, the rigid body slip is generally computed in each element in the contact patch. Normally, this rigid slip is calculated from the three creepages at a reference point using equations 1.7 and 1.8. These equations assume the contact area is planar, and planar motion can indeed be described using three parameters. However, to describe the relative motion between two bodies in space, six parameters are needed. One possibility would be to calculate the rigid body slip from the six velocities (three translational and three rotational) in the centre of mass of the bogie. This approach is particularly attractive when the contact model is embedded in vehicle dynamic software so that the velocities at the wheelset centre are indeed available. In contact mechanics however, researchers prefer to stick to the concept of creepages at a reference point, because this concept makes it easier to compare the results of a non-planar contact model to those of a reference planar model. Moreover, the quasi-static equations 1.4, 1.5 and 1.6 can be used to determine the creepages.

All current methods, with the exception of the Stripes and WEAR methods, presented in Chapter 4), assume planar contact. The Stripes method solves the above-mentioned problem by calculating the rigid slip under the assumption that the spin only originates from the wheel's rotation around its axis (the geometric spin), neglecting the velocity of the yaw rotation of the wheelset (kinematic spin) [29]. On the other hand, WEAR solves the problem by separating the geometric from the kinematic spin, thereby requiring four creepages as input [21, 43]. Both the Stripes and WEAR methods ignore the effect of the changing contact angle on the lateral creepage (equation 1.5).

### 1.7.8. OFFLINE COMPARISON OF CONTACT METHODS USED IN VEHICLE SIMULATION

A number of fast non-elliptical methods were investigated offline in [24] for their applicability to multibody system simulations: the Kik-Piotrowski [34], Stripes [29] and Linder [28] methods. The contact patch and stress distribution estimated by these methods were compared with those determined by Kalker's full theory implemented in the computer code CONTACT. The results from the non-elliptical models were more similar to the reference results (CONTACT [20]) than the Hertzian results. However, it was concluded that further improvement of contact patch and pressure distribution estimation is required. These three models were mathematically desciber in [34]; moreover, the Kik-Piotrowski method was compared with CONTACT, and the normal solution of the Stripes method was compared with FE results. It was concluded that the creep forces obtained by the Kik-Piotrowski method differ from those determined by CONTACT by up to 5 %. In a benchmark of rolling contact [44], USETAB [20], FastSim, Shen-Hedrick-Elkins [30], Polach [31], Vermeulen-Johnson [42] and linear theory [20] with saturation were compared with each other and with CONTACT. This study, which was limited to Hertzian contacts, concluded that USETAB and FastSim produces errors in the tangential force in the range of 5-10% with respect to CONTACT, whereas the other methods produce

results that differ by 15-60% from those of CONTACT.

In the Manchester Benchmark [45], a number of contact methods currently employed in multibody software (MBS) were investigated. The benchmark consisted of a quasi-static case and the case of a single wheelset running on rails with a prescribed lateral displacement and yaw angle; the resulting creep forces were compared. The effects of using different contact methods on the vehicle's motion were not compared. The comparison of the contact solution was essentially offline, even though some of the contact methods were applied in an online simulation procedure. The normal contact methods used were: Hertzian (VAMPIRE, NUCARS), multi-Hertzian (OCREC, NUCARS) or semi-Hertzian (VOCOLIN, GENSYS); on the other hand, the tangential contact methods used were FastSim and adaptions thereof, and Kalker's lookup tables. The main conclusion was that the models agree well with respect to the contact positions but differ in the shape of the contact area. Another outcome of the study was that the resulting creep forces were very similar for all the codes when the lateral displacement of the wheelset, and therefore the contact angle, was small. However, once the flange clearance was exceeded, the codes produces differences of up to 20% in the creep force.

A true online investigation of the influence of the contact methods on vehicle simulation appears to be missing in the literature; therefore, such an investigation is discussed in Chapter 3 of this dissertation.

### 1.7.9. VALIDATION THROUGH MEASUREMENTS

A common way of validating a contact method is to compare the results to those of a treoretically more rigorous model. Kalker's full theory is often used for this purpose, but some authors have used finite element modelling [22]. However, validation by comparison with measurements is more difficult, as there is no measurement method available that can directly measure the local stresses and local slip between a steel wheel and a steel rail. Therefore a number of measurement systems that measure these factors indirectly have been employed:

- The wheel/rail contact forces can be measured using an instrumented wheelset [46, 47]. This is a wheelset equipped with a number of strain gauges that allow the longitudinal, lateral and vertical forces on each wheel to be calculated. The associated calibration and data acquisition procedures are complicated and expensive.
- The contact forces and the slip between the wheel and the rail can be measured on a twin disk test setup [48, 49], using either a real train wheel or a scaled model consisting of two disks.
- A roller rig is a setup in which the ride of an entire vehicle is simulated by supporting each of its wheels with a large rotating wheel representing the rail [50, 51]. The rig can be a full-scale setup with a real train wheel rolling on a bigger wheel representing the rail or a scaled model.
- The wheel/rail contact forces can be estimated by measuring the displacements in the primary suspension [52].
- Ultrasonic measurements can be used to determine the normal contact pressure and the contact area [53].

- Comparing observations of rail wear and rolling contact fatigue with simulation results is an indirect way of validating contact methods [54, 55].

- Measurements of the energy dissipation of a train travelling through a track with [56] or without [57–59] traction allows for an indirect validation of the contact method.

In Chapter 5, simulated and measured energy dissipation are compared.

## 1.8. MULTIBODY DYNAMICS

### 1.8.1. VEHICLE MODEL



The most suitable method for simulating vehicle dynamics is multibody analysis, in which a vehicle is often modelled by rigid bodies. One rigid body is commonly used for each carbody, bogieframe and wheelset. Therefore, for a passenger wagon seven rigid bodies (one carbody, two bogies and four wheelsets) are each determined by 6 degrees of freedom, yielding 42 degrees of freedom per wagon. Bogies with a more complex anatomy, such as three-piece bogies, may need to be modelled with a higher number of degrees of freedom.

The forces between the rigid bodies are described using linear or non-linear spring elements, viscous dampers, friction dampers or a combination thereof. The forces between the wheels and the rails must be evaluated by a contact method, usually a separate module. In this work, most vehicles simulations were performed using a model of the Dutch VIRM train (bogie shown in Figure 1.9).

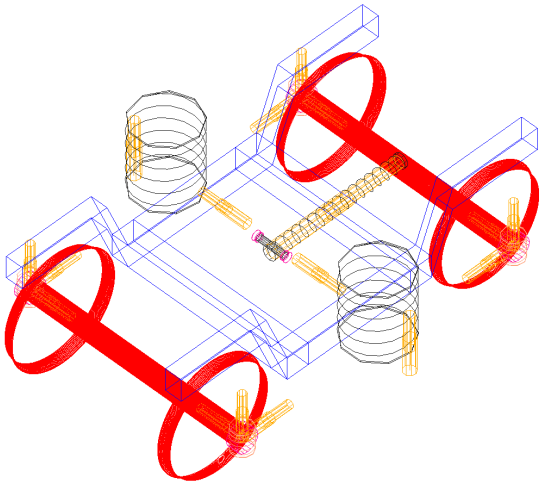

Figure 1.9: Bogie model of the VIRM train.

### 1.8.2. CONSTRAINS VERSUS ELASTIC APPROACH

The wheel/rail contact in a vehicle simulation is implemented through one of two approaches [60]:

- The constraint approach: Two constraints are introduced into the wheelset, such that the wheelset is described with four degrees of freedom instead of six. Note that by applying these constraints, part of the dynamics of the wheelset is removed; the wheelset cannot accelerate in the direction of the two constraints. The constraint approach is employed in SIMPACK and most other vehicle simulation software, and is explained in [61, 62].

- The elastic approach: this approach does not introduce any constraints. Given the exact wheelset position and velocity, one can calculate how the wheel/rail profiles overlap and thus the penetration depth between wheel and rail. In each overlapping area, the contact forces are calculated from the penetration depth and the creepages, which can be obtained from the wheelset velocity. Most models do not include energy dissipation in the normal contact direction because they do not include material damping. This omission could yield a high-frequency behaviour in the normal contact direction. To avoid these high frequencies and make the solution more realistic, vehicle software that uses the elastic approach introduces additional numerical damping [60]. VIRail, the vehicle dynamics software used in the present work, uses the elastic method [63].



### 1.8.3. WHEEL/RAIL CONTACT IN TURNOUTS

Recently, E. Alfi et al. [64] studied the vehicle-turnout interaction. FastSim was used online for wheel/rail contact. However, Kalker reported a 25% difference in frictional work between CONTACT and FastSim [65]. E. Kassa et al. [66] simulated the vehicle-turnout interaction; they accounted for random deviations from the nominal track geometry, but FastSim was also used as the wheel/rail contact model. Shu et al. [67] performed simulations for vehicles in turnouts. Their model was able to detect multiple-point contact and calculate the penetration depth, but the tangential contact problem which is necessary for wear prediction was ignored. Although Wiest et al. [68] and Telliskivi and Olafsson[69] used more advanced methods such as CONTACT and finite element methods, their simulations also neglected the tangential contact problem.

Falomi et al. [70, 71] discussed two different ways of detecting contact points. An overview of contact methods currently used for vehicle simulation can be found in [27, 45, 72]. The most complex model applied to the train-turnout interaction that considers tangential contact appears to be FastSim (e.g., [64, 66]).

## 1.9. RELATION BETWEEN CONTACT METHODS AND WEAR AND ROLLING CONTACT FATIGUE

Because contact forces and vehicle dynamics strongly influence each other, any accurate modelling of the contact forces and their effects on wear, deformation and fatigue should consider the dynamics of the vehicle-track interaction. Such a model should provide insight into the mechanisms of these adverse phenomena so that counter measures may

be developed, which may include improved turnout and rolling stock design as well as more intelligently scheduled maintenance. In the contact patch, the product of the local tangential stress and local slip is local frictional work, which is often used as a predictor for the amount of wheel/rail wear [43, 65, 73, 74]. Using this relation, evolution of the wheel/rail profile can be predicted [21, 55, 65, 75]. Wear is also strongly related to rolling contact fatigue [54, 76–78]; the right amount of wear ('magic wear') can erase initiating cracks and thereby prevent rolling contact fatigue.

A more accurate contact model would lead to a more accurate calculation of the local contact stresses and local slip and thus a more accurate prediction of wear and rolling contact fatigue. However, predicting rail wear and fatigue in turnouts is not trivial because many of the assumptions commonly made in methods that solve for wheel/rail contact, such as a small contact patch and constant spin creepage, may be violated in turnouts.



## 1.10. PROBLEM STATEMENT

The research question is the following:

*How can more insight into the interaction between a vehicle and a complex piece of track, such as a turnout, be gained?*

This research question is divided into several sub-questions:

1. What is the effect of the longitudinal contact position on the vehicle simulation?
2. What is the effect of the tangential contact model on the vehicle simulation?
3. Is it necessary to account for the conformity of the contact area?
4. Is it possible to validate contact or vehicle models through measurements of the wheel/rail frictional power?
5. What is the effect of the coupler forces?

## 1.11. OUTLINE OF THIS DISSERTATION

The outline of this dissertation is shown in Figure 1.10. The train-turnout interaction requires accurate modelling of wheel/rail contacts, the interaction of the vehicles and the track flexibility. Because the modelling of track flexibility is covered extensively in the literature, it is only briefly discussed in the introduction of this dissertation (in Section 1.3).

To the best of the author's knowledge, the effect of the contact model used on vehicle dynamic simulation has not yet been addressed in the literature. The effect of the location of the contact point is discussed in Chapter 2. The effect of the contact method on the vehicle dynamic simulation is analyzed in Chapter 3, in which three interpenetration methods (Kik-Piotrowski, Linder and Stripes) are coupled to MBS software.

To assess the contact forces and contact stress distribution a new method developed by Li [21] is presented in Chapter 4. This method is an extension of Kalker's full theory, intended for conformal contact. The curvature of the contact area has been accounted for in the calculation of the influence numbers and in the rigid body slip in each element

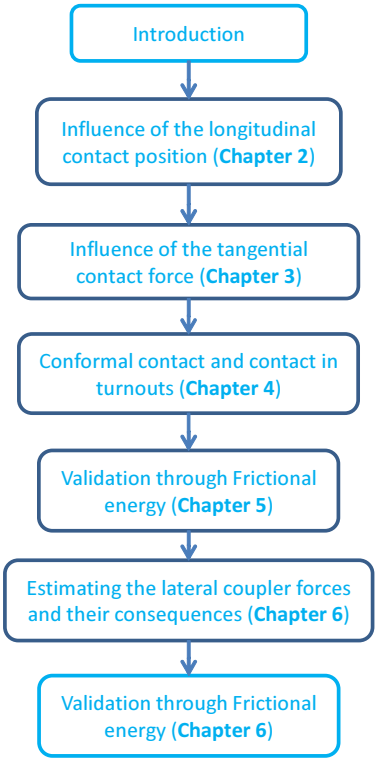


Figure 1.10: Outline of the dissertation.



of the contact area. The new method was applied in post-processing to the wheel/rail contact in a turnout.

Several contact methods are discussed in Chapters 3 and 4. However, it was difficult to determine which contact method is best. It is often assumed that the method that models physical reality best (WEAR, or finite elements) is also the most accurate. However, it is still desirable to validate contact methods by comparison with measurements. Many authors have proposed various measurement methods related to wheel/rail contact, all of which have drawbacks (Section 1.7.9). Chapter 5 proposes that methods be validated through measurements of vehicles' energy consumption. A few methods for calculating wheel rail energy dissipation are presented and compared with each other. Furthermore, a method to extract the power dissipated in the wheel/rail contact from the measured electrical energy consumed by the vehicle's engines is presented.

Coupling between vehicles has two aspects: longitudinal and lateral. The longitudinal forces in the couplers between vehicles have been extensively discussed in the literature; therefore, longitudinal dynamics is only mentioned in the introduction (Section 1.4) and not further studied. The lateral forces, however, have been studied for curves with constant radius but in a turnout, with a changing radius of the curve, such an anal-

ysis appears to be missing. Therefore Chapter 6 extends the quasi-static approach of McClanachan [14] to transient curves, and compares the lateral wheel/rail forces obtained from quasi-statics with those from vehicle simulations. This comparison allows for the identification of a multiplication coefficient to be used with the quasi-static results, and thus yields a fast method for estimating the lateral wheel/rail forces in transient curves and turnouts.

## REFERENCES

[1] C. Esveld, *Modern Railway Track* (MRT-Productions, 2001).

[2] N. Chaar and M. Berg, *Simulation of vehicle–track interaction with flexible wheelsets, moving track models and field tests,* Vehicle System Dynamics **44**, 921–931 (2007).

[3] E. Gialleonardo, F. Braghin, and S. Bruni, *The influence of track modelling options on the simulation of rail vehicle dynamics,* Journal of Sound and Vibration **331**, 4246–4258 (2012).

[4] Y. Bezin, S. D. Iwnicki, M. Cavalletti, E. de Vries, F. Shahzad, and G. Evans, *An investigation of sleeper voids using a flexible track model integrated with railway multibody dynamics,* Proceedings of the Institution of Mechanical Engineers Part F Journal of Rail and Rapid Transit **233**, 597–607 (2009).

[5] E. Kassa and J. Nielsen, *Dynamic train-turnout interaction in an extended frequency range usingh a detailed model of track dynamics,* Journal of Sound and Vibration **320**, 893 (2009).

[6] S. Dietz, G. Hippmann, and G. Schupp, *Interaction of vehicles and flexible tracks by co-simulation of multibody vehicle systems and finite element track models,* Vehicle System Dynamics **37**, 372–384 (2002).

[7] N. Burgelman, Z. Li, and R. Dollevoet, *Some preliminary results in simulation of interaction between a pushed train and a turnout,* in *Proceedings of 22nd International Symposium on Dynamics of Vehicles on Roads and Tracks* (2011).

[8] C. Cole, *Longitudinal train dynamics,* in *Handbook of Railway Vehicle Dynamics,* edited by S. Iwnicki (Taylor and Francis, 2006) p. 239–278.

[9] C. Cole and Y. Sun, *Simulated comparisons of wagon coupler systems in heavy haul trains,* Proceedings of the Institution of Mechanical Engineers, Part F: Journal of Rail and Rapid Transit **220**, 247–256 (2006).

[10] V. K. Garg and R. V. Dukkipati, *Dynamics of railway vehicle systems* (Academic Press, 1984).

[11] T. Geike, *Understanding high coupler forces at metro vehicles,* Vehicle System Dynamics **45**, 389–396 (2007).

[12] S. Mohammadi and A. Nasr, *Effects of power unit location on in-tain longitudinal forces during brake application,* Int. J. of Vehicle Systems Modelling and Testing **5**, 176–196 (2010).

[13] M. Anseri, E. Esmailzadeh, and D. Younesian, *Longitudinal dynamics of freight trains,* Int. J. of Heavy Vehicle Systems **16**, 102–131 (2009).

[14] M. McClanachan, C. Cole, D. Roach, and B. Scown, *An investigation of the effect of bogie and wagon pitch associated with longitudinal train dynamics,* Vehicle System Dynamics **33**, 374–385 (2000).

[15] M. El-Sibaie, *Recent adcancements in buff and draft testing techniques,* Proceedinges of the 1993 IEEE/ASME joint conference **11**, 1–13 (1993).

[16] C. Cole, M. McClanachan, M. Spiryagin, and Y. Q. Sun, *Wagon instability in long trains,* Vehicle System Dynamics **50**, 303–317 (2012).

[17] S. Simson, *Three axle locomotive bogie steering, simulation of powered curving performance passive and active steering bogies,* Ph.D. thesis, Central Queensland University (2009).

[18] Z. Xu, W. Ma, Q.Wu, and S. Luo, *Coupler rotation behaviour and its effect on heavy haul trains,* Vehicle System Dynamics **51**, 1919–1838 (2013).

[19] Z. Xu, W. Ma, Q.Wu, and S. Luo, *Analysis of the rotation angle of a coupler used on heavy haul locomotives,* Proceedings of the Institution of Mechanical Engineers, Part F: Journal of Rail and Rapid Transit **228**, 835–844 (2013).

[20] J. J. Kalker, *Three Dimensional Elastic Bodies in Rolling Contact* (Kluwer Academic Publishers, 1990).

[21] Z. Li, *Wheel-Rail Rolling Contact and its Application to Wear Simulation,* Ph.D. thesis, Delft University of Technology (2002).

[22] X. Zhao and Z. Li, *The solution of frictional wheel-rail rolling contact with a 3d transient finite element model: validation and error analysis,* Wear **271**, 444 (2011).

[23] X. Zhao and Z. Li, *A three-dimensional finite element solution of frictional wheel–rail rolling contact in elasto-plasticity,* Journal of Engineering Tribology **229**, 96 (2014).

[24] M. Sh. Sichani, R. Enblom, and M. Berg, *Comparison of non-elliptic contact models: towards fast and accurate modelling of wheel/rail contact,* Wear **314**, 111–117 (2014).

[25] H. Hertz, *Über die berührung fester elastischer körper,* Journal für die reine und angewandte Mathematik **91**, 156–171 (1881).

[26] S. Iwnicki, *Handbook of railway vehicle dynamics* (Taylor and Francis, 2006).

[27] J. Piotrowski and H. Chollet, *Wheel/rail contact models for vehicle system dynamics including multi-point contact,* Vehicle system dynamics **43**, 455–483 (2007).

[28] C. Linder, *Verschleiss von Eisenbahnrädern mit Unrundheiten,* Ph.D. thesis, ETH Zurich (1997).

[29] J. Ayasse and H. Chollet, *Determination of the wheel rail contact patch for semi-hertzian conditions,* Vehicle System Dynamics **43**, 159–170 (2005).

[30] Z. Y. Shen, J. K. Hedrick, and J. A. Elkins, *A comparison of alternative creep force models for rail vehicle dynamic analysis,* Vehicle System Dynamics **12**, 79–83 (1983).

[31] O. Polach, *A fast wheel-rail forces calculation computer code,* Vehicle System Dynamics **33**, 728 (1999).

[32] J. J. Kalker, *A simplified theory for non-hertzian contact,* Vehicle System Dynamics **12**, 43–45 (1983).

[33] J. J. Kalker, *A fast algorithm for the simplified theory of rolling contact,* Vehicle System Dynamics **11**, 1–13 (1982).

[34] J. Piotrowski and W. Kik, *A simplified theory of wheel/rail contact mechanics for non-hertzian problems and its application in railway vehicle simulations,* Vehicle System Dynamics **46**, 27–48 (2008).

[35] J. J. Kalker, *Rolling with slip and spin in the presence of dry friction,* Wear **9**, 20–38 (1966).

[36] J. J. Kalker, *The tangential force transmitted by two elastic bodies rolling over each other with pure creepage,* Wear **11**, 421–430 (1968).

[37] J. J. Kalker, *Rolling contact phenomena—linear elasticity,* Proceedings of the CISM International Centre for Mechanical Sciences **411**, 1–183 (2001).

[38] J. Boussinesq, *Application des potentiels à l'étude de l'équilibre et du mouvement des solides élastiques,* Gauthier-Villars **Paris** (1885).

[39] V. Cerruti, *Accademia dei lincei,* Mem. fis. mat. **Rome** (1882).

[40] A. Alonso and J. Giménez, *Wheel-rail contact: Roughness, heat generation and conforming contact influence,* Tribology International **41**, 755–768 (2008).

[41] A. Bhaskar and K. Johnson, *Wheel-rail dynamics with closely conformal contact. part 1: dynamic modelling and stability analysis,* Proceedings of the Institution of Mechanical Engineers, Part F: Journal of Rail and Rapid Transit **211**, 11–26 (1997).

[42] K. L. Johnson, *Contact Mechanics* (Cambridge University Press, 1985).

[43] Z. Li and J. Kalker, *Simulation of severe wheel-rail wear,* in *Proc. the Sixth International Conference on Computer Aided Design, Manufacture and Operation in the Railway and Other Mass Transit Systems* (1998) p. 393–402.

[44] E. Vollebregt, S. Iwnicki, G. Xie, and P. Shackleton, *Assessing the accuracy of different simplified frictional rolling contact algorithms,* Vehcile system dynamics **50**, 1–17 (2012).

[45] P. Shackleton and S. Iwnicki, *Comparison of wheel/rail contact codes for railway vehicle simulation: An introduction to the manchester contact benchmark,* Vehcile system dynamics **46**, 129 (2008).

[46] Y.-S. Ham, D.-H. Lee, S.-J. Kwon, W.-H. You, and T.-Y. Oh, *Continuous measurement of interaction forces between wheel and rail,* International Journal of Precision Engineering and Manufacturing **10**, 35–39 (2009).

[47] E. Kasa and J. Nielsen, *Dynamic interaction between train and railway turnout: full-scale field test and validation of simulation models,* Vehicle System Dynamics **46**, 521–534 (2008).

[48] M. Ishida and N. Abe, *Experimental study on rolling contact fatigue from the aspect of residual stress,* Wear **191**, 65–71 (1996).

[49] E. Gallardo-Hernandez and R. Lewis, *Twin disc assessment of wheel/rail adhesion,* Wear **265**, 1309–1316 (2008).

[50] A. Jaschinski, H. Chollet, S. Iwnicki, A. Wickens, and J. Würzen, *The application of roller rigs to railway vehicle dynamicss,* Vehicle System Dynamics **31**, 345–392 (1999).

[51] W. Zhang, J. Chen, X. Wu, and X. Jin, *Wheel/rail adhesion and analysis by using full scale roller rig,* Wear **253**, 82–88 (2002).

[52] A. Matsumoto, Y. Sato, H. Ohno, M. Shimizu, J. Kurihara, T. Saitou, Y. Michitsuji, R. Matsui, M. Tanimoto, and M. Mizuno, *Actual states of wheel/rail contact forces and friction on sharp curves – continuous monitoring from in-service trains and numerical simulations,* Wear **314**, 189–197 (2014).

[53] M. Pau, F. Aymerich, and F. Ginesu, *Ultrasonic measurements of nominal contact area and contact pressure in a wheel-rail system,* Proceedings of the Institution of Mechanical Engineers Part F Journal of Rail and Rapid Transit **214**, 231–243 (2000).

[54] Y. Zhou, S. Wang, T. Wang, Y. Xu, and Z. Li, *Field and laboratory investigation of the relationship between rail head check and wear in a heavy-haul railway,* Wear **315**, 68–77 (2014).

[55] A. Johansson, B. Pålsson, M. Ekh, J. Nielsen, M. Ander, J. Brouzoulis, and E. Kasa, *Simulation of the wheel-rail contact and damage in switches and crossings,* Wear **271**, 472–481 (2011).

[56] G. I. Alarcón, N. Burgelman, J. M. Meza, A. Toro, and Z. Li, *The influence of rail lubrication on the energy dissipation in the wheel/rail contact: a comparison of simulation results with field measurements,* Wear **330**, 533–539 (2015).

[57] P. Lukaszewicz, *Running resistance - results and analysis of full-scale tests with passenger and freight trains in sweden,* Proceedings of the Institution of Mechanical Engineers Part F Journal of Rail and Rapid Transit **222**, 183–192 (2007).

[58] P. Lukaszewicz, *A simple method to determine train running resistance from full-scale measurements,* Proceedings of the Institution of Mechanical Engineers Part F Journal of Rail and Rapid Transit **222**, 331–337 (2007).

[59] J. VanderMarel, D. T. Eadie, K. D. Oldknow, and S. Iwnicki, *A predictive model of energy savings from top of rail friction control,* Wear **314**, 155 (2014).

[60] A. Shabana, K. Zaazaa, J. Escalona, and J. R. Sany, *Development of elstic force model for wheel-rail contact problems,* Journal of Sound and Vibration **269**, 295–325 (2004).

[61] H. Netter, G. Schupp, W. Rulka, and K. Schroeder, *New aspects of contact modelling and validation within multibody system simulation of railway vehicles,* Vehicle System Dynamics **29**, 246–269 (1998).

[62] G. Schupp, C. Weidemann, and L. Mauer, *Modelling the contact between wheel and rail within multibody system simulation,* Vehicle System Dynamics **45**, 349–364 (2004).

[63] *VIrail 16.0 documentation*, VI-grade engineering software & service (2014).

[64] S. Alfi and S. Bruni, *Mathematical modeling of train-turnout interaction,* Vehicle System Dynamics **47**, 551–574 (2009).

[65] J. J. Kalker, *Simulation of the development of a railway wheel profile through wear,* Wear **150**, 355–365 (1991).

[66] E. Kassa, C. Andersson, and J. Nielssen, *Simulation of dynamic interaction between train and railway turnout,* Vehicle System Dynamics **44**, 247–258 (2006).

[67] X. Shu, N. Nilson, C. Sasaoka, and J. Elkins, *Development of a real-time wheel/rail contact model in nucars and apllication to diamond crossing and turnout design simulations,* Vehicle System Dynamics **44**, 251–260 (2006).

[68] M. Wiest, E. Kassa, W. Daves, and J. Nielsen, *Assessment of methods for calculating contact pressure in wheel-rail/switch contact,* Wear **265**, 1439–1445 (2008).

[69] T. Telliskivi and U. Olofsson, *Contact mechanics analysis of measured wheel-rail profiles using the finite element method,* Rail and Rapid Transit **215**, 65–72 (2001).

[70] S. Falomi, M. Malvezzi, E. Meli, and A. Rindi, *Determination of wheel-rail contact points: comparison between classical and neural network based procedures,* Meccanica **44**, 661–686 (2009).

[71] S. Falomi, M. Malvezzi, and E. Meli, *Multibody modeling for railway vehicles: Innovative algorithms for the detection of wheel-rail contact points,* Wear **271**, 453–461 (2011).

[72] S. Magheri, M. Malvezzi, E. Meli, and A. Rindi, *An innovative wheel-rail contact model for multibody applications,* Wear **271**, 462–471 (2011).

[73] H. Grausse and G. Poll, *Wear of wheel-rail surfaces,* Wear **113**, 103–122 (1986).

[74] R. Lewis and U. Olofsson, *Mapping rail wear regimes and transitions,* Wear **257**, 721–729 (2004).

[75] F. Braghin, R. Lewis, R. Dwyer-Joyce, and S. Bruni, *A mathematical model to predict railway wheel profile evolution due to wear,* Wear **261**, 1253–1264 (2006).

[76] R. Dollevoet, Z. Li, and O. Arias-Cuevas, *A method for the prediction of head checking initiation location and orientation under operational loading conditions,* Proc. IMechE, Part F: J. Rail and Rapid Transit **224**, 369–374 (2010).

[77] A. Ekberg, B. Akesson, and E. Kabo, *Wheel/rail rolling contact fatigue - probe, predict, prevent,* Wear **314**, 2–12 (2014).

[78] G. Donzella, M. Faccoli, A. Ghidini, A. Mazzu, and R. Roberti, *The competitive role of wear and rcf in a rail steel,* Engineering Fracture Emchanics **72**, 287–308 (2005).

# 2

# EFFECT OF THE LONGITUDINAL CONTACT LOCATION ON VEHICLE DYNAMICS SIMULATION

*This chapter investigates the effect of the calculation of the longitudinal location of a wheel rail contact point on the wheelset's motion in a vehicle dynamic simulation. All current vehicle dynamic software assume that the contact takes place in the vertical plane through the wheelset's axis. However, when the yaw angle of the wheelset is non-zero, the contact point is situated up to* 10 mm *from that plane. This difference causes a differences in the yaw moment on the wheelset which is used in the vehicle dynamic simulation. First, an existing analytical method to determine the longitudinal method is validated using a numerical approach. Then simulations with both the classic and the new contact location were performed, concluding that the effect of the contact point location on the simulated wheelset's motion is small.*

This chapter has been submitted for publication in Mathematical Problems in Engineering.

## 2.1. INTRODUCTION

To asses the wheel rail contact conditions (e.g. at a turnout) a vehicle simulation and a contact method are needed. There are two possible approaches. Either one can use contact models online in the vehicle simulation, which are advanced while still being fast and robust. Or one can use a simple method contact method to evaluate the contact forces online during the vehicle simulation. And then a sophisticated method offline to resolve the contact problems and obtain a more accurate estimate of the local stress and slip distribution in the contact area. In the later case, the balance of force is not necessarily fulfilled as the contact force calculated with the advanced method are not coupled back to the vehicle dynamic simulation; therefore producing an error. This error is the topic of Chapter 2 and 3. This chapter will focus on the effect of the contact location, whereas the next chapter will focus on the effect of the calculation of the tangential contact force.

A common assumption in vehicle dynamics simulations is that the contact between the wheel and the rail takes place in the vertical plane through the rolling axis of the wheelset. This is correct when there is no angle of attack; however, when the angle of attack is not zero, the actual contact point will shift in longitudinal direction, opposite to the direction of the yaw rotation of the wheelset, see Figure 2.1. Therefore the yaw moment caused by the lateral force of the rail on the wheel will be smaller than expected, i.e. that not accounting for this longitudinal shift in the contact point would lead to an overestimation of this yaw moment. As this moment acts to increase the yaw angle, an overestimation of this moment will lead to an overestimation of the angle of attack of the wheelset. Which in turn would give an overestimation of the derailment risk, as some derailment criterion are based on the angle of attack (e.g. [1–3]).

In this chapter the effect of the longitudinal location of the contact point on the wheelset's yaw angle is quantified through vehicle dynamic simulations. Therefore a method is needed to calculate the longitudinal location of the contact point. We propose to use the principle of contact locus, a line of potential contact points on the wheel profile (see Section 2.2.1). In this way, we avoid the need for a true 3D method such as found in [4–7]. When the angle of attack is zero the contact locus is the principal wheel profile. However, when the angle of attack is not zero, a method is needed to calculate the contact locus. Here, we use an analytical approximation: Wang's method [8] (translated as Appendix D of Li's thesis [9]), based on work of de Pater [10, 11]), explained in Section 2.2.2. This method is fast and so suitable for online evaluation during the vehicle dynamic simulation. Wang's method is compared to results obtained from the projection of a 3D mesh, explained in Section 2.2.3. Due to the interpolations and the numerical minimum search required, the 3D meshing method is considered too slow to be used in vehicle dynamics simulation. However, the accuracy of the 3D meshing method only depends on the mesh size, therefore it allows validating Wang's method.

## 2.2. DETERMINATION OF THE CONTACT LOCATION

### 2.2.1. CONTACT LOCUS

To determine the contact point we assume that the rail is straight and smooth in the longitudinal (rolling) direction, whereas in the lateral direction (i.e. along the rail cross

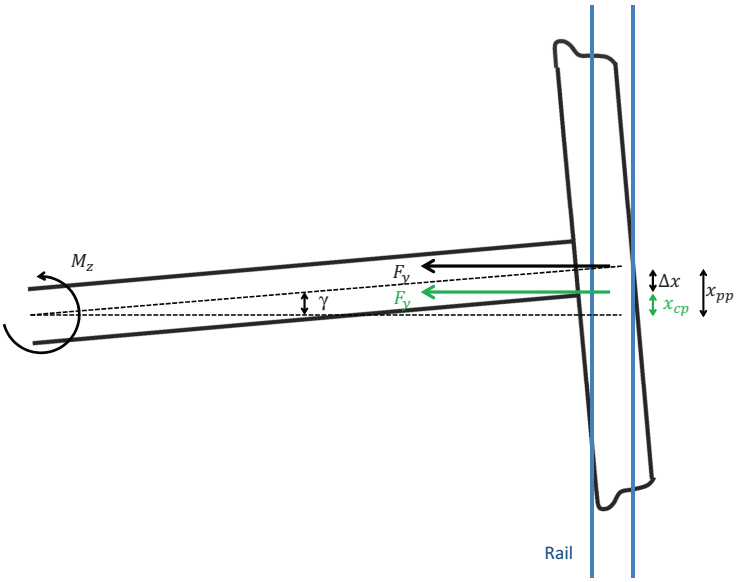


Figure 2.1: A top view of a wheelset with an angle of attack, $\gamma$. The lateral force of the wheel on the rail occurs at the longitudinal contact location defined ($x_{cp}$), whereas current vehicle dynamic simulations assume the contact occurs at the principal profile (longitudinal location defined by $x_{pp}$).



section) we still allow rail surface irregularities. This assumption is widely used in vehicle dynamic simulation, although violated in the case of wheel rail contact at the point of a frog or at the gap of an insulated joint. If these are the areas of interest, it is better to use a finite element simulation instead (eg. [12]).

The assumption of straight and smooth rail allows to simplify the problem by introducing the concept of 'contact locus'. A contact locus is a line of points on the wheel profile where contact is possible, given a certain angle of attack and roll angle. A contact locus can be used instead of a wheel profile leading to a 2D contact point search algorithm.

### 2.2.2. WANG'S METHOD

Wang's method is an analytical approximation; it calculates a correction of the rotated wheel principal profile, i.e. the wheel profile in a vertical plane through the wheel rolling axis. Wheel profiles are commonly defined as a list of points $(y_o(i), z_o(i))$, where $y$ is the lateral and $z$ the vertical direction and with the origin (0,0) half the tape circle distance ($T$) away from the wheelset center in lateral direction and at vertical distance $R_0$ from the wheel axis; this way the local rolling radius $R(i) = R_0 - z(i)$. The wheel rotated principal profiles $(x_{pp}(i), y_{pp}(i), z_{pp}(i))$ can be calculated by translating the reference frame in which the wheel profile is defined to the center of the wheelset and then rotate it around

the angle of attack ($\gamma$) and the roll angle ($\theta$):

$$\begin{bmatrix} x_{pp}(i) \\ y_{pp}(i) \\ z_{pp}(i) \end{bmatrix} = \begin{bmatrix} \cos\gamma & \sin\gamma & 0 \\ -\sin\gamma & \cos\gamma\cos\theta & \sin\theta \\ 0 & -\sin\theta & \cos\theta \end{bmatrix} \begin{bmatrix} 0 \\ y_0(i)+T \\ z_0(i)-R_0 \end{bmatrix} \tag{2.1}$$

Wang's method assumes that at each point on the wheel profile the wheel surface can be approximated as a cone. These cones pass through a point on the wheel profile, with the axes coinciding with the wheelset's rolling axis and a cone angle equal the local contact angle. According to Wang [8], the contact locus ($x_{cp}(i)$,$y_{cp}(i)$,$z_{cp}(i)$) is then found as a correction ($\Delta x(i)$,$\Delta y(i)$,$\Delta z(i)$) of the rotated principal profiles as follows:

$$\Delta x(i) = x_{cp}(i) - x_{pp}(i) = R(i)\sin\theta\sin\gamma + l_x R(i)\tan\delta(i) \tag{2.2}$$

$$\Delta y(i) = y_{cp}(i) - y_{pp}(i) = R(i)\sin\theta\cos\gamma - \frac{R(i)}{1-l_x^2}\left(l_x^2 l_y \tan\delta(i) + l_z m\right) \tag{2.3}$$

$$\Delta z(i) = z_{cp}(i) - z_{pp}(i) = R(i)\cos\theta - \frac{R(i)}{1-l_x^2}\left(l_x^2 l_y \tan\delta(i) - l_y m\right) \tag{2.4}$$

2

where $\delta(i)$ is the local angle of the wheel surface with respect to the wheelset rolling axis.

$$l_x = \cos\theta\sin\gamma \tag{2.5}$$

$$l_y = \cos\theta\cos\gamma \tag{2.6}$$

$$l_z = \sin\theta \tag{2.7}$$

and

$$m = \sqrt{1 - l_x^2\left(1+\tan^2\delta(i)\right)} \tag{2.8}$$

### 2.2.3. SPLINE INTERPOLATION ON A 3D MESH

To validate Wang's method a 3D mesh of the wheel surface has been constructed. A matrix of points on the wheel surface is obtained by revolving the wheel profile around the wheelset's rolling axis, using the parametric equation for a circle through each point on the wheel profile. All the points are then rotated using equation 2.1, then a 3D cubic spline surface is fitted to the mesh points so that the resulting surface is the rotated wheel surface. On the intersection line of this spline surface and a plane vertical and parallel to the rails, the minimum of $z$ is searched, for a given lateral location, using a golden section search. The resulting $z$ and the corresponding $x$ are the coordinates of the contact locus. The surface as well as the contact locus (in red) and the rotated principal profile (blue) are shown in Figure 2.2 for an angle of attack of 5°. This is done for a better visualization as common angles of attack are 0° to 0.5° for trains and 0° to 2° for trams. The advantage of the meshing method is that it does not make geometric simplifications, thus the accuracy only depends on the mesh size, which can always be refined. The disadvantage is that the minimum search requires a substantial computational effort, therefore the method is not suitable for evaluating the contact point location online in a vehicle dynamic simulation.

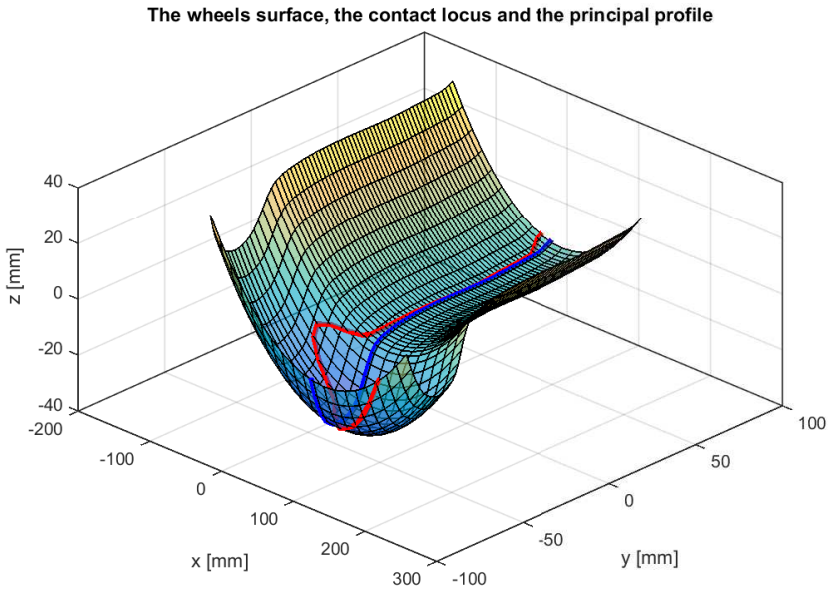


Figure 2.2: The 3d mesh with the contact locus in red and the principal profile in blue. For visualization it is calculated here with a very large angle of attack of 5°, and a coarse mesh.

## 2.3. RESULTS

### 2.3.1. COMPARISON OF METHODS FOR CONTACT LOCUS

Comparing the results obtained from Wang's method with the results from the 3D mesh for an angle of attack of 1° shows a very good fit, see Figure 2.3 and 2.4. It is therefore concluded that Wang's method is sufficient accurate for use in vehicle dynamic simulations.

Looking at Figure 2.4 one can see that the largest longitudinal difference between the rotated principal profile and the real contact locus is around 23 mm. However, this largest difference occurs at the highest contact angle (70°), which will normally not be reached in a common vehicle dynamic simulation.

### 2.3.2. EFFECT ON VEHICLE DYNAMICS

Current vehicle dynamic simulations assume the contact takes place at the principal profile $(x_{pp}, y_{pp}, z_{pp})$, whereas it takes place at $(x_{cp}, y_{cp}, z_{cp})$, calculated in previous section. The location of the contact point has an effect on the moment on the wheelset transferred from the rail on the wheel (see Figure 2.1). The moment from the lateral wheel/rail contact force on the wheelset is normally calculated as $M_z = F_y x_{pp}$, whereas it should be: $M_z = F_y x_{cp}$. Where $F_y$ is the lateral force from the wheel on the rail consisting of the lateral components of the normal contact force and the lateral creep force.

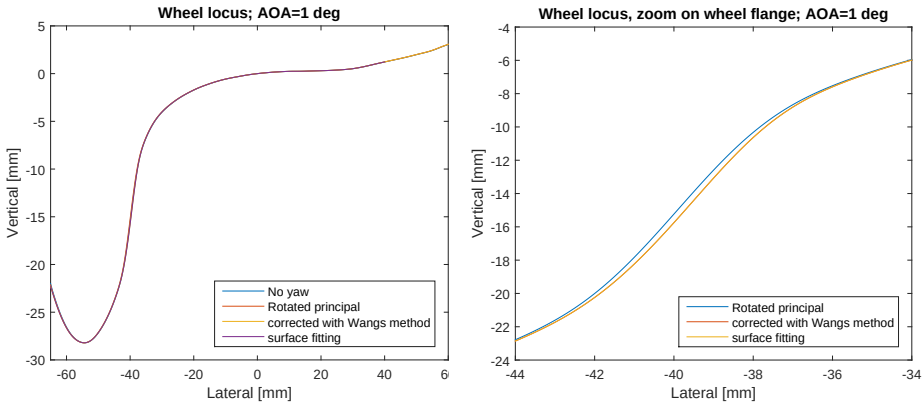


(a) (b)

Figure 2.3: The projection of the contact locus on the yz-plane, vertical and perpendicular to the rail, for a s1002 profile and an angle of attack of 1°. The whole profile (left) and a zoom on the wheel flange (right)



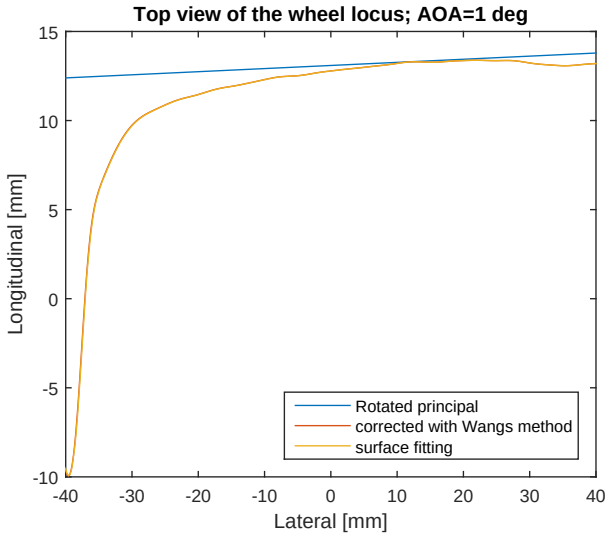


Figure 2.4: The projection of the contact locus on the yx-plane (horizontal plane), for a s1002 profile and an angle of attack of 1°.

A co-simulation was setup between the MultiBody Software (MBS) VIRail and Matlab. At each timestep of the simulation the angle of attack, the roll angle, the lateral creep force, the normal creep force and the contact angle are passed from the MBS to Matlab. Matlab then calculates the lateral force and the difference in moment ($\Delta M_z = \Delta x F_y$) for each wheel. The resulting moment is then fed back to the MBS where it is applied

through an actuator.

The differences in longitudinal location and the resulting moment for a case of a vehicle entering a curve with radius 100 m (realistic for tram networks), are plotted in Figure 2.5a and 2.5b. This moment results in a change in the angle of attack in the simulation, seen in Figure 2.6. It can be seen that the influence of this moment on the angle of attack is very small at around 0.2 %. This can be explained by the observation that the moment applied through the actuator is small compared to the other yaw moments that act on the wheelset, more specifically, the yaw moment caused by the longitudinal creep force. The longitudinal creep force causes a yaw moment equaling $F_x T$, where $T$ is halve the tape circle distance, and even though $F_x$ is generally smaller than $F_y$, $\Delta x$ is much smaller then $T$, so that the moment originating from the lateral contact force becomes negligible.

We conclude that for the case of a vehicle entering a 100 m curve, resulting in an angle of attack of 1° and a contact angle of 40° the influence of the longitudinal contact location if negligible. In tramway the angle of attack can be as high as 2°, and in case of a derailment the contact angle can be up to 70°. However, such angle of attacks will only occur in very tight curves so that the difference in rolling radius between the left and right wheel will not compensate for the difference in traveled distance on the left and right rail, therefore in such cases there will always be a high longitudinal creep force so that the change in moment due to the longitudinal contact location can safely be neglected.



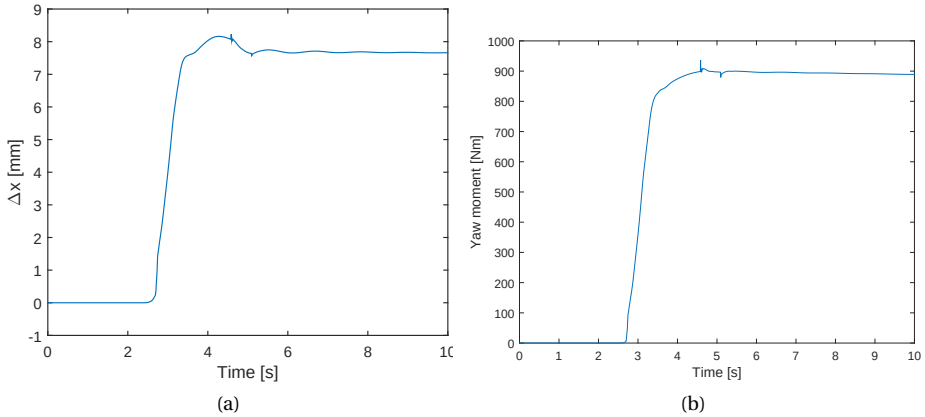


(a) (b)

Figure 2.5: The longitudinal distance between the contact locus obtained with Wang's method and the principal profile at the point of contact (a), and the difference in yaw moment due to the assumed location of the contact patch (b). This difference in moment that is applied on the actuator in the MBS.

## 2.4. CONCLUSIONS

The exact longitudinal location of the contact point can be calculated for normal wheel/rail contact fast and accurately using Wang's method, which was validated using a 3d mesh. However, even though the extra computational time for obtaining such accurate longi-

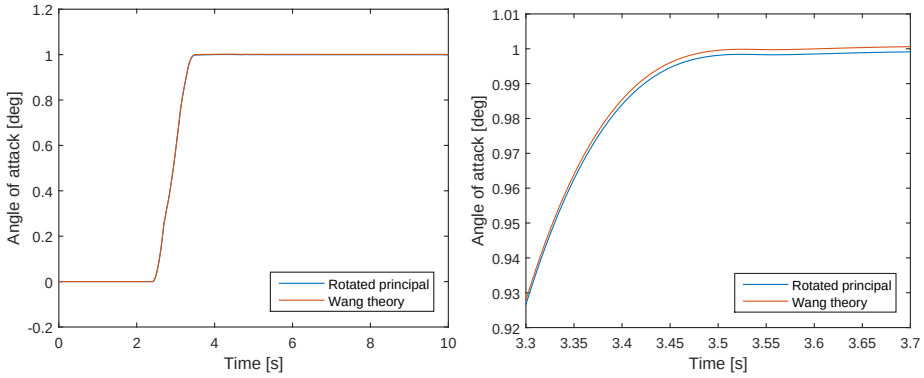


Figure 2.6: The angle of attack of the first wheelset of a vehicle entering a curve with radius 100 m from a simulation with the contact on the rotated principal profile and for a simulation with the contact location obtained through Wang's method (a) and a zoom-in on the moment steady curving is reached (b).



tudinal contact location is small, also the benefits are small, as simulations have shown that the effect of the longitudinal location of the contact point on the vehicle simulation is negligible for contact angles up to 40° and angles of attack up to 1°; for derailment scenarios with contact angles up to 70° further investigation is necessary. Apart from the contact point location, also the contact forces are important to choose whether to use a contact model offline or online, this is further investigated Chapter 3.

## REFERENCES

[1] Q. Guan, J. Zeng, and X. Jin, *An angle of attack-based derailment criterion for wheel flange climbing,* Proceedings of the Institution of Mechanical Engineers, Part F: Journal of Rail and Rapid Transit **228**, 719–729 (2014).

[2] J. Elkins and H. M. Wu, *Angle of attack and distance based criterion for flange climb derailment,* Vehicle System Dynamics **33**, 293–305 (1999).

[3] F. Braghin, S. Bruni, and G. Diana, *Experimental and numerical investigation on the derailment of a railway wheelset with solid axle,* Vehicle System Dynamics **44**, 305–325 (2006).

[4] A. Pieringer, W. Kropp, and D. J. Thompson, *Investigation of the dynamic contact filter effect in vertical wheel/rail interaction using a 2d and a 3d non-hertzian contact model,* Wear **271**, 328–338 (2011).

[5] A. Pieringer, W. Kropp, and J. Nielsen, *The influence of contact modelling on simulated wheel/rail interaction due to wheel flats,* Wear **314**, 273–281 (2011).

[6] A. A. Shabana, M. Tobaa, H. Sugiyama, and K. E. Zaazaa, *On the computer formulations of the wheel/rail contact problem,* Non Linear Dynamics **40**, 169–193 (2005).

[7] M. Malvezzi, E. Meli, S. Falomi, and A. Rindi, *Determination of wheel-rail contact points with semianalytic methods,* Multibody System Dynamics **20**, 327–358 (2008).

[8] K. Wang, *The track of wheel contact points and the calculation of wheel/rail geometric contact parameters,* Journal of Southwest Jiaotong University **1**, 89–99 (1984).

[9] Z. Li, *Wheel-Rail Rolling Contact and its Application to Wear Simulation*, Ph.D. thesis, Delft University of Technology (2002).

[10] A. D. de Pater, *The general theory of the motion of a single wheelset moving through a curve with constant radius and cant,* Journal of Applied Mathematics and Mechancis **61**, 277–292 (1981).

[11] A. D. de Pater, *The geometrical contact between track and wheelset,* Vehicle System Dynamics **17**, 127–140 (1988).

[12] M. Oregui, Z. Li, and R. Dollevoet, *An investigation into the relation between wheel/rail contact and bolt tightness of rail joints using a dynamic finite element model,* International conference on contact Mechanics and Wear of Rail/Wheel Systems, Chengdu, China (2012).

# 3

# THE EFFECT OF THE WHEEL/RAIL CONTACT MODEL ON VEHICLE DYNAMIC SIMULATIONS

*This paper presents a comparison of four models of rolling contact used for online contact force evaluation in rail vehicle dynamics. Until now only a few wheel/rail contact models have been used for online simulation in multibody software. Many more models exist and their behaviour has been studied offline, but a comparative study of the mutual influence between the calculation of the creep forces and the simulated vehicle dynamics seems to be missing. Such a comparison would help researchers with the assessment of accuracy and calculation time. The contact methods investigated in this paper are: FastSim, Linder, Kik-Piotrowski and Stripes. They are compared through a coupling between a multibody software for the vehicle simulation and Matlab for the contact models. This way the influence of the creep force calculation on the vehicle simulation is investigated. More specifically this study focuses on the influence of the contact model on the simulation of the hunting motion and on the curving behaviour.*

This chapter has been published in Vehicle System Dynamics [1].

## 3.1. BACKGROUND

One of the difficult aspects in modelling rail vehicle dynamics is the calculation of the contact forces between wheel and rail. Because the contact forces are evaluated multiple times each timestep, the wheel/rail contact method needs to be fast and robust, yet accurate. To calculate the contact forces, the contact problem is divided into the normal and the tangential problems. For the normal contact problem, the methods used in the currently available software are the Hertzian, multi-Hertzian or semi-Hertzian approaches [2], whereas for the tangential problem the methods are Kalker's simplified theory implemented as FastSim [3], adaptations of FastSim, Kalker's lookup tables [4], linear theory [4], or Shen-Hedrick-Elkins [5]. These methods are fast and robust, and accurate enough to model tread contact, which is contact between the wheel and the rail with a small contact angle. In more extreme contact cases, such as gauge corner contact, flanging with worn wheel/rail profiles, and complicated rail profiles at switch blades and crossings, currently implemented contact models are not accurate enough. In these cases the contact area may be conformal, the contact angle can be large and may vary within the contact patch so that the spin creepage is not constant; moreover, multiple-point contact may occur.

A number of fast non-Hertzian methods have been investigated offline in [6] for their applicability to multibody system simulations: the Kik-Piotrowski [7], the Stripes [8] and the Linder method [9]. The contact patch and stress distribution estimated by these methods were compared with Kalker's complete theory implemented in the computer code CONTACT. The results from the non-elliptical models were closer to the reference (CONTACT) compared with Hertzian results. However, it was concluded that there is a need for further improvement in terms of contact patch and pressure distribution estimation. In [10] these three models are mathematically described, and the Kik-Piotrowski method is compared with CONTACT and the normal solution of the Stripes is compared with FE results. It was concluded that the creep forces from the Kik-Piotrowski method differ up to 5% with the creep forces from CONTACT. In a benchmark of rolling contact [11], USETAB, FastSim, Shen-Hendrick-Elkins, Polach, Vermeulen-Johnson and linear theory with saturation are compared with each other and with CONTACT. This study, which is limited to Hertzian contacts, concluded that USETAB and FastSim give errors in the tangential force in the range of 5-10% with respect to CONTACT whereas the other methods differ 15-60% from CONTACT.

In the Manchester Benchmark [12], a number of contact methods currently employed in multibody software (MBS) were investigated. The benchmark consisted of a quasi-static case and the case of a single wheel set running on the rails with a prescribed lateral displacement and yaw angle and compared the resulting creep forces. They did not compare the influence of the contact methods on the vehicle's motion; they essentially compared the contact methods offline, even though some of the contact methods where applied in an online simulation procedure. The normal contact methods used were: Hertzian (VAMPIRE, NUCARS), multi-Hertzian (OCREC, NUCARS) or semi-Hertzian (VOCOLIN, GENSYS), whereas the tangential contact methods were FastSim and adaption thereof, and Kalker's lookup tables. The main conclusion was that the models agree well with respect to the contact positions, but differ in the shape of the contact area. Another outcome of the study was that the resulting creep forces were

very similar for all the codes if the lateral displacement of the wheel set, and therefore the contact angle, is small. However, once the flange clearance is exceeded, the codes resulted in up to 20% difference in the creep force.

All the above-mentioned studies have compared the contact methods based on separate vehicle and contact simulations, which means that first the vehicle simulation was performed and then the contact methods were applied in post-processing. This procedure does not guarantee that the calculated contact forces satisfy the dynamic equilibrium during the vehicle simulation. Therefore, online simulations with a full vehicle model are needed to investigate the influence of the applied contact model on the vehicle dynamics. Online simulation means that the contact methods that are compared are run each timestep of the vehicle simulation and the resulting creep forces are applied to the wheels in that timestep of the simulation.

### 3.1.1. WHEEL/RAIL CONTACT IN CURRENT COMMERCIAL SOFTWARE

There are two ways of treating the wheel/rail contact [13]:

- The constraint approach: Two constraints are introduced to the wheel set, so that the wheel set is described with four degrees of freedom instead of six. Note that by applying these constraints part of the dynamics of the wheel set is removed; the wheel set cannot accelerate in the direction of the two constraints. The constraint approach is employed in SIMPACK and most other vehicle simulation software, and is explained in [14, 15].

- The elastic approach: It does not introduce any constraints. Given the exact wheel set position and velocity, one can calculate how the wheel/rail profiles overlap, and thus the penetration depth between wheel and rail. In each overlapping area, the contact forces are calculated from the penetration depth and the creepages, which can be obtained from the wheel set velocity. Most models do not include energy dissipation in the normal contact direction, because they do not include material damping. This could cause a high-frequency behaviour in the normal contact direction. To avoid these high frequencies and make the solution more realistic, vehicle software that uses the elastic approach, introduce additional numerical damping. VIRail, the vehicle dynamics software used for the present work, uses the elastic method.



## 3.2. INTRODUCTION TO THE CO-SIMULATION

### 3.2.1. SIMULATION OVERVIEW

Figure 3.1 gives an overview of the simulation procedure. For the vehicle simulation, the MBS VIRail is used, where the initial wheel/rail contact problem is solved using a multi-Hertzian-FastSim approach, which is the most advanced of the contact models available within VIRail. The contact pressure distribution and the tangential forces are obtained with the methods described in section 3.2.3. To use a custom method for the creep force evaluation, the simulation is run with the built-in FastSim to evaluate the creep forces while a corrective force and moment are applied to the wheel set. This corrective force and moment are calculated in such a way that the total force and moment from the rail

on the wheel equal the force and moment that the wheel set would experience if the creep forces were calculated with the custom method.

The coupling between the MBS and the custom made models is achieved through Matlab. First, the normal forces, creep forces, creepages and contact positions calculated by the MBS are transferred to Matlab at each timestep and used as input to the chosen contact method, so that new creep forces are obtained. To apply the right creep force back to the wheel set, the difference between the newly obtained creep forces and the creep forces from the built-in FastSim algorithm is computed. By rotating and translating these force difference the equivalent force and moment in a reference frame fixed to the centre of mass of the wheel set are obtained. This is achieved by rotating the difference between the creep forces around the longitudinal axis with the contact angle and around the vertical axis with the wheel set's yaw angle (see equation (3.1)). The effect of the roll angle of the wheel set is assumed to be small and has been neglected. These rotated forces are then translated from the contact point on the rail profile to the center of mass of the wheel set (see equation (3.2)).

$$\begin{bmatrix} F_x \\ F_y \\ F_z \end{bmatrix} = \begin{bmatrix} \cos\gamma & \sin\gamma & 0 \\ -\sin\gamma & \cos\gamma\cos\delta & \pm\sin\delta \\ 0 & \mp\sin\delta & \cos\delta \end{bmatrix} \begin{bmatrix} \Delta_x \\ \pm\Delta_y \\ 0 \end{bmatrix} \tag{3.1}$$

$$\begin{bmatrix} M_x \\ M_y \\ M_z \end{bmatrix} = \begin{bmatrix} 0 & \mp r & \pm l \\ r & 0 & 0 \\ \pm l & 0 & 0 \end{bmatrix} \begin{bmatrix} F_x \\ F_y \\ F_z \end{bmatrix} \tag{3.2}$$



with

- $F_x$, $F_y$, $F_z$, $M_x$, $M_y$ and $M_z$: the forces and moments in the reference frame fixed to the center of mass of the wheel set and with the y-axis coinciding with the rolling axis of the wheel set;
- $\Delta_x$: the difference in longitudinal creep force between the custom model and the build-in model; parallel to the rail ;
- $\Delta_y$: the difference in lateral creep force between the custom model and the build-in model, perpendicular to the rail; towards the field side of the rail;
- $\delta$: the contact angle - the angle of the lateral creep force with the horizontal plane;
- $\gamma$: the yaw angle of the wheel set;
- $l$: the horizontal distance between the contact point and the center of mass of the wheel set;
- $r$: the vertical distance between the contact point and the center of mass of the wheel set, which is the local rolling radius;
- $\pm$: a plus for the right wheel and a minus for the left wheel;
- $\mp$: a minus for the right wheel and a plus for the left wheel.

The same procedure is applied to other possible contact points on the same wheel and for the other wheel of the wheel set; the resulting equivalent forces and moments are summed up to obtain a total corrective force and moment on the wheel set. These forces and moments are applied to the wheel set in the MBS through actuators.

The set-up with the MBS and Matlab coupled together is flexible; there is no limitation to the complexity of the Matlab code and all variables that are available in the vehicle simulation can be used as an input for the contact model. In this study only models for the creep force calculation are compared with each other, but in the future the same approach could be used to study the influence of the contact search method or the calculation of the normal force. Also models that couple the normal and the tangential problems such as CONTACT could be introduced to vehicle dynamics. The drawback of this set-up is the complexity of the coupling and the large amount of computation time spent on transferring data between the programmes. Therefore, this set-up gives a first insight on the influence of the contact models on the vehicle simulation and could be used for short simulations of wheel/rail contact in complex conditions such as conformal contact and contact with a complex rail geometry (e.g., in turnouts), where models with more advanced contact than FastSim are required. For practical, large-scale simulations the communication between the programmes should be optimised.

The goal of this study is to investigate the influence of the contact model on the simulated vehicle's dynamics. Four different contact methods are considered: three custom models, Kik-Piotrowski, Linder and Stripes, and the built-in model from the MBS: FastSim. To compare the methods two cases are studied: a vehicle passing a single track irregularity that excites a hunting motion, and a vehicle negotiating a curve with the gauge corner contact. For each case, the influence of all the four contact methods on the vehicle's motion will be studied.



### 3.2.2. CONTACT SEARCH AND NORMAL CONTACT FORCE

This study is limited to the influence of different methods to calculate the creep forces on the vehicle dynamics. Therefore, the position of the contact points and the normal contact forces are taken from the commercial software. VIRail determines the interpenetration between the wheel and the rail. In each penetration zone, up to three per wheel/rail contact pair, Hertzian contact is used to determine the normal contact force based on the penetration depth and the local radius of curvature of wheel and rail. The normal contact force is then used to determine a new contact pressure distribution in Matlab, through iteration of the penetration depth and one of the following methods: Linder, Kik-Piotrowski or Stripes. These contact pressure distributions are then used as an input to one of the above-mentioned methods to calculate the tangential contact forces.

### 3.2.3. THE CONTACT PRESSURE DISTRIBUTION AND THE TANGENTIAL PROBLEM

The procedures of the four models are described in Table 3.1. The first one is FastSim; here the contact pressure distribution is ellipsoidal (based on Hertzian theory) and the tangential problem is solved by the original FastSim, of Kalker [3]. The three other models utilise the concept of virtual penetration to find contact patch and pressure distribution. This concept and different implementations of it in each model are described in [6].

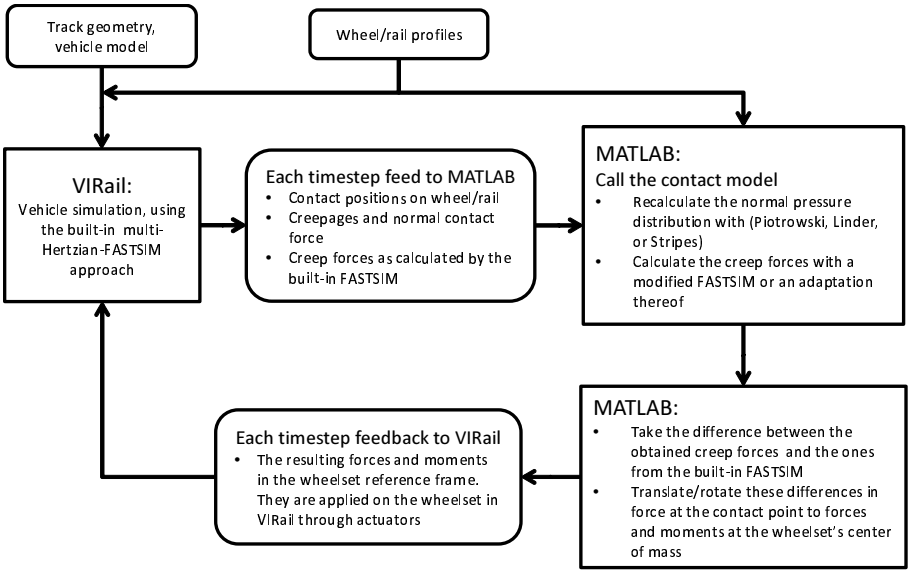


Figure 3.1: Flowchart of the simulations

3

Virtual penetration is used in order to solve normal contact, in cases where the Hertzian geometric assumptions do not hold, without a significant increase in the computational effort. It assumes that the rigid interpenetration zone between the undeformed surfaces of the wheel and rail, is equal to the contact patch if the surfaces approach each other with a fraction of the prescribed penetration value, known as virtual penetration. The contact pressure is assumed to be elliptical in the rolling direction, with the maximum contact pressure at each lateral position being proportional to the local penetration depth of the contact area at that position.

### KIK-PIOTROWSKI

In this method, the interpenetration zone is calculated by assigning the virtual penetration to 0.55 times the rigid body penetration [7]. Then, a shape correction is performed to this zone to obtain the contact patch. The pressure distribution in the lateral direction is similar to the contact patch length at each lateral coordinate. For the tangential part, FastSim algorithm is applied to the non-elliptic contact patch. However, in order to calculate the flexibility parameters needed in FastSim, an equivalent ellipse is assigned to the contact patch [6].

### LINDER

In the Linder method the virtual interpenetration zone is taken to be the contact patch [9]. The patch is then divided in strips in the rolling direction. Unlike the Kik-Piotrowski method, an equivalent ellipse is assigned to each strip [6]. Thus, flexibility parameters used in FastSim are varied through the patch.

#### STRIPES

In the Stripes method, the virtual penetration is a constant value calculated based on the curvature values at the point of contact. The contact patch is divided into longitudinal strips [8]. For each strip, the patch length and its maximum pressure are calculated using local curvature values. An equivalent ellipse is calculated for each strip based on the local curvatures and a modified version of the the FastSim algorithm is applied. Moreover, the contact angle at each strip is considered. Thus, each strip may have a different spin value and the whole contact patch is considered to be curved rather than flat.

#### ACCURACY AND COMPUTATION TIME OF THE MODELS

Due to the difficulty in measuring the real shape of the contact patches and the real creep forces, new contact models are often compared with results obtained with the complete theory of Kalker (the CONTACT algorithm) as opposed to a comparison with measurements. The complete theory from Kalker on its turn has been compared with the results from finite element models in several studies [16]. The accuracy of the non-elliptic models used in this study has been investigated in [6]. Taking CONTACT results as reference, it was concluded that the contact patch estimation and pressure distribution by Stripes are the closest to the reference. Kik-Piotrowski and Linder methods were a bit less accurate. Regarding the creep forces in a pure spin case, the Stripes method predicted higher forces whereas the other methods are closer to the reference. This was related to the fact that in Stripes the spin variation through the contact patch was taken into account, which is not included in the other methods including CONTACT.

Due to the coupling between the vehicle simulation and Matlab, it is difficult to estimate the computation time as much of the time of the simulation is consumed by data transfer between the two programmes. This can be omitted when the contact solution is calculated in a (FORTRAN) subroutine of the vehicle dynamics software, such an option exists in some commercial codes. Nevertheless, it can be mentioned that Stripes is slower than the other two mainly because of the need to calculate the Hertzian solution at each strip.

In all comparisons a friction coefficient, $\mu$, of 0.4 is used.

### 3.2.4. VEHICLE MODEL

A Dutch VIRM double deck wagon is modelled as 7 rigid bodies: a car body, 2 bogies and 4 wheel sets with 42 degrees of freedom. All major non-linearities, such as friction dampers, airsprings and bump stops, are included. The wheel profile is S1002.

### 3.2.5. TRACK MODEL

#### STRAIGHT TRACK WITH A SINUSOIDAL IRREGULARITY

To investigate the effect of the contact model on the prediction of the hunting motion, a straight track with a sinusoidal irregularity was modelled. After 50 meters of straight track the right rail has a vertical dip: a half sine with an amplitude of 5 mm and a wavelength of 9 m. This wavelength was selected because it corresponds to the wavelength observed in wear patterns on the Dutch network. The irregularity initiates the hunting motion, which fades away because the vehicle speed is lower than the critical speed. The study focuses on the influence of the contact model on the hunting wavelength and on

Table 3.1: Overview of the contact models

| | FastSim | Kik-Piotrowski | Linder | Stripes |
|---|---|---|---|---|
| Contact patch | Elliptic | Interpenetration area; corrected | Interpenetration area | Interpenetration area; compensated profile curvature |
| Pressure distribution | Hertzian | Hertzian in rolling direction; similar to patch boundaries in lateral direction | Hertzian in rolling direction | Hertzian in rolling direction |
| Assigned flexibility parameter | Hertzian ellipse | Equivalent ellipse assigned to the whole patch | Equivalent ellipse in each strip; with width equal to the patch width | Equivalent ellipse, using local curvatures, in each strip |
| Local creepage | Constant spin | Constant spin | Constant spin | Spin calculated in each strip using local contact angle |
| Creep force calculation | FastSim | FastSim | FastSim in each strip | Adapted FastSim in each strip |

the damping of the hunting motion (how fast the lateral movement diminishes). On this track the vehicle speed is 72 km/h (20 m/s) and the rail profile is UIC60.

3

#### CURVE WITH RADIUS 500 m

The influence of the contact model on the vehicle's curving behaviour is studied by simulating the passage of the vehicle through a curve. The vehicle starts on a straight track of 50 m followed by 50 m of transition and then a curve with a radius of 500 m and a cant of 8 cm. The vehicle speed for this simulation is 60 km/h, which means there is cant deficiency. The cant deficiency causes the wheel sets to shift outwards and increases the contact angle on the outer wheels. This curve is simulated twice: once with nominal wheel and rail profiles, and once with worn profiles. With nominal profiles, the maximum contact angle found from the vehicle dynamics simulations is 38°, which is large enough to cause a significant difference between the simple FastSim and the more advanced models in calculated creep forces. With worn profiles there is two-point contact on the outer wheel of the leading wheel set; the contact angles are 1.7° and 51°.

Special attention will be paid to the influence of the contact methods on steady curving. A model that predicts a higher longitudinal creep force based on the same creepages should lead to a higher steering moment on the wheel set and consequently, a lateral displacement closer to the one corresponding to ideal curving.

## 3.3. RESULTS AND DISCUSSION

### 3.3.1. COMPARISON OF THE CONTACT METHODS FOR INDIVIDUAL CONTACT CASES

In this section the different contact methods are compared with each other offline. The calculated creep forces are compared for a case with low spin and a case with high spin, with a nominal UIC60 rail profile and S1002 wheel profile. Low spin occurs when the

wheel/rail contact is on the rail top, for example on a tangent track or on the inner rail in a curve. For this case the contact angle $\delta$ was 4.3° causing a spin creepage of $-0.164$ rad/m. The lateral creep forces as a function of the lateral (see Figure 3.2a) and longitudinal creepage (see Figure 3.2b) are very similar for most methods, except for Kik-Piotrowski. The Kik-Piotrowski method results in a higher lateral creep force for the same lateral creepage. Figure 3.3a and 3.3b shows the longitudinal creep force.

For the second case, high spin, the contact angle was 35.5° which corresponds to a spin creepage of $-1.26$ rad/m. For the influence of the lateral creepage on the lateral creep force Stripes results in a lower creep forces for all creepages (see Figure 3.4a), also for very low or high creepages Stripes does not converge to the traction bound $\mu F_n$. This is due to the fact that Stripes accounts for the non-planar contact patch. With planar contact methods, all lateral contact stress is supposed to act perpendicular to the rail surface in the reference point, here chosen at the center of the contact patch. In the Stripes method, the lateral creep force is defined as the integral of all the stress components in the lateral direction of the contact point. Therefore, in a part of the contact patch that has a different contact angle than at the reference point also the normal contact pressure has a 'lateral' component (see Figure 3.5b).

FastSim results in zero longitudinal creep force when the longitudinal creepage is also zero. This is because the contact pressure distribution has two axes of symmetry. The non-elliptical methods do result in longitudinal creep force in the case of zero longitudinal creepage. This longitudinal force is bigger for a larger spin (compare Figure 3.3a with Figure 3.5a). The direction of this force depends on the contact pressure distribution and thus on the local curvature of the wheel and rail profile.

In a curve with cant deficiency, the difference between the rolling radii of a wheel set at the contact points is often larger than required for ideal curving. This causes opposite longitudinal creepages on the two wheels which leads to a steering moment on the wheel set. Regarding the contact models, the longitudinal creep force due to longitudinal creepage is large with the Kik-Piotrowski method in the case of low spin (see Figure 3.3b) and larger with Stripes in the case of high spin (see Figure 3.5b). This means that the steering moment caused by the difference in rolling radii is larger for Kik-Piotrowski so that a better curving behaviour will be predicted using Kik-Piotrowski. The lateral creepages originate from the wheel set's yaw angle. In curving the yaw angle is negative; the wheel set is understeering. This means that the lateral creepage is towards the gauge side and the force on the wheel set is towards the field side for the outer wheel and vice versa for the inner wheel. In other words, a larger lateral creep force pulls the wheel set more to the outside of the curve. Like for the longitudinal creep force, Kik-Piotrowski predicts a higher longitudinal creep force for the same longitudinal creepage than the other models. From the higher lateral creep force can be concluded that Kik-Piotrowski would predict a worse curving behaviour than the other models. The effects of the longitudinal and lateral creep force oppose each other.

### 3.3.2. SINUSOIDAL TRACK

A few phenomena can be observed in the lateral displacement of the leading wheel set shown in Figure 3.6a. First, simulating the vehicle with the Kik-Piotrowski method results in a 15% shorter hunting wavelength. A second observation is that the solutions

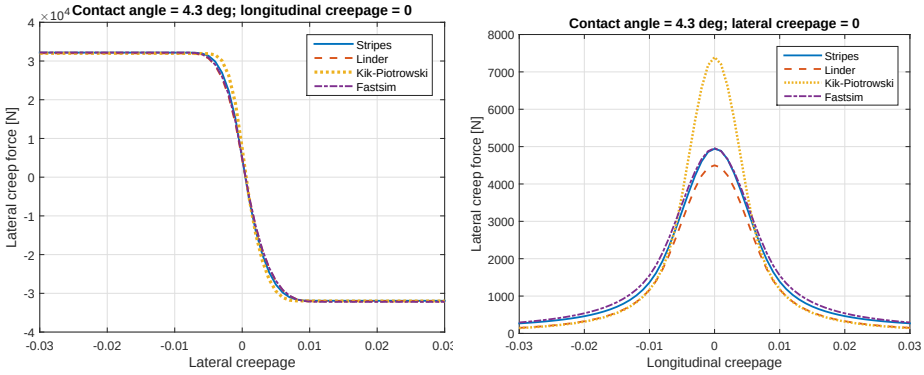


(a) (b)

Figure 3.2: The lateral creep force as a function of the lateral creepage (a) and the longitudinal creepage (b), for a case with low spin.



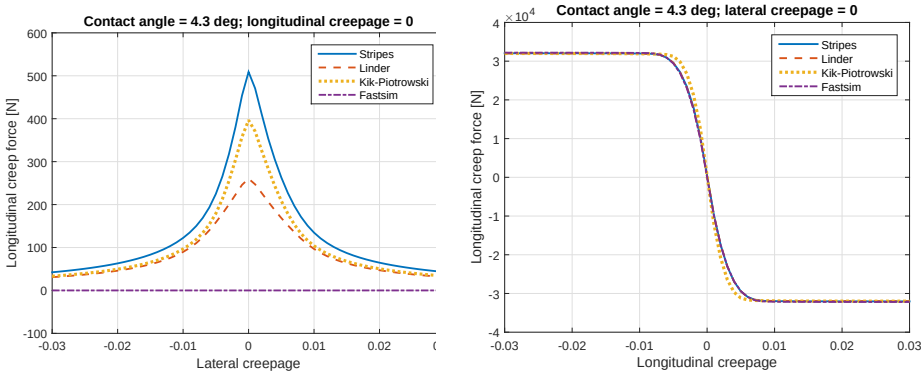


(a) (b)

Figure 3.3: The longitudinal creep force as a function of the lateral creepage (a) and the longitudinal creepage (b), for a case with low spin.

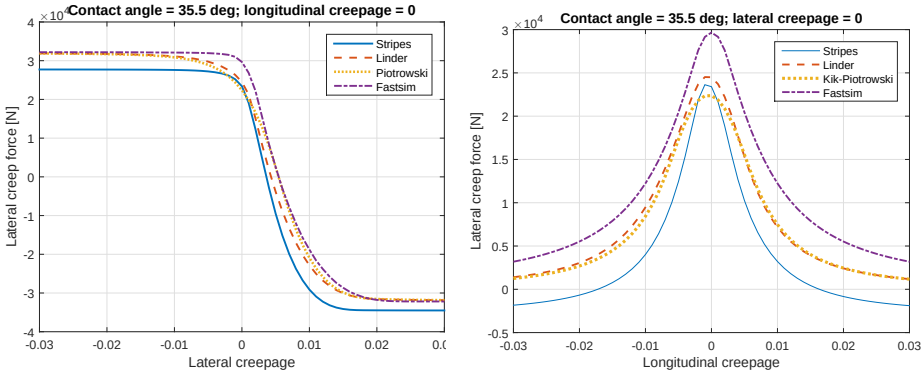


(a) (b)

Figure 3.4: The lateral creep force as a function of the lateral creepage (a) and the longitudinal creepage (b), for a case with high spin.

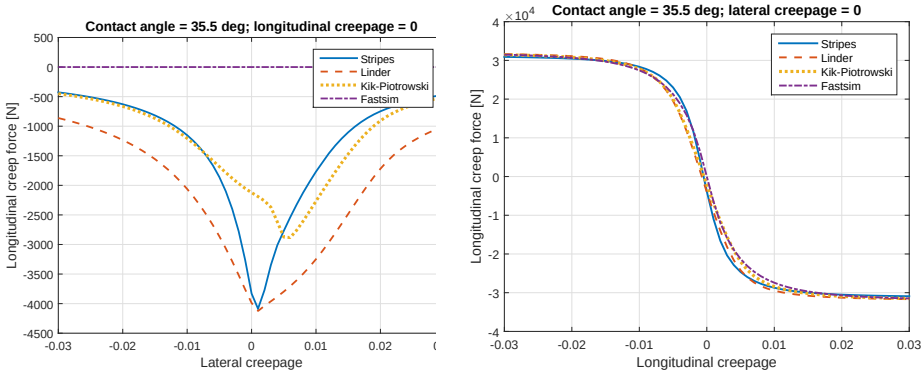


(a) (b)

Figure 3.5: The longitudinal creep force as a function of the lateral creepage (a) and the longitudinal creepage (b), for a case with low spin.

obtained with Stripes and the Linder method are very close to each other, in line with what was observed in the previous section.

Also for the yaw angle of the leading wheel set shown in Figure 3.6b, the solutions from Linder and Stripes are reasonably close to each other. An odd phenomenon can be observed: on tangent track, FastSim predicts zero longitudinal creepage and creep force, whereas the other methods predict zero longitudinal creep force, but a small longitudinal creepage (see Figure 3.7). This is because a longitudinal creep force would cause an uncompensated pitch moment on the wheel set, causing the wheel set to rotate faster, which results in a small creepage. The wheel set is in balance when the longitudinal creepage is just large enough to cancel the longitudinal creep force. This phenomenon can only exist when there is a feedback loop that changes the creepages based on the creep force, so only in an online simulation.

### 3.3.3. CURVED TRACK

Figure 3.8a shows the contact angle of the outer wheel of the leading wheel set of the vehicle when entering the 500 m curve. One can see that all the solutions are close to each other for small contact angles and diverge for larger contact angles. This was expected because a large contact angle and the corresponding spin creepage mean a larger absolute difference between the different contact models. In steady curving FastSim results in a contact angle around 8% higher than the other models.

The yaw angle of the leading wheel set is shown in Figure 3.8b. FastSim results in a 8% higher and Kik Piotrowski in a 4% lower yaw angle compared with Linder and Stripes, which give similar results. The lateral creepage (see Figure 3.9a) is function of the yaw angle and the contact angle; FastSim predicts a 12% higher lateral creepage and creep force than Linder, Kik-Piotrowski and Stripes. The difference in lateral creep force (see Figure 3.9b) is smaller, all contact models lead to creep forces within 5% from each other. Another conclusion is that the results obtained with the Linder and Stripes methods are very close to each other. In Figure 3.8b it can be seen that when the wheel set enters the curve the yaw angle changes signs at time 2.4 s. It is also around the time 2.4 s that the wheel set motion starts to differ depending on the used contact method.

### 3.3.4. CURVED TRACK WITH TWO-POINT CONTACT

The influence of the contact method on simulations of two-point contact is discussed in this section. To such an end, simulations have been performed of a vehicle negotiating a 500 m curve with worn wheel and rail profiles. The wheels are worn to the point where they become hollow. Due of the hollowness of the wheel, the contact angle on the rail top is only 1.95° in the curve, see Figure 3.10b. After 1 s the vehicle enters the turn and at 1.2 s the wheel flange makes a contact angle of 51°. The yaw angle of the leading wheel set (Figure 3.10a) is similar for most contact methods although Kik-Piotrowski results in a bit higher angle. This higher yaw angle also results in a higher lateral creepage (Figure 3.11a) for Kik-Piotrowski. Interesting to notice is that the influence of the contact model depends on the position of the contact point. Figure 3.11b shows the lateral creep force. For tread contact, Stripes and Kik-Piotrowski result in a higher creep force, whereas for flange contact FastSim and Linder result in a higher creep force.

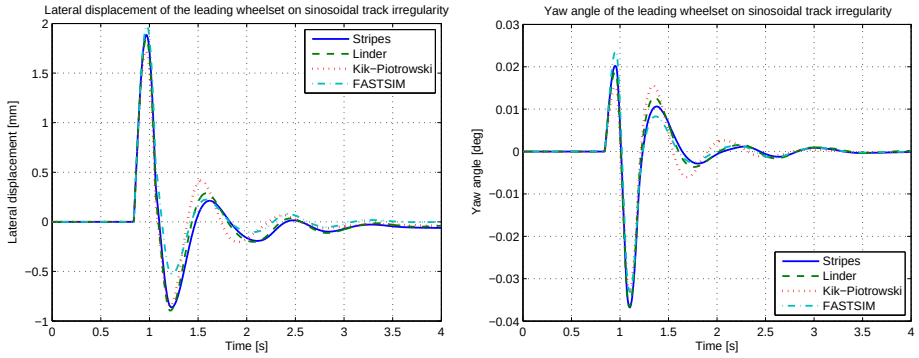


(a) (b)

Figure 3.6: The contact angle (a) on the outer wheel and the yaw angle (b) of the leading wheel set of a vehicle running over a vertical sinusoidal irregularity, initiating the hunting motion, calculated with different contact methods.



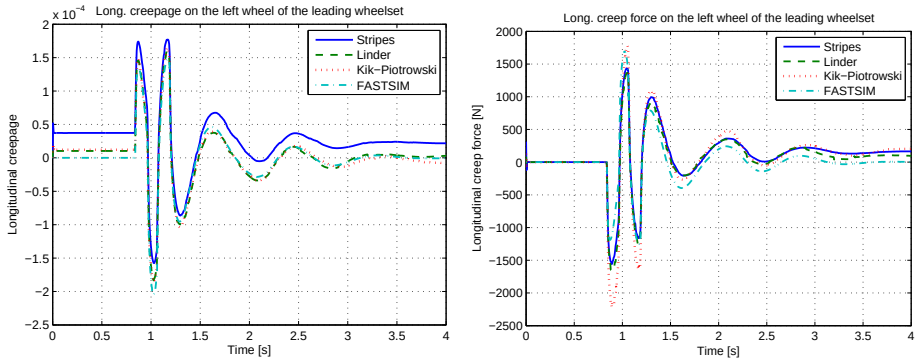


(a) (b)

Figure 3.7: The longitudinal creepage (a)and creep force (b) on the outer wheel of the leading wheel set of a vehicle running over a vertical sinusoidal irregularity, initiating the hunting motion, calculated with different contact methods.

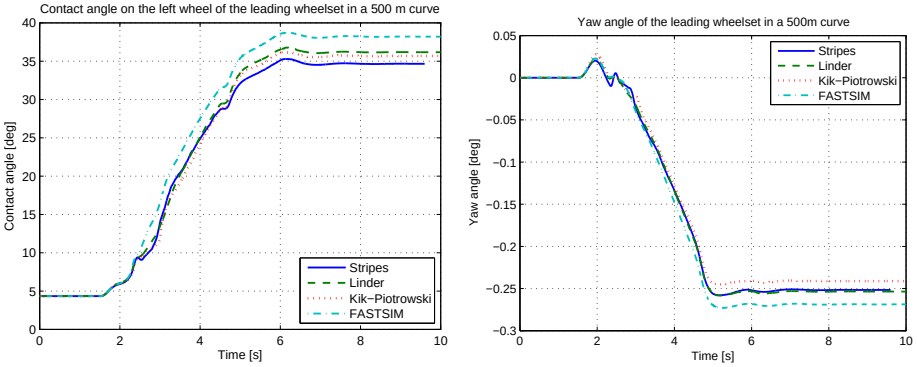


(a) (b)

Figure 3.8: The contact angle on the outer wheel (a) and the yaw angle (b) of the leading wheel set of a vehicle entering a 500 m curve, calculated with different contact methods.



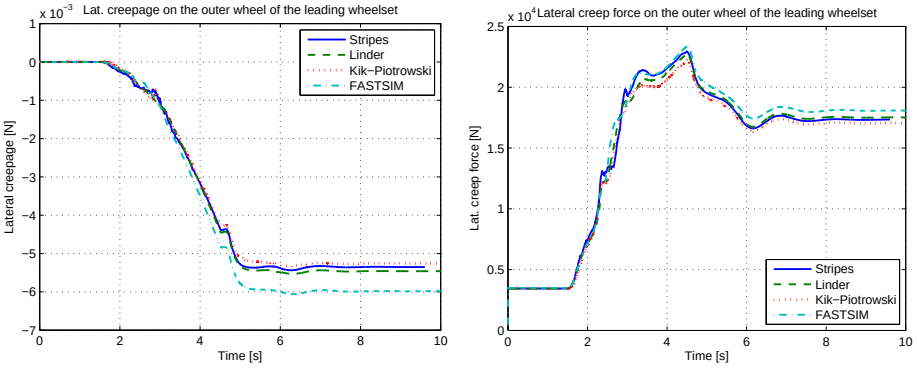


(a) (b)

Figure 3.9: The lateral creerpage (a) and the creep force (b) on the outer wheel of the leading wheel set of a vehicle entering a 500 m curve, calculated with different contact methods.

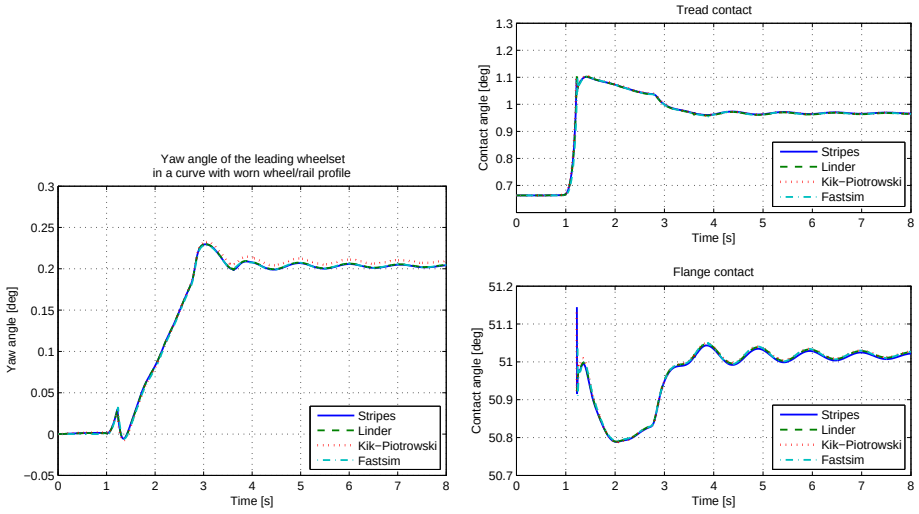


(a) (b)

Figure 3.10: The yaw angle (a) and the contact angle (b) of the leading wheel set of a vehicle running over a curve with worn wheel and rail profiles, calculated with different contact methods.

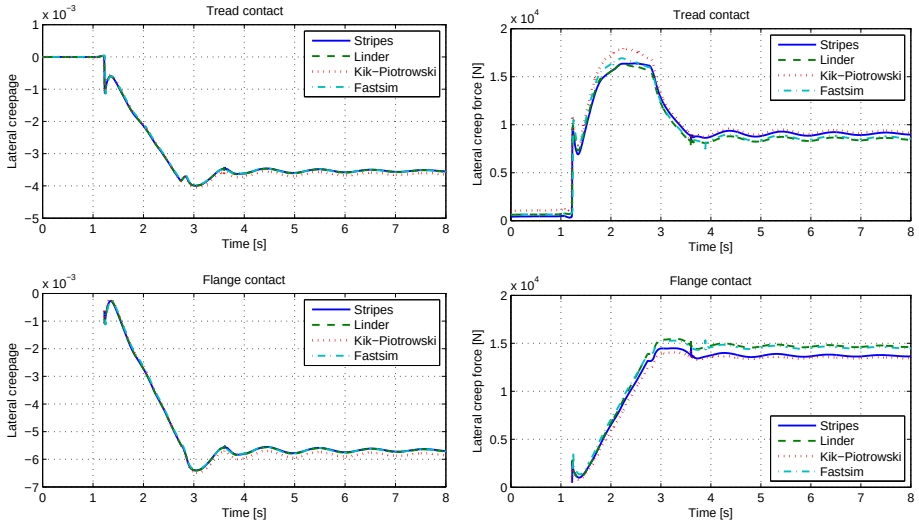


(a) (b)

Figure 3.11: The lateral creepages (a) and lateral creep forces (b) of the outer wheel of the leading wheel set of a vehicle entering a 500 m curve with worn wheel and rail profiles, calculated with different contact methods.

## 3.4. CONCLUSION

A number of different methods for solving the tangential contact problem and calculating the creep forces have been compared with each other with regard to their performance in online vehicle simulations. The simulation set-up introduced in this chapter may be too complex and too slow to be used for the simulation of vehicle dynamics on extended pieces of track. However this set-up allows for some theoretical investigations of the simulation process and more specifically the contact search and contact force algorithms. This set-up can also be useful for short simulations when a high accuracy is needed, for example for situations where extreme contact conditions (large contact angles, multiple contact points, etc.) are expected so that more accurate and time-consuming methods are needed.

By coupling a vehicle simulation software with Matlab we created a versatile tool that enables to investigate the influence of the wheel/rail interaction on the vehicle simulation. In this study only the influence of the creep forces was investigated, but future work could include the comparison of different methods to determine the contact point positions and different methods for the normal contact problem. Also online simulations using the Kalker's CONTACT or a derivation thereof, such as WEAR ([17]), will be possible.

It is concluded that the non-elliptical models Kik-Piotrowski, Linder and Stripes predict a better curving behaviour, lower creepages (12% lower) and creep forces (3% lower), than the elliptical model FastSim. Another finding is that, for curving the difference in the dynamic behaviour of the vehicle between the non-elliptical methods and FastSim is small for small contact angles, but significant for larger contact angles. This shows the need to use more accurate contact models for simulations of a vehicle negotiating a curve. From the simulations about hunting, it is concluded that the Kik-Piotrowski method results in the 15% shorter wavelength, compared with the other models. The more sophisticated non-Hertzian method in this study, Stripes, results in a vehicle behaviour similar to those obtained with the other non-elliptical methods, especially Linder. Therefore, for the cases investigated in this study the need to use Stripes was not shown. There are, however, more extreme contact conditions, such as wheel/rail contact with heavily worn profiles, multiple-point contact, or contact on changing profiles, such as on the switch blade or frog in a turnout. For these extreme conditions, it might be necessary to use a more complex method such as Stripes or even CONTACT in the vehicle simulation.



## 3.5. ACKNOWLEDGMENT

The research for this chapter has been performed in cooperation with Matin Sh. Sichani, PhD candidate at KTH, Stockholm, and his supervisors, Roger Enblom and Mats Berg.

## REFERENCES

[1] N. Burgelman, M. S. Sichani, R. Enblom, M. Berg, Z. Li, and R. Dollevoet, *Influence of wheel–rail contact modelling on vehicle dynamic simulation,* Vehicle System Dynamics **53**, 1190–1203 (2015).

[2] J. P. Pascal, *About multi-hertzian-contact hypothesis and equivalent conicity in the case of s1002 and uic60 analytical wheel/rail profiles,* Vehicle System Dynamics **22**, 57–78 (1993).

[3] J. J. Kalker, *A fast algorithm for the simplified theory of rolling contact,* Vehicle System Dynamics **11**, 1–13 (1982).

[4] J. J. Kalker, *Three Dimensional Elastic Bodies in Rolling Contact* (Kluwer Academic Publishers, 1990).

[5] Z. Y. Shen, J. K. Hedrick, and J. A. Elkins, *A comparison of alternative creep force models for rail vehicle dynamic analysis,* Vehicle System Dynamics **12**, 79–83 (1983).

[6] M. Sh. Sichani, R. Enblom, and M. Berg, *Comparison of non-elliptic contact models: towards fast and accurate modelling of wheel/rail contact,* Wear **314**, 111–117 (2014).

[7] J. Piotrowski and W. Kik, *A simplified theory of wheel/rail contact mechanics for non-hertzian problems and its application in railway vehicle simulations,* Vehicle System Dynamics **46**, 27–48 (2008).

[8] J. Ayasse and H. Chollet, *Determination of the wheel rail contact patch for semi-hertzian conditions,* Vehicle System Dynamics **43**, 159–170 (2005).

[9] C. Linder, *Verschleiss von Eisenbahnrädern mit Unrundheiten,* Ph.D. thesis, ETH Zurich (1997).

[10] J. Piotrowski and H. Chollet, *Wheel/rail contact models for vehicle system dynamics including multi-point contact,* Vehicle system dynamics **43**, 455–483 (2007).

[11] E. Vollebregt, S. Iwnicki, G. Xie, and P. Shackleton, *Assessing the accuracy of different simplified frictional rolling contact algorithms,* Vehcile system dynamics **50**, 1–17 (2012).

[12] P. Shackleton and S. Iwnicki, *Comparison of wheel/rail contact codes for railway vehicle simulation: An introduction to the manchester contact benchmark,* Vehcile system dynamics **46**, 129 (2008).

[13] A. Shabana, K. Zaazaa, J. Escalona, and J. R. Sany, *Development of elstic force model for wheel-rail contact problems,* Journal of Sound and Vibration **269**, 295–325 (2004).

[14] H. Netter, G. Schupp, W. Rulka, and K. Schroeder, *New aspects of contact modelling and validation within multibody system simulation of railway vehicles,* Vehicle System Dynamics **29**, 246–269 (1998).

[15] G. Schupp, C. Weidemann, and L. Mauer, *Modelling the contact between wheel and rail within multibody system simulation,* Vehicle System Dynamics **45**, 349–364 (2004).

[16] X. Zhao and Z. Li, *The solution of frictional wheel-rail rolling contact with a 3d transient finite element model: validation and error analysis,* Wear **271**, 444 (2011).

[17] N. Burgelman, Z. Li, and R. Dollevoet, *A new contact method applied to train-turnout interaction,* Proceedings of the 9th International Conference on Contact Mechanics and Wear of Rail-Wheel Systems , 523–529 (2012).

# 4

# A NEW ROLLING CONTACT METHOD APPLIED TO CONFORMAL CONTACT AND THE TRAIN-TURNOUT INTERACTION

*This chapter introduces a new computer program called WEAR. It contains a new and more accurate method for calculating wheel/rail contact stresses to predict degradation due to wear, deformation and fatigue. WEAR accounts for conformal contact by using influence numbers that are based on quasi-quarter spaces instead of the traditional half-spaces and considers the varying geometrical spin due to the varying contact angle through a contact patch.*

*This new contact method is applied to two cases: wheel/rail contact in a turnout and conformal contact in a curve with a heavily worn wheel profile. In both cases, many of the assumptions commonly made in excising solution methods for wheel/rail contact problems, such as a small contact patch and a constant spin creepage, may be violated. The case of conformal contact demonstrates the effect of the influence numbers and the varying spin creepage on the resulting stresses and creep forces and provides a comparison of this new method with the well-established contact method CONTACT. For the turnout case, the first task is to obtain realistic input for all timesteps of a vehicle coasting through a turnout (i.e., diverging route) in a simulation. This step is necessary because the contact forces, which cause wear, deformation and fatigue of the wheels and rails, and the dynamics of the vehicle-turnout interaction strongly influence each other. WEAR converged for all timesteps, including many cases with multiple-point contacts at the switch blade and with extremely high creepages. This robustness demonstrates suitability of the new method for online contact force evaluation in vehicle dynamics simulations.*

This chapter has been published in Wear [1]

## 4.1. INTRODUCTION

### 4.1.1. WHEEL/RAIL CONTACT IN THE TRAIN-TURNOUT INTERACTION

Turnouts are a major concern for railways due to their high maintenance and repair costs, risk of derailment, and discomfort for passengers. These problems are largely due to the high wheel/rail contact forces, especially in the lateral direction, which are caused by the sharp turn in a turnout, which cannot be compensated for with rail cant. These high forces may lead to severe rolling contact fatigue and excessive wear of the rails and wheels, especially at the switch blade, as well as tilting of the rail, deformation of the switch control mechanism and displacement of the entire track. These effects may cause turnouts to malfunction, in turn causing wheel climb and subsequent derailment.

These problems demonstrate the need to accurately calculate of the contact forces and resulting stresses and strains. Because the contact forces and vehicle dynamics strongly influence each other, any accurate modeling of the contact forces and their consequent effects on wear, deformation and fatigue should consider the dynamics of the vehicle-track interaction. Such a model should provide insight into the mechanisms of these adverse phenomena so that counter measures may be developed, which may include improved design of turnouts and rolling stock and more intelligently scheduled maintenance. In the contact patch, the product of the local tangential stress and local slip is the local frictional work, which is often used as a predictor for the amount of wheel/rail wear [2]. Wear is strongly related to rolling contact fatigue [3–5]. A more accurate contact model would lead to a more accurate calculation of the contact stresses and microslip and thus a more accurate prediction of wear and rolling contact fatigue. However, predicting rail wear and fatigue in turnouts is not trivial because many of the assumptions commonly made for the solution methods of wheel/rail contact, such as a small contact patch and constant spin creepage, may be violated in turnouts. Furthermore, the current wheel rail contact models may not suffice for the interaction between worn wheels and worn rails in curves, where conformal contact commonly occurs.



The first successful numerical solution of wheel/rail rolling was proposed by Kalker [6, 7]. His works established the quantitative relationship between contact force and arbitrary creepage. Kalker's theory was further developed and implemented in his well-known computer program CONTACT [8]. Although CONTACT has been considered not sufficiently fast or stable for vehicle dynamics simulation, the simplified theory of Kalker, called FASTSIM, has been widely employed for such purposes. Recently, E. Alfi et al. [9] studied the vehicle-turnout interaction. FASTSIM was used in real time for wheel/rail contact; however, Kalker reported a 25% difference in frictional work between CONTACT and FASTSIM [10]. E. Kassa et al. [11] simulated the vehicle-turnout interaction; they accounted for random deviations from the nominal track geometry, but FASTSIM was also used as the wheel/rail contact model. Shu et al. [12] performed simulations for vehicles in turnouts. Their model was able to detect multiple-point contact and calculate the penetration depth, but the tangential contact problem which is necessary for wear prediction was ignored. Although Wiest et al. [13] and [14] used more advanced methods such as CONTACT and finite element methods, their simulation also neglected the tangential contact problem. The finite element solution of Zhao and Li [15] addresses both the normal and tangential problems for quasi-static and dynamic cases. However, its long computing time hinders its application in vehicle dynamics simulation.

Shabana et al. [16] described two ways of implementing contact methods into a vehicle dynamics simulation: the introduction of constraints and an elastic approach. Falomi et al. [17, 18] discussed two different ways of detecting the contact points. An overview of contact methods currently used for vehicle simulation can be found in [19–21]. The most complex model applied to the train-turnout interaction that considers tangential contact appears to be FASTSIM (e.g., [9, 11]). CONTACT could also have been used also for the tangential solution, but it was considered overly slow in the last century, when commonly available computers had long calculation times; today's computers do not have this problem. More importantly, the solution process of CONTACT does not always converge. This problem arises when many thousands of contact problems must be solved in a continuous simulation. Furthermore, CONTACT and FASTSIM cannot handle conformal contact.

### 4.1.2. CONFORMAL CONTACT

Conformal contact, (i.e., contact where the contact angle changes substantially within the same contact patch) is a frequent problem for railways, especially in the arcs of turnouts and in curves. It causes excessive wear and possible rolling contact fatigue originating from the large tangential stresses and microslip between the wheel and rail. Despite its practical importance, only a few studies have addressed the issue of curved contact patches. A. Alonso et al. [22] performed a finite element analysis of the normal contact problem of planar and curved contact patches and concluded that the influence on the contact pressure distribution is small; they did not consider the tangential problem. A. Bhaskar et al. [23] extended the model of Johnson [24] for a perturbation analysis to account for a constant radius of the rail profile when calculating the change in longitudinal creepage between two points shifted in the lateral direction.

To solve the tangential contact problem in a numerical method, the rigid body slip is generally computed in each element in the contact patch. This rigid body slip is calculated by adding location-dependent and spin-related components to the lateral and longitudinal creepage at a reference point in the contact patch. All current methods, with the exception of STRIPES [25] and WEAR [26, 27], assume that the spin is constant throughout the contact patch. In contrast STRIPES and WEAR account for the influence of curvature in the contact patch on the local spin. Between WEAR and STRIPES, WEAR has a more advanced method of calculating the stresses using Kalker's full theory, whereas STRIPES calculates the normal pressure from the rigid body interpenetration and the tangential stresses from a modified FASTSIM.



### 4.1.3. SCOPE OF THIS STUDY

As discussed previously, for both vehicle dynamics simulations and wear/damage prediction an accurate model is required for the interaction between the wheel and rail. Many models of wheel–rail contact exist, ranging from being simple but fast to complex and accurate but slow. To simplify the contact treatment the contact patch is typically assumed to be small compared to the characteristic size of the contacting bodies [8, 24]. The spin creepage is almost always assumed to be constant throughout the contact patch. These assumptions are reasonable for contact between the wheel tread and rail crown, but they may not hold for some more severe contact situations, as often en-

countered in the train-turnout interaction.

This chapter introduces the wheel/rail contact method WEAR [26, 27], which does not make these assumptions. WEAR is an extension of the CONTACT algorithm of Kalker, which employed the boundary element method [8]. It was initially developed for the simulation of (severe) wear of wheel/rail contact. WEAR accounts for conformal contact by using the influence numbers for a quasi-quarter space and by using the local and varying spin creepage in each element in the contact patch. A module to determine the position of the contact point and estimate the potential contact area has also been included such that the entire contact problem can be solved in one implementation.

In this chapter, this new method is presented through its application to two cases:

- First, conformal contact is studied. Therefore, a case of flange contact with a worn rail profile has been selected so that conformal contact occurs. The contact area spans a range of contact angles, as shown in Figure 4.1a. Because WEAR is an extension of CONTACT, CONTACT is used as reference contact model for WEAR; the results obtained with both models are compared with each other.
- For the second case, the simultaneous contact between the wheel and switch blade and between the wheel and stock rail in the diverting route of a turnout is considered. This contact situation is of importance because the switch blade is known to be subject to large amounts of wear and rolling contact fatigue. Safe operation of the switch requires the wear at the tip of the switchblade to stay within certain limits. Excessive wear may cause the wheel to run on top of the switch blade instead of being guided along the side, which may lead to derailment. A correct assessment of the contact stresses and the microslip at the switch blade would help to predict wear and understand the mechanisms behind rail defects.
  To investigate wear, fatigue and deformation of wheels and rails in dynamic vehicle-track interaction, it is necessary to examine the suitability of WEAR for simulating vehicle dynamics, in which many thousands of contact problems must be solved online. wheel/rail contact in turnouts is a suitable test for such a purpose, as the multiple-point contact on the switch blade and stock rail, as well as the high creep forces at the moment the wheel touches the tip of the switch blade, are among the most complex contact situations that occur in rail vehicle dynamics simulations. Some of these contacts are conformal because they involve large variations of the contact angle in the contact patch. Therefore, this work first ensures the accurate calculation of creepages and wheelset positions in the simulation of the vehicle-turnout interaction; then, the new contact method is applied to analyze the contact of each timestep in the vehicle dynamics simulation. To be suitable for the dynamics simulation, the contact method must converge at every timestep, even in cases where the dynamics simulation produces less realistic wheel/rail kinematic values. If WEAR is sufficiently robust to converge in all cases it is deemed sufficiently robust to be used online in all vehicle dynamics simulations. The resulting creep forces are compared to the creep forces obtained with FASTSIM, as that method is currently the most widely used in vehicle dynamics simulation.

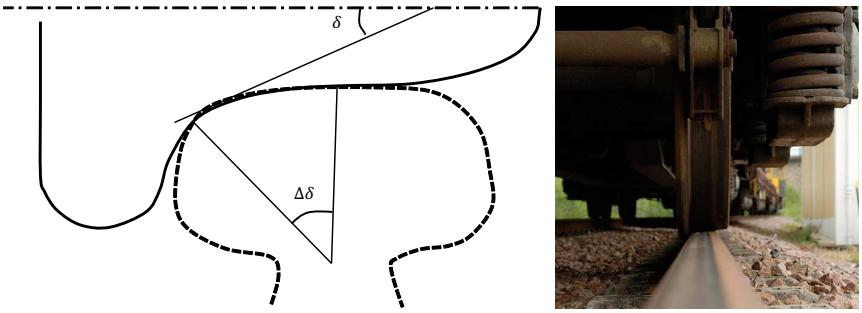


(a) (b)

Figure 4.1: Conformal contact: the contact patch spans a range, $\Delta\delta$, of contact angles, $\delta$.

## 4.2. THE METHOD OF WEAR

This section introduces to the algorithm behind WEAR by comparing it with CONTACT [8], from which it is developed, and with FASTSIM, which is the contact model that is currently employed in most vehicle dynamics simulations.

### 4.2.1. THE OVERALL ALGORITHM OF WEAR

Before the new algorithm can be applied to solve a contact problem, a contact point must first be found on the contacting surfaces of each wheel/rail contact. Because a wheelset is formed with two wheels connected by a rigid axle, the two contact points, each at one of the two wheel/rail contacts, are found together. Such a contact point is called an explicit contact because it is found explicitly by considering the wheelset and rails as rigid bodies. In the case of multiple-point contact, sub-contact patches may develop due to deformation around the explicit contact points, which may not be found when the contacting bodies are regarded as rigid. Next, a potential contact area must be determined around the explicit contact patch, on which the contact problem can be solved. These steps are incorporated into one implementation.

A schematic summary of this implementation is given in Figure 4.2. The method takes the normal contact force and creepages as input and calculates the creep forces. First, the contact locus is calculated for each wheel/rail contact of a wheelset, which is a function of the wheel profile, the lateral wheelset displacement and the yaw angle of the wheelset. The contact locus is determined with a fixed yaw angle and by varying the lateral displacement. For each displacement, iteration is performed on the roll angle of the wheelset $\theta$ until the distance between the rail top and wheel tread is equal for the left and right wheel/rail contacts; then one point is determined for each of the two loci. After the contact loci are determined, they are used as if they were the wheel profiles. Iterations over the roll angle are performed again so that the distances between the left and right rail profiles and loci become equal to each other. This second iteration on the roll angle is necessary to ensure that the contact geometry is computed to the required accuracy, especially when the yaw angle is large.

In the next step, an initial estimate of the penetration is made based on Hertzian theory, followed by an initial estimate of the potential contact area, which is a rectangle around the rigid penetration area. Then, the normal contact problem is solved using the same algorithm as in CONTACT but with the influence numbers for quasi-quarter spaces, which assume a null tangential contact stress (i.e., the influence of the tangential stress on the normal solution is neglected). The accuracy is checked on not only the balance of the total normal force but also the number of elements on the edge of the potential contact area; if this number is overly large, the potential contact area is likely not sufficiently large and should be updated. Once the normal contact problem is solved, the contact patch is known.

The tangential problem is then solved in the known contact patch with the known contact pressure, using the variational method of Kalker [8] with the influence numbers for quasi-quarter spaces and with the methods explained in section 4.2.2.1 to evaluate the rigid body slip. The effect of the tangential contact stress on the normal solution must be considered to obtain an accurate solution; the obtained tangential stress is then applied to the previously determined potential contact area, and the normal problem is solved again to obtain a a new contact area and a pressure distribution. These are compared with the old contact area and pressure. If the differences are larger than the given tolerances, the tangential problem is solved with the new contact area and pressure. The iteration process is continued until the tolerances are satisfied.

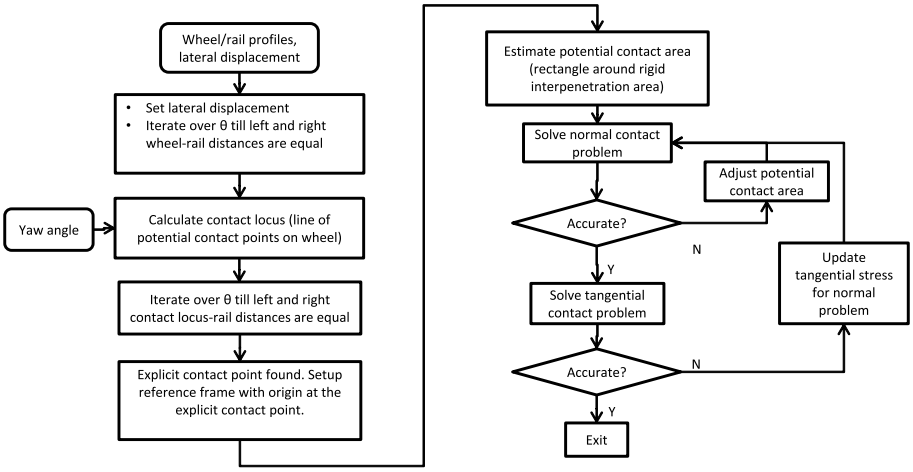


Figure 4.2: Flowchart of WEAR

### 4.2.2. THE DEVELOPMENT OF WEAR WITH RESPECT TO KALKER'S CONTACT

Compared to CONTACT, WEAR has the following improvements:

- CONTACT assumes that the contact patch is planar so that the influence number can be calculated from the Boussinesq-Cerruti solution for a half space [8]. The

influence number $A_{IiJj}$ is defined as

$$u_{Ii} = \sum_{j=1}^{3} \sum_{J=1}^{M} A_{IiJj} p_{Jj} \tag{4.1}$$

which relates the displacement of element $I$ in direction $i$ to the unit contact stress in element $J$ in direction $j$. $i, j = 1, 2, 3$ or $x, y, z$ and $I, J = 1, 2, \cdots, M$, where $M$ is the number of elements in the contact area. To account for the contact at the gauge corner, where the contact patch is no longer planar, WEAR introduces the quasi-quarter space assumption [26, 27], which assumes that the gauge corner and flange root can be approximated with their respective quasi quarter spaces. Unlike the influence numbers for a half space, the influence numbers for the quasi-quarter space could not be found analytically; therefore, they were obtained through the finite element method.

- WEAR considers a geometry dependent spin in each element of the contact area to account for a varying contact angle within the contact patch (see section 4.2.2.1)
- The original CONTACT method has been extended with an algorithm that finds the contact locus. Without yawing, the contact locus is the same as the wheel profile. When the yaw angle is not zero, the contact point on the wheel will not be on the wheel profile, which is the intersection of the wheel running surface with the plane that passes the wheelset axis, but will shift forward or backward on the tread with respect to the intersection. Thus, a contact locus is the line of potential contact points on the wheel when the yaw angle is not zero. A potential contact patch, which is a discretized surface patch on which the solution of rolling contact is sought [8], is determined and optimized automatically (see section 4.2.1). The potential contact patch should be sufficiently large to contain the real contact patch completely, but also as small as possible to minimize the computational costs.

WEAR has been validated with rail wear observations on the Dutch network and has been successfully applied to the determination of loading conditions for head-checking initiation [28].

#### LOCAL RIGID BODY SLIP IN NON-PLANAR CONTACT

To solve the tangential problem, the relative motion in each element of the contact patch of the two bodies must be determined as if they were rigid: this is the rigid body slip. If for a reference point $O$ (Figure 4.3a) in the contact patch the creepages $\xi, \eta$ are known, which allows for the calculation of the rigid body slip at that point with $v_{ox} = R_o \Omega \xi$ , $v_{oy} = R_o \Omega \eta$, where $R_o$ is the local wheel radius at the reference point $O$ and $\Omega$ is the rotational velocity of the wheelset about its rolling axis. From these equations and from the geometrical spin creepage at the reference point, the rigid body slip can be calculated for each point in the contact patch as follows, assuming that the contact patch is planar:

$$v_x = v_{ox} - y\Omega \sin \delta_o = v_{ox} - y\Omega_{oz} \tag{4.2}$$

$$v_y = v_{oy} + x\Omega_{oz} \tag{4.3}$$

where $\Omega_{oz}$ is the component of $\Omega$ normal to the contact patch: $\Omega_{oz} = \Omega \sin\delta_o$, where $\delta_o$ is the contact angle at the reference point (see Figures 4.1a, 4.3a and 4.3b).

If the contact patch is non-planar, the rigid body slip follows as (Figure 4.3c):

$$v_x = v_{ox} - (R - R_o)\Omega \tag{4.4}$$

$$v_y = v_{oy} + x\Omega \sin\delta \tag{4.5}$$

It can be verified that for a planar contact area, (4.4) reduces to (4.2) because $R - R_o = y \sin\delta_o$. Terms with kinematic spin can readily be added to (4.2)-(4.5) if necessary [27]. In this case, the local rolling radius, $R$, must be known everywhere in the contact patch (see Figure 4.3c). This means that contact methods that assume non-planar contact, such as WEAR, require the wheel profiles as input, whereas contact methods that assume planar contact patch suffice with knowledge of the principal radii of the bodies and the contact angle at a reference point. Figure 4.3c illustrates that if planar contact were assumed, the values of $R - R_o \sin\delta$ would be underestimated at the gauge side and overestimated at the field side. This results in a higher longitudinal and lateral rigid body slip at the gauge side for non-planar contact and a lower rigid body slip at the field side compared to planar compact.

Furthermore, higher and lower tangential traction is expected at the gauge side and field sides of the adhesion zone, respectively. In the slip zone, the tangential traction is limited by the local contact pressure and the friction coefficient, and thus does not depend on the rigid body slip. The local slip only differs from the local rigid body slip by the difference of the deformation gradient between the two bodies:

$$\mathbf{s} = \mathbf{c} - (\partial \mathbf{u}/\partial \mathbf{x})\, nV \tag{4.6}$$

where $\mathbf{s}$ is the slip vector; $\mathbf{c}$ is the rigid body slip vector, where $\mathbf{c} = (v_x, v_y)$, $\mathbf{u}$ is the deformation vector; $\mathbf{x} = (x, y)$; and $V$ is the reference speed, $V = R_o\Omega$. $|\mathbf{s}| = 0$ in the adhesion zone, and $|\mathbf{s}| > 0$ in the slip zone. Therefore, for non-planar contact, a higher slip is expected at the gauge side and a lower slip is expected at the field side.

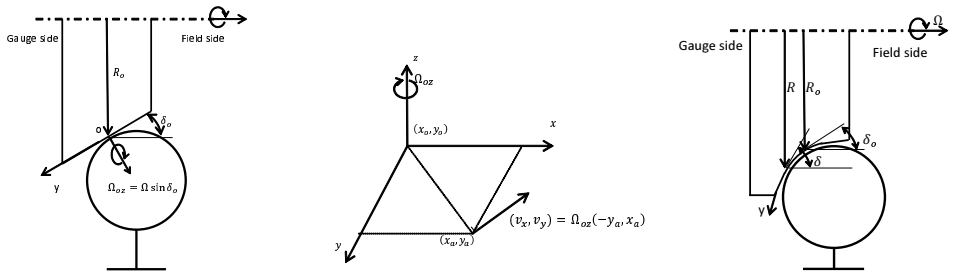


Figure 4.3: Sketches of the different contact conditions. (a) planar contact with a constant angle $\delta_o$; (b) the relative velocity $v_a$ of point $a$ with respect to reference point O due to spin in planar contact and (c) non-planar contact with a varying contact angle $\delta$.

### 4.2.3. DIFFERENCE BETWEEN WEAR AND FASTSIM

FASTSIM assumes that the contact patches are planar and elliptical, and spin creepage is assumed to be constant throughout the entire contact patch. When using FASTSIM for problems with multiple contact points, it is assumed that the sub-contact patches at the individual contact point do not influence each other [19]; this allows the method to be applied to all of the contact points separately. However, FASTSIM exhibits some limitations when calculating wheel/rail contact in turnouts. In a turnout there is often contact at the gauge corner, which may result in multiple-point contact or conformal contact, especially when the wheel and rail are worn; in this case the geometrical spin creepage may not be constant in the contact patch. FASTSIM cannot account for this phenomenon. The advantages of WEAR over multi-Hertzian-FASTSIM are:

- Different contact points are not treated separately but rather in one potential contact patch; the influence of the displacement field of one sub-contact patch on another sub-contact patch is included. This inclusion is believed to be especially important when contact patches are close to one another, although this influence has not yet been fully investigated in the literature.
- In the multi-Hertzian-FASTSIM approach, different sub-contact patches have different reference points for which the spin creepage is calculated, whereas in WEAR, the geometrical spin creepage is rigorously computed from the contact geometry in each surface element in the contact patch (see section 4.2.2.1). This distinction is especially important for conformal contact, because the contact patch is large in the lateral direction across the gauge corner, resulting in a large range of contact angles and rolling radii in the contact patch.

The advantages of WEAR become especially important when considering profiles in practical applications. The profiles are often so irregular that multiple contact patches occur close to each other. Most classical contact methods resolve this issue by applying a strong smoothing to the profiles before applying contact methods based on Hertz theory, which requires smooth profiles to derive the radii of curvature. Such smoothing may remove the real geometric features of the contact, rendering the solution non-physical and inaccurate. An example of the use of the Hertzian-FASTSIM approach with rough surfaces can be found in [29]. WEAR can handle full non-Hertzian contact geometry, thus negating the need for profile smoothing.



## 4.3. CONTACT IN TURNOUTS

To assess the performance of the new contact model, contact simulations are performed with input data obtained from a vehicle simulation.

First, the Multibody Software (MBS) VIRail is employed to perform a vehicle simulation in which the wheel/rail contact forces are evaluated using a multi-Hertzian approach for the normal force and FASTSIM for the tangential forces. The calculated creep forces, wheelset position, creepages and normal contact force are communicated to WEAR. WEAR performs a contact calculation, including the contact point search. WEAR yields more accurate values of the creep forces than the values obtained with FASTSIM.

### 4.3.1. VEHICLE MODEL

The modeled vehicle is a double-deck passenger car that is currently widely used on the Dutch rail network. Each vehicle has 42 degrees of freedoms (dof):, with 6 dof for each of the wheelsets, the bogie frames and the car bodies. All major non-linearities in the primary and secondary suspension are considered, including the friction dampers, bump stops and airsprings.

A comparison between the hunting wavelength obtained from simulations and the hunting wavelength observed in wear patterns in tracks has been performed to calibrate the primary yaw stiffness [30]. The hunting motion of the vehicle can be strongly affected by the primary yaw stiffness, which is also a dominant factor for the wear rate.

### 4.3.2. TURNOUT MODEL

In this research, a UIC1:15 turnout with a radius of 725 m is modeled with the design track geometry and rail profiles. The flexibility of the track is modeled for each wheelset independently with a co-traveling model. The model consists of one rigid sleeper, which is allowed to roll and translate vertically and laterally in the vehicle reference frame. The properties of the ballast are expressed as one spring/damper pair between the ground and sleeper. The rail pads are modeled as spring/damper pairs between the sleeper and rails. This limited flexibility is only accurate in a limited frequency range and does not account for changes in track stiffness along the turnout. However, this limited track flexibility is considered sufficiently accurate for this study, which focuses is on the wheel/rail contact model; other studies have used simpler contact models but an extended track flexibility model [9, 31]. In a later stage, WEAR could be combined with a more extensive model of the track.

## 4.4. RESULTS

### 4.4.1. RELATIVE ERROR OF PLANAR CONTACT IN THE RIGID BODY SLIP

#### THE LONGITUDINAL RIGID BODY SLIP

In Section 4.2.2.1, it is discussed that by assuming a planar contact area, error can be introduced into the calculated rigid body slip at the gauge corner where the geometrical spin changes significantly due to the change in the contact angle along the rail profile in the contact area. The error is now further analyzed for a rail profile with a constant radius. The center of the contact patch is chosen as the reference point.

The difference between a planar (Figure 4.3a) and non-planar contact patch (Figure 4.3c) in calculating the longitudinal rigid body slip at the edge of the contact patch is shown for a rail profile with a constant curvature (see Figure 4.4). The relative error introduced by assuming the contact patch to be planar can be calculated from Equations (4.2) and (4.4) with $v_{ox} = 0$:

$$\textbf{Relative error} = 1 - \frac{\frac{\Delta\delta}{2}\sin\delta_o}{\left(\cos\delta_o - \cos\left(\delta_o + \frac{\Delta\delta}{2}\right)\right)} \tag{4.7}$$

where $\Delta\delta = \frac{w}{r}$ is the change in contact angle in the contact patch, $r$ is the radius of the rail profile, $w$ is the lateral width of the contact patch and $\delta_0$ is the contact angle at the

reference point. The resulting relative error is shown in Table 4.1. The relative error is larger when the change in contact angle in the contact patch is larger, and smaller for a larger contact angle at the reference point. Two cases are discussed: tread contact and gauge corner contact.

In tread contact, the contact is at the rail top, where the rail radius is 300 mm for a UIC60 profile. At the rail top, the lateral width of the contact patch is 10-40 mm resulting in a change in contact angle, $\Delta\delta$, of $2-7°$. The contact angle, $\delta_o$, is small and depends mainly on the conicity of the wheel profile and the rail inclination, typically between 1.4° and 2.8°. Table 4.1 illustrates that the relative error is 20-40% for this contact angle ant contact angle difference. Because of the small contact angle, the geometric spin in the contact patch is small, resulting in a small rigid body slip.

The local radius is smallest at the gauge corner: 13 mm for a UIC60 profile. At the gauge corner, the contact angle is large, but the contact patch is narrow (typically between 1 and 6 mm) in the lateral direction due to the small local rail radius. This results in a change in the contact angle of $4.5-26°$. The relative error of the rigid body slip will be 10-30%. As typical contact angles are large (i.e., $20-50°$), the geometric spin and the rigid body slip are large; therefore, the absolute error is larger than for the railtop case.

Real rail profiles do not have constant curvature; as a result a contact patch always spans a range of curvature, especially in gauge corner contact. Furthermore, when multiple-point contact occurs, the sub-contact patches are likely to have very different local rail radii. They also span a larger lateral distance, leading to a higher relative error when planar contact is assumed.



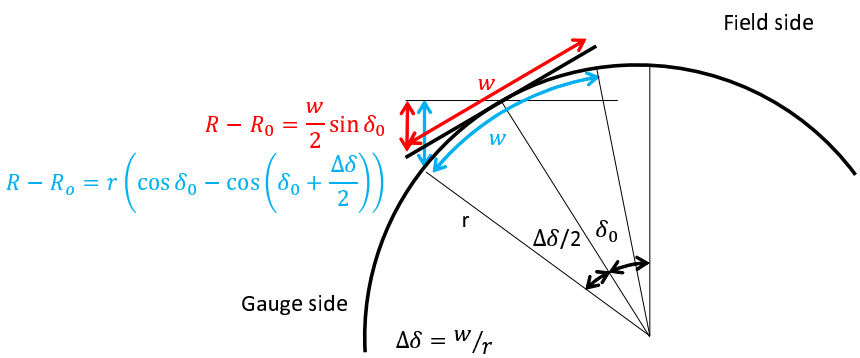


(a)

Figure 4.4: The difference in rolling radius between the edge of a contact patch and the middle, assuming planar contact (red) and conformal contact (blue)

Table 4.1: Relative error (4.7) in percent of the longitudinal rigid body slip due to spin calculated when assuming planar contact.

| $\delta_0 \setminus \Delta\delta$ | 2.5° | 5° | 10° | 15° | 20° | 25° | 30° |
|---|---|---|---|---|---|---|---|
| 2.5° | 20.0 | 33.3 | - | - | - | - | - |
| 5° | 11.1 | 19.9 | 33.2 | 42.7 | - | - | - |
| 10° | 5.82 | 11.0 | 19.7 | 26.9 | 32.8 | - | - |
| 15° | 3.90 | 7.50 | 13.9 | 19.4 | 24.2 | 28.4 | - |
| 20° | 2.90 | 5.63 | 10.6 | 15.0 | 19.0 | 22.5 | 25.7 |
| 25° | 2.28 | 4.44 | 8.45 | 12.1 | 15.4 | 18.4 | 21.1 |
| 30° | 1.85 | 3.61 | 6.91 | 9.94 | 12.7 | 15.3 | 17.6 |
| 40° | 1.28 | 2.50 | 4.83 | 6.98 | 8.98 | 10.8 | 12.6 |
| 50° | 0.899 | 1.77 | 3.41 | 4.94 | 6.36 | 7.69 | 8.91 |

#### THE LATERAL RIGID BODY SLIP

The relative error on the lateral rigid body slip can be calculated from Equations (4.3) and (4.5):

$$\textbf{relative error} = 1 - \frac{\sin\delta_o}{\sin\left(\delta_o + \frac{\Delta\delta}{2}\right)} \tag{4.8}$$

Unlike for the longitudinal rigid body slip, the relative error on the lateral rigid body slip can be calculated without the assumption of a rail with constant radius. The resulting relative error is shown in Table 4.2. Similar as for the longitudinal rigid body slip, the relative error is larger when the change in contact angle in the contact patch is larger and smaller for a larger contact angle at the reference point.



Table 4.2: Relative error (4.8) in percent of the lateral rigid body slip due to spin calculated when assuming planar contact.

| $\delta_0 \setminus \Delta\delta$ | 2.5° | 5° | 10° | 15° | 20° | 25° | 30° |
|---|---|---|---|---|---|---|---|
| 2.5° | 33.3 | 50.0 | - | - | - | - | - |
| 5° | 19.9 | 33.2 | 49.8 | - | - | - | - |
| 10° | 11.0 | 19.8 | 32.9 | 42.3 | 49.2 | - | - |
| 15° | 7.50 | 13.9 | 24.3 | 32.4 | 38.8 | 43.9 | - |
| 20° | 5.63 | 10.6 | 19.1 | 25.9 | 31.6 | 36.3 | 40.4 |
| 25° | 4.45 | 8.47 | 15.5 | 21.3 | 26.3 | 30.6 | 34.3 |
| 30° | 3.62 | 6.94 | 12.8 | 17.9 | 22.2 | 26.0 | 29.3 |
| 40° | 2.51 | 4.85 | 9.10 | 12.8 | 16.1 | 19.0 | 21.5 |
| 50° | 1.77 | 3.44 | 6.48 | 9.17 | 11.5 | 13.6 | 15.5 |

### 4.4.2. COMPARISON WITH CONTACT

To assess the ability of WEAR to treat conformal contact, a case with two-point contact has been investigated (see Figure 4.5). The undeformed situation of the two sub-contact patches is indicated by the two penetrations of the wheel and rail profiles. The rail has a worn UIC60 profile with a 1/40 rail inclination, whereas the wheel has a worn S1002 pro-

file. The contact angle varies between 8° and 15° in the sub-contact area on the top of the rail, whereas the contact angle varies between 17° and 35° in the sub-contact area at the gauge corner. To highlight the effect of the changing geometrical spin, the longitudinal and lateral creepages are set to zero. The coefficient of friction is set at 0.4.

The field of local slip (**s** in Equation (4.6)) in the contact patch is shown in Figure 4.6. The shapes of the contact patch and adhesion zone are similar for CONTACT and WEAR. In section 4.2.2.1, it was concluded that the longitudinal slip is higher on the gauge side of the reference point and lower on the field side for non-planar contact. WEAR chooses the explicit contact point as the reference point. Here, the reference point is in the sub-contact patch at the field side. This situation is most common because the explicit contact point is where the compression and thus the contact pressure are largest; the major wheel load is typically carried, at the contact point closest to the field side (i.e., the rail head). The error that CONTACT makes by assuming planar contact will be largest when furthest away from the reference point, which is at points A and B in Figure 4.6. Because there is more contact on the gauge side of the reference point in this case, CONTACT underestimates the overall longitudinal slip. In Figure 4.5b, the rolling radius difference between the reference point and the extreme point A in Figure 4.6a is 4.5 mm, whereas the horizontal distance between those points is 14 mm, and the contact angle at the reference point is 10°. From this figure and Equations (4.2) and (4.4), the relative error in the longitudinal rigid body slip can be calculated as 45%. On the gauge corner at the extreme point B (Figure 4.6b) on the edge, the local longitudinal slip obtained with CONTACT is 37% lower (i.e., 0.174 m/s) than that obtained with WEAR (i.e., 0.278 m/s) at point A in Figure 4.6a with a rolling speed of 20 m/s. This indicates that the relative error of the longitudinal local slip from the contact methods is close to the relative error of the longitudinal rigid body slip from the calculations.

The error in the lateral rigid body slip is also largest when furthest away from the reference point in lateral direction. The absolute error is largest when furthest away from the reference point in longitudinal direction (i.e., points C and D in Figures 4.6a and 4.6b). From equations (4.3) and (4.5) and with the contact angle of 10° at the reference point and 30° at the extreme point C in Figures 4.6a, the relative error in the lateral rigid body slip is 58%. On the gauge corner at the extreme point D (Figure 4.6b) at the edge the lateral local slip obtained with CONTACT is 60% lower (i.e., 0.066 m/s) than that obtained with CONTACT (i.e., 0.17 m/s) (Point C in Figure 4.6a) with a rolling speed of 20 m/s. As in the lateral case, the relative error of the rigid body slip is close to that of the resulting local slip.

The difference in slip explains the absence of an adhesion area with WEAR at the gauge corner, whereas a small adhesion area in the contact area still exists at the gauge corner calculated with CONTACT. The difference in tangential traction, as shown in Figure 4.7, is considerably smaller because the contact patch is mainly in slip; this limits the tangential traction is to the traction bound and does not depend on the local rigid body slip. The local frictional work is the product of the local slip and local tangential stress; therefore, the same conclusion as for the local slip can be extended to frictional work: CONTACT underestimates the local frictional work in the contact patch at the gauge corner by approximately 60%. The wear rate is also underestimated by CONTACT when assuming that the wear rate is proportional to frictional work.

The reference point will typically be on the rail head when contact appears simultaneously at the rail head/shoulder and the gauge corner because it is the rail head that carries the major load. From this consideration and section 4.2.2.1, it can be concluded that CONTACT typically underestimates the slip for normal operation.

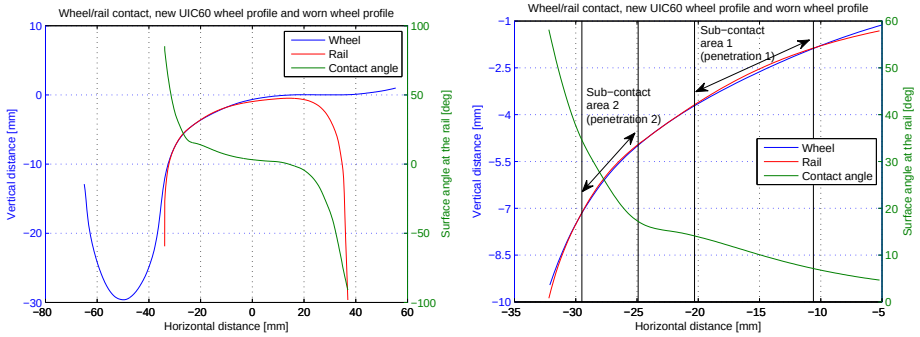


(a) (b)

Figure 4.5: The wheel and rail profiles in the case of a conformal contact with two-point contact indicated by the penetrations between the wheel and rail profiles: (a) an overview and (b) a zoom-in of the contact area. The worn and inclined rail profile is in red, the wheel in blue and the contact angle on the undeformed rail profile in green.

### 4.4.3. ROBUSTNESS TEST WITH A VEHICLE DYNAMIC SIMULATION IN A TURNOUT WITH NOMINAL WHEEL/RAIL PROFILES

To assess the robustness of WEAR for dynamic simulations of vehicle-track interaction, the passage of the vehicle coasting through the UIC1:15 turnout at 20 m/s was simulated with VIRail. The simulation was defined to run 20 m in 10,000 timesteps so that the contact patch moves approximately 2 mm forward with each timestep. The memory consumption of WEAR is small, around 15 Mb, therefore the new method can run on any presently available computer. The computational time of one contact force evaluation is 0.08 s, which means that the total computation time for this simulation is 800 s per wheel/rail contact pair. It would be beneficial to use WEAR for the wheels where conformal contact or multiple point contact is expected while using a traditional method, such as FASTSIM, for the other wheels. Or use FASTSIM on simple parts of the tracks (i.e. straight sections), while using WEAR at places where complex contact conditions are expected. The transition from one contact model to another in a vehicle dynamic simulation could be part of a future study.

The coefficient of friction was set to 0.4 for this simulation. The resulting creepages (see in Figure 4.8a) and the normal force (see Figure 4.8b) are used as inputs for the WEAR simulation.

Due to the absence of cant in turnouts, the lateral force is higher than in normal curves. Consequently, the wheel/rail contact is always fully flanging in the curve of a turnout. High-frequency peak creepage (see Figures 4.8a and 4.8b), at 31 m occurs on

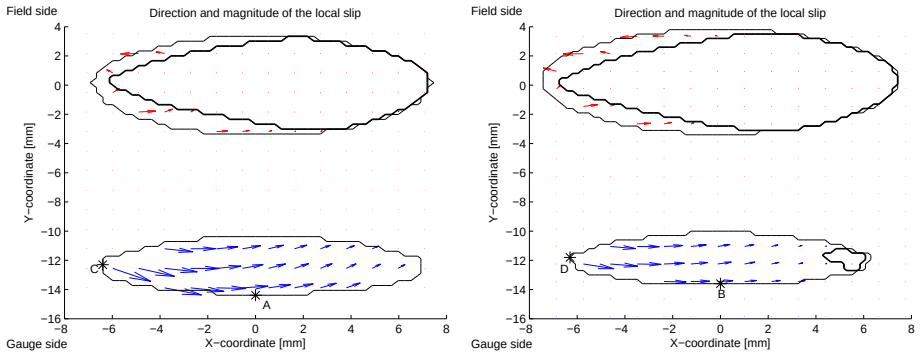


(a) (b)

Figure 4.6: Direction and magnitude of the local micro slip. The direction of the arrows indicates the direction of the local slip in the contact patch calculated with WEAR (a) and with CONTACT (b). The length of the arrows is proportional to the magnitude of the slip, but a different scale is used for the contact patch on the field side (red arrows) and for the contact patch on the gauge side (blue arrows). For the same arrow length, the local slip is half as large in the contact patch on the gauge side (blue arrows). The difference in scale is used to make the red arrows more visible. The directions of the red arrows are less regular, which is likely due to their small magnitude, resulting in more visible numerical error. The thin curves enclose the contact area, whereas the thick curves enclose the adhesion area. Within the contact area but outside the adhesion area is the slip area. The y-coordinate is positive toward the field side and negative toward the gauge side.

the impact of the wheel/rail (i.e., where the wheel flange hits the switch blade at the blade tip). Even with this peak, WEAR converged for the contact case of each timestep of the simulation. Figure 4.9 shows the creep forces calculated with WEAR and FASTSIM. The results from WEAR and FASTSIM are extremely close to each other on the tangent part of the track before the turnout (i.e., to the left of 30 m) and after the wheel has been transferred from the stock rail (i.e., right of 31 m). There is a difference between the two contact methods at the moment when the wheel flange hits the switch blade (see Figure 4.10): WEAR predicts the initiation of two-point contact at position 30.7 m, whereas FASTSIM predicts this at position 30.8 m.

One of the differences between WEAR and CONTACT is that WEAR predicts a non-zero longitudinal creep force while the vehicle is still on the straight track, where the lateral and longitudinal creep forces are zero (i.e., the pure spin case) (see Figure 4.9a). This prediction occurs because the contribution of the spin to the longitudinal creep force is zero if the contact patch has two axes of symmetry, which is the case for the elliptical contact patches from FASTSIM but not for WEAR.

### 4.4.4. APPLICATION TO TYPICAL CONTACT SITUATIONS IN TURNOUTS

To test the performance of WEAR's contact calculation, it is applied to four typical positions along the 1:15 turnout. Figure 4.11 presents the four positions: case (1) is on tangent track just before the turnout; case (2) is at the point where the switch blade and the wheel flange initially make contact, where the load is mainly carried by the stock rail;

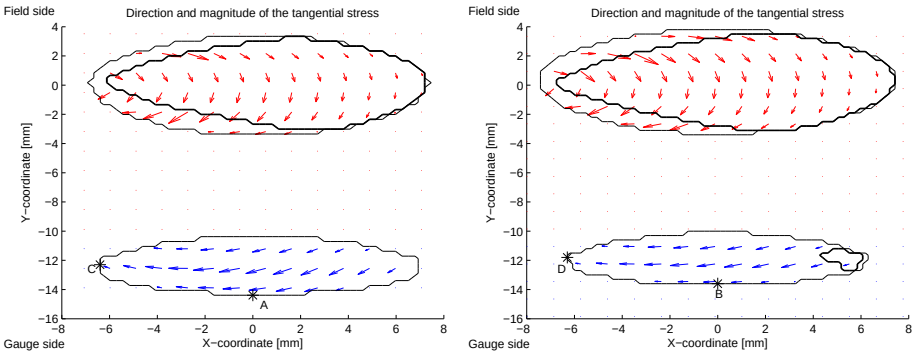


(a) (b)

Figure 4.7: Direction and magnitude of the tangential stress. The direction of the arrows indicates the direction of the tangential stress in the contact patch calculated with WEAR (a) and with CONTACT (b). The length of the arrows is proportional to the magnitude of the slip, but a different scale is used for the contact patch at the field side (red arrows) and for the contact patch at the gauge side (blue arrows). For the same arrow length, the tangential stress is half as large on the contact patch on the gauge side (blue arrows). The thin curves enclose the contact area, whereas the thick curves enclose the adhesion area. The slip area is within the contact area but outside the adhesion area. The y-coordinate is positive toward the field side and negative toward the gauge side.

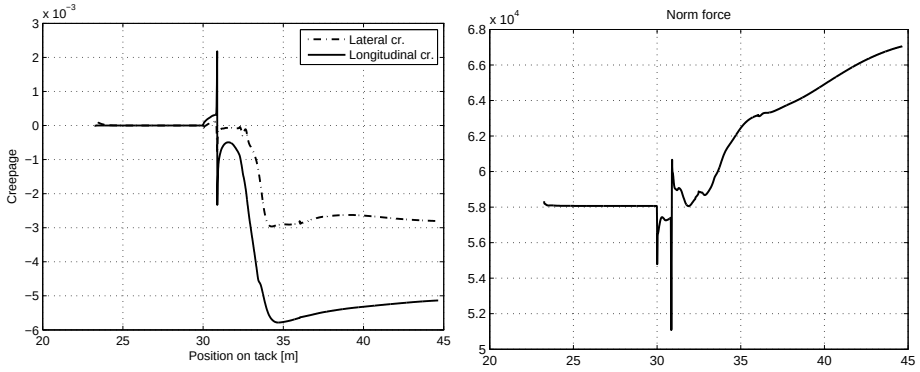


(a) (b)

Figure 4.8: Lateral and longitudinal creepages (a) and the normal contact force (b) on the outer rail in a UIC1:15 turnout for a vehicle coasting through the turnout at 20 m/s, taking the diverging route, as calculated with Vehicle Dynamics Software VIRail. The point of the switch blade is at 30 m; at 34 m, the rail profile stops changing and is again the same as that of a normal rail.

case (3) is further down the track, where there is still two-point contact but now the load is mainly carried by the switch blade; and case (4) is in the middle of the turnout, where the wheelset is curving steadily and all transient phenomena have faded away.

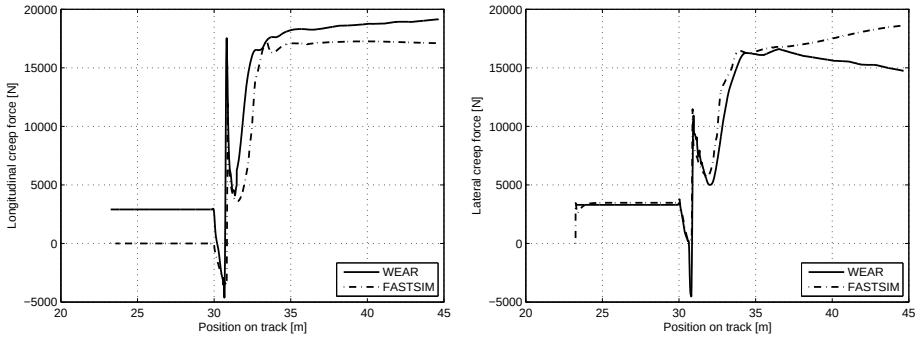


(a) (b)

Figure 4.9: Longitudinal (a) and lateral (b) creep forces in a UIC1:15 turnout calculated with WEAR and FASTSIM. The switch blade starts at 30 m.

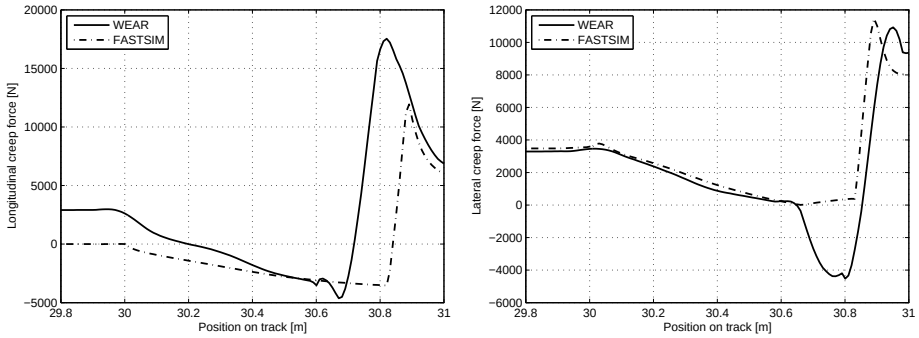


(a) (b)

Figure 4.10: Longitudinal (a) and lateral (b) creep forces in a UIC1:15 turnout, shown as a zoom-in of Figure 4.9 at the transition from the stock rail to the switch blade calculated with WEAR and FASTSIM. The switch blade starts at 30 m.

Figure 4.12 presents the shapes of the contact patches and the normal pressure distributions for all four cases. In case (1), the contact is on the rail head with a contact angle of 3.2°. In case (4), the contact is at the gauge corner with a contact angle of 25.3°. In both cases (1) and (4), there is only one contact point, and the contact patch is almost elliptical. Thus using a Hertzian method would have been sufficient to calculate the contact stresses. Cases (2) and (3) are the transition from case (1) to (4).

Cases (2) and (3) are further analyzed. Figure 4.13 shows the wheel/rail interface for case (2) when the wheel flange has just made contact with the switch blade. From the wheel profile and rail profile at that position, two-point contact is expected with the two contact patches approximately 35 mm apart; this is indeed the case, as shown in Figure


Figure 4.11: The positions of the four cases in the turnout: (1) before the turnout on a tangent track; (2) at the point where the wheel first makes contact with the switch blade; (3) on the switch blade; and (4) in the turnout when all transient phenomena have faded out.

4.12b. The origin of the axes in Figure 4.12b is at the explicit contact point. The contact angle at the contact point on the head of the stock rail is 3.5°, whereas the contact angle at the contact point on the switch blade is 30°. The contact pressure of the contact point on the switch blade is small compared to the contact pressure on the stock rail, so most of the load is carried by the stock rail. Therefore, the explicit contact point is on the stock rail. The low normal pressure on the switch blade together with the large spin due to the change in contact angle between the reference point and gauge corner explains why the implicit contact point is fully in slip (see Figure 4.13) where the tangential traction at the implicit contact is proportional to the corresponding normal stress everywhere when using the coefficient of friction as the scaling factor; the wheel rotates around the contact point on the stock rail.

Figure 4.14 shows the contact situation for case (3) in Figure 4.11. At this position, the cross section of the switch blade is wider than for case (b), and the top of the switch blade is only 0.5 mm lower than the top of the stock rail. There is still two-point contact, but now, most of the load is carried by the switch blade as shown in Figure 4.12c. The contact angle at the switch blade is 4.8°. Figure 4.14a illustrates that there a small amount of slip at that contact point, whereas the contact point on the stock rail is almost fully in slip; this occurs because the contact pressure is considerably lower on the stock rail than on the switch blade. The shape of the tangential stress distribution on the switch blade in Figure 4.14a is somewhat irregular because the width of the contact patch in the lateral direction is small compared to the width of the potential contact patch. Therefore this case has been redone with a higher number of elements in the contact patch (15360: 640 in lateral direction, 24 in longitudinal direction). Refining the resolution had negligible influence on the creep forces.

This analysis shows that WEAR is able to solve the contact problems for all four typical cases that can be found in wheel/rail contact in turnouts. It is capable of finding multiple contact points that occur at complex rail profiles, such as those in turnouts.

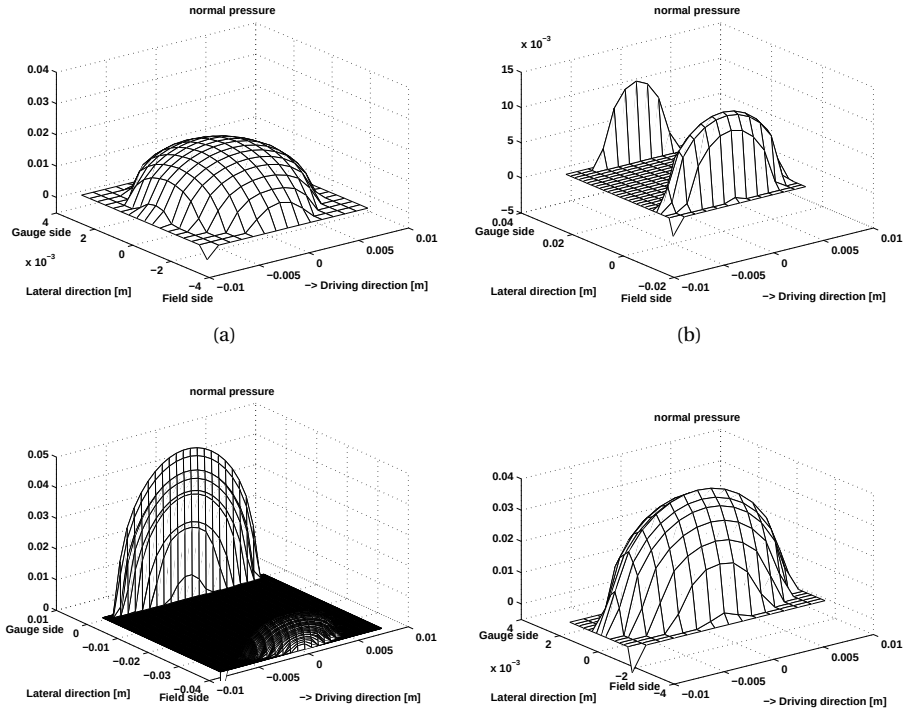


Figure 4.12: The normal pressure distribution in the contact patch for all cases in Figure 4.11. The contact area dimensions are in m, whereas the pressure is normalized with the shear stiffness of 81.3 GPa so that it is dimensionless.



The next step in the research will be to use WEAR to calculate the rail wear rate using local frictional work. These calculations will then be compared with wear observations and profile measurements in the field for validation.

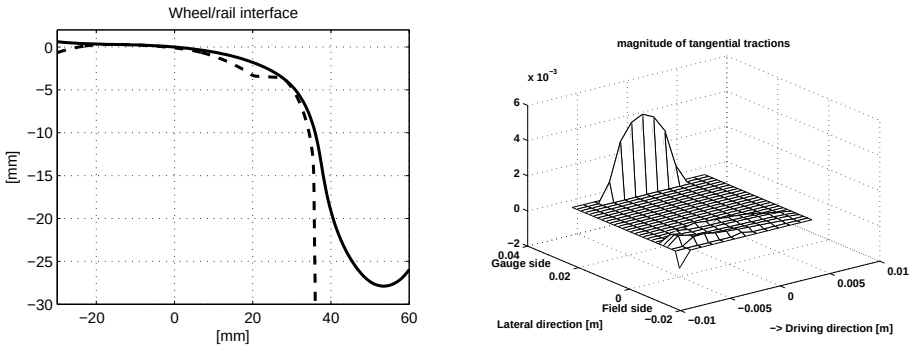


(a) (b)

Figure 4.13: The wheel (full line) and rail (dashed line) profiles for case (2) in Figure 4.11 with contact on the railhead of the stock rail and on the side of the switch blade (a). (b) shows the magnitude of the tangential traction at that location. The traction is normalized with the shear stiffness of 81.3 GPa. The values on the horizontal axes are in m.

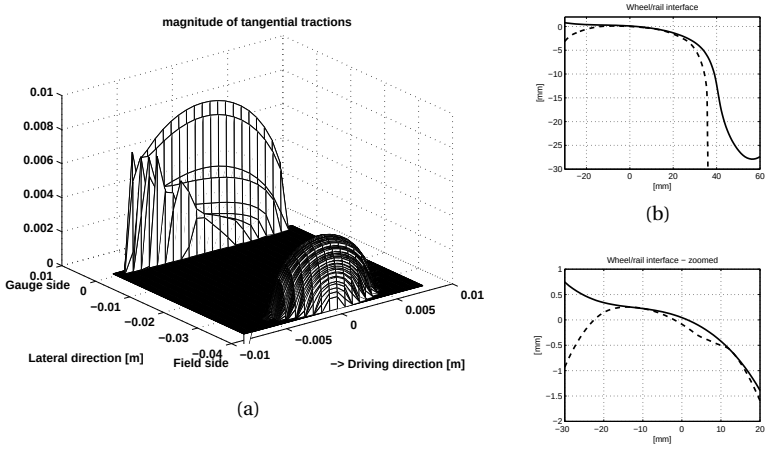


(a) (b) (c)

Figure 4.14: The magnitude of the tangential traction (a) for case (3) indicated in Figure 4.11. The traction is normalized with the shear stiffness 81.3 GPa. The dimensions of the contact area are in m. The wheel (solid line) and rail (dashed line) profile for case (3) in Figure 4.11 with contact on the railhead of the stock rail and on the side of the switch blade are shown in: (b) overview of the contact and (c) a zoom-in at the contact points. The horizontal and vertical axes do not have the same scale.

## 4.5. CONCLUSIONS

The program WEAR was used to calculate the creep forces in multiple cases, including conformal contact and the contact between the wheel and switch blade of a turnout.

WEAR was compared with CONTACT for the case of conformal contact. First, the

difference in the calculation of the longitudinal rigid body slip between WEAR and CONTACT was compared analytically and demonstrated with a theoretical case of a rail with a constant rail radius. The relative error in the calculation of the longitudinal rigid body slip is 10-40% when assuming a planar contact patch, whereas the relative error on the lateral rigid body slip is 10-50%. Second, the case with real wheel and rail profiles was investigated. This case had contact angles ranging from 8° to 35°. The results show that the way in which the rigid body slip is calculated has a significant influence on the lateral local slip (i.e., up to 60%) and longitudinal local slip (i.e., up to 37%). In the case of two-point contact with contact on the rail head and gauge corner, CONTACT underestimates of the local slip at the contact patch on the gauge side.

WEAR has shown to be able to capture and solve two-point contact problems occurring when the wheel transfers from the stock rail to the switch blade. It can also capture an implicit (sub-)contact patch. The creep forces and shapes of the contact areas calculated with WEAR are reasonable and realistic. Moreover, WEAR converged in all cases; this robustness is required if the method is to be applied to online creep force calculations in vehicle dynamics simulations. While it has been successfully applied, by integrating into a combined model of vehicle dynamics and RCF initiation, to the analysis of RCF on a normal track curve, its application to RCF in turnouts would be the next step. Another next step can be to use WEAR, coupled with a vehicle dynamics model, to simulate the wear of wheel and rail profiles, both in normal curves and in turnouts. Special attention will be given to conformal contact. The wear will be assumed to be proportional to the frictional work, which can be computed readily from the outputs of WEAR, the local tangential stress and micro-slip. This will allow to compare a simulated wheel/rail profile evolution with wear observations in tracks. The combinations of WEAR with RCF or wear models, including conformal contact, will be validated by comparing with controlled laboratory test. The new method, with a more accurate calculation of stress and micro slip, can also be used to obtain an better estimate of the energy dissipation in the wheel rail contact, which can be compared with experimentally acquired values. A direct numerical validation can be done by comparing with results obtained with a finite element model, such as that of [15].

In future work, the creep force calculation with WEAR will be conducted online in vehicle dynamics simulations. A dynamic coupling between the new contact model and the vehicle simulation will allow to evaluate the influence of the contact model on the wheelset's motion, and so obtain more accurate values for both the creepages and the tangential stress in the contact patch. This approach can be applied to obtain a better estimate of the rail wear and energy consumption in tight curves or to get a better estimate of the stability of a vehicle traveling of an track with irregularities. creep forces. A better estimate of the creep force is also important when considering derailment at switch blades.



## 4.6. ACKNOWLEDGMENT

This research was partially supported by the Dutch Technology Foundation STW, which is part of the Netherlands Organization for Scientific Research (NWO), and is partly funded by the Ministry of Economic Affairs. This work was partially supported by the Dutch railway infrastructure manager ProRail.

## REFERENCES


[1] N. Burgelman, Z. Li, and R. Dollevoet, *A new rolling contact method applied to conformal contact and the train-turnout interaction,* Wear **321**, 94–105 (2014).

[2] H. Grausse and G. Poll, *Wear of wheel-rail surfaces,* Wear **113**, 103–122 (1986).

[3] A. Ekberg, B. Akesson, and E. Kabo, *Wheel/rail rolling contact fatigue - probe, predict, prevent,* Wear **314**, 2–12 (2014).

[4] Y. Zhou, S. Wang, T. Wang, Y. Xu, and Z. Li, *Field and laboratory investigation of the relationship between rail head check and wear in a heavy-haul railway,* Wear **315**, 68–77 (2014).

[5] G. Donzella, M. Faccoli, A. Ghidini, A. Mazzu, and R. Roberti, *The competitive role of wear and rcf in a rail steel,* Engineering Fracture Emchanics **72**, 287–308 (2005).

[6] J. J. Kalker, *Rolling with slip and spin in the presence of dry friction,* Wear **9**, 20–38 (1966).

[7] J. J. Kalker, *The tangential force transmitted by two elastic bodies rolling over each other with pure creepage,* Wear **11**, 421–430 (1968).

[8] J. J. Kalker, *Three Dimensional Elastic Bodies in Rolling Contact* (Kluwer Academic Publishers, 1990).

[9] S. Alfi and S. Bruni, *Mathematical modeling of train-turnout interaction,* Vehicle System Dynamics **47**, 551–574 (2009).

[10] J. J. Kalker, *Simulation of the development of a railway wheel profile through wear,* Wear **150**, 355–365 (1991).

[11] E. Kassa, C. Andersson, and J. Nielssen, *Simulation of dynamic interaction between train and railway turnout,* Vehicle System Dynamics **44**, 247–258 (2006).

[12] X. Shu, N. Nilson, C. Sasaoka, and J. Elkins, *Development of a real-time wheel/rail contact model in nucars and apllication to diamond crossing and turnout design simulations,* Vehicle System Dynamics **44**, 251–260 (2006).

[13] M. Wiest, E. Kassa, W. Daves, and J. Nielsen, *Assessment of methods for calculating contact pressure in wheel-rail/switch contact,* Wear **265**, 1439–1445 (2008).

[14] T. Telliskivi and U. Olofsson, *Contact mechanics analysis of measured wheel-rail profiles using the finite element method,* Rail and Rapid Transit **215**, 65–72 (2001).

[15] X. Zhao and Z. Li, *The solution of frictional wheel-rail rolling contact with a 3d transient finite element model: validation and error analysis,* Wear **271**, 444 (2011).

[16] A. Shabana, K. Zaazaa, J. Escalona, and J. R. Sany, *Development of elstic force model for wheel-rail contact problems,* Journal of Sound and Vibration **269**, 295–325 (2004).

[17] S. Falomi, M. Malvezzi, E. Meli, and A. Rindi, *Determination of wheel-rail contact points: comparison between classical and neural network based procedures,* Meccanica **44**, 661–686 (2009).

[18] S. Falomi, M. Malvezzi, and E. Meli, *Multibody modeling for railway vehicles: Innovative algorithms for the detection of wheel-rail contact points,* Wear **271**, 453–461 (2011).

[19] J. Piotrowski and H. Chollet, *Wheel/rail contact models for vehicle system dynamics including multi-point contact,* Vehicle system dynamics **43**, 455–483 (2007).

[20] P. Shackleton and S. Iwnicki, *Comparison of wheel/rail contact codes for railway vehicle simulation: An introduction to the manchester contact benchmark,* Vehcile system dynamics **46**, 129 (2008).

[21] S. Magheri, M. Malvezzi, E. Meli, and A. Rindi, *An innovative wheel-rail contact model for multibody applications,* Wear **271**, 462–471 (2011).

[22] A. Alonso and J. Giménez, *Wheel-rail contact: Roughness, heat generation and conforming contact influence,* Tribology International **41**, 755–768 (2008).

[23] A. Bhaskar and K. Johnson, *Wheel-rail dynamics with closely conformal contact. part 1: dynamic modelling and stability analysis,* Proceedings of the Institution of Mechanical Engineers, Part F: Journal of Rail and Rapid Transit **211**, 11–26 (1997).

[24] K. L. Johnson, *Contact Mechanics* (Cambridge University Press, 1985).

[25] J. Ayasse and H. Chollet, *Determination of the wheel rail contact patch for semihertzian conditions,* Vehicle System Dynamics **43**, 159–170 (2005).

[26] Z. Li and J. Kalker, *Simulation of severe wheel-rail wear,* in *Proc. the Sixth International Conference on Computer Aided Design, Manufacture and Operation in the Railway and Other Mass Transit Systems* (1998) p. 393–402.

[27] Z. Li, *Wheel-Rail Rolling Contact and its Application to Wear Simulation*, Ph.D. thesis, Delft University of Technology (2002).

[28] R. Dollevoet, Z. Li, and O. Arias-Cuevas, *A method for the prediction of head checking initiation location and orientation under operational loading conditions,* Proc. IMechE, Part F: J. Rail and Rapid Transit **224**, 369–374 (2010).

[29] A. Rovira, A. Roda, M. Marshall, H. Brunskill, and R. Lewis, *Experimental and numerical modelling of wheel-rail contact and wear,* Wear **271**, 911–924 (2011).

[30] O. Arias-Cuevas, Z. Li, and C. Esveld, *Simulation of the lateral dynamics of a railway vehicle and its validation based on rail wear measurements,* in *Proceedings of the ECCOMAS Thematic Conference on Multibody* (2007).

[31] E. Kassa and J. Nielssen, *Dynamic train-turout interaction in an extended frequency range using a detailed model of track dynamics,* Journal of Sound and Vibration **320**, 893–914 (2009).

# 5

# CALCULATION OF THE FRICTIONAL ENERGY

Sections 5.5.2 and 5.6 of this chapter were realized in a cooperation with Guillermo Idárraga Alarcón, Juan Meza and Alejandro Toro from the National University of Colombia, Medellin [1].

## 5.1. INTRODUCTION

The frictional energy dissipated in the wheel/rail contact can be calculated using one of the wheel-rail contact methods available in the literature in two ways: from a rigid body point of view (the $T\gamma$ approach) or from a local stress-slip point of view . These two approaches can be applied in combination with different wheel/rail contact methods. In this chapter we will analyze the frictional energy obtained through two widely used contact methods: FastSim [2] and Kalker's full theory [3].

One of the difficulties of studying wheel/rail contact is the limited possibility of validating the theoretical approaches. Wheel/rail contact forces can be measured in the following manners: from an instrumented wheelset [4, 5], from a twin disk experiment [6, 7], or from the displacements in the primary suspension [8].

The frictional energy can be used in a direct and in an indirect way to validate the wheel/rail contact theories. In a direct way, the energy dissipation from the theories can be compared to measured energy dissipation. It is not possible to directly measure the energy dissipated in the wheel/rail contact, there are two indirect ways. First, the energy dissipation can be estimated from the measured deceleration of a train coasting through a curveOr by measuring the coupler forces to a trailing wagon. The first method has been successfully applied to freight trains in Sweden [9, 10], while the second method was applied to evaluate the effectiveness of friction modifiers to reduce the energy consumption in [11]. The drawback of this method is that it does not allow for traction, while traction has a substantial influence on the slip and stress in the wheel rail contact and so energy dissipation. A second method is to measure the electrical energy consumed by the train engine. This can be achieved by measuring the electric current, as the voltage is often constant. This method is cheap and easy. The difficulty here is that the energy from the engine is not only dissipated in the wheel/rail contact but also in the train acceleration (kinetic energy), the change in altitude (potential energy), among other sources of dissipation. However, in the case of a train curving at a constant speed on a track without slope, it can be assumed that the energy dissipation in the wheel/rail contact will be dominant. For other scenarios the kinetic and potential energy can be compensated for by calculation (see Section 5.6).



An indirect way of wheel/rail contact validation through frictional energy is via wear observations. There are empirically proven relations between the frictional energy and the wear rate [12, 13], so observations of the wear rate and wear distribution along the wheel and the rail profiles can be compared with the frictional energy distribution obtained from wheel/rail contact solutions.

In this chapter we analyze several methods for calculating the frictional energy dissipated in the wheel/rail contact (Section 5.3) and compare the frictional power obtained through simulation (Section 5.5 and 5.4) and from measurements (Section 5.6).

## 5.2. VEHICLE AND TRACK MODEL

The vehicle model for the simulation and the measurements is a three-car train from the metro of Medellin described in [1]. The first and the last car can apply traction on all the four axles while the middle car is trailing. The simulations and measurements have focused on the passage of the train through one specific curve of the metro line, a

curve with a radius of 300 m (see [1]). In this curve the train is accelerating in normal operations.

## 5.3. METHODS FOR THE CALCULATION OF THE FRICTIONAL ENERGY

The frictional energy dissipated in the wheel/rail contact can be calculated from a rigid body point of view in which we consider the contact between wheel and rail as one point. At this point the relative slip velocity, the total resultant contact force and moment between the two bodies need to be known. The frictional power, $P_{T\gamma}$, is often calculated as [13]:

$$P_{T\gamma} = (F_x v_x + F_y v_y) V \tag{5.1}$$

where $V$ is the train velocity, $F_x$ and $F_y$ are the longitudinal and lateral creep force, respectively, and $v_x$ and $v_y$ are the longitudinal and lateral creepages. This formula is widely used as it is simple and requires only few input variables. The required creep forces can be calculated if the creepages are known (e.g. online in a vehicle dynamic simulation) or can be estimated with the use of quasi-statics [14]. Traditionally, the creep forces required by the $T\gamma$-method are calculated using FastSim, but other methods such as Kalker's full can be used as well.

An extension of this approach is to include the moment that is produced in the wheel/rail contact due to spin creepage. This moment is not calculated in most contact methods that are designed to operate within vehicle dynamic simulations, because its influence on the wheelset's motion is negligible. For frictional energy considerations, however, this moment can be significant. Common algorithms such as FastSim can be adapted to calculated this moment (Section 5.3.1). The dissipated power, $P_{T\gamma S}$, then becomes:

$$P_{T\gamma S} = (F_x v_x + F_y v_y + M_z \psi) V \tag{5.2}$$

where $M_z$ is the moment about the normal at the contact point and $\psi$ is the spin creepage.

The third possibility for calculating the dissipated energy is based on the local stress and slip in the wheel/rail contact area. In each point of the contact area the local frictional power can be calculated, which then can be integrated over the contact area:

$$P_{SS} = \iint_A (\sigma_x s_x + \sigma_y s_y) \mathrm{d}A \tag{5.3}$$

where $\sigma_x$ and $\sigma_y$ are the local tangential contact stresses, $s_x$ and $s_y$ are the local slip, and $\mathrm{d}A$ is the area of a contact element. FastSim in its original form, does not calculate the slip [2], but this can be included using the same assumptions employed for the method itself (Kalker's simplified theory) (see Section 5.3.1). In Kalker's full theory the slip is included in the standard output [3].

### 5.3.1. FRICTIONAL ENERGY WITH FASTSIM

FastSim is based on the simplified theory of Kalker [2]; its two main assumptions are:

- the tangential contact stress $\boldsymbol{\sigma}$ is proportional to the local tangential displacement $\mathbf{u}$:

$$\mathbf{u} = L\boldsymbol{\sigma} \tag{5.4}$$

where $L$ is the flexibility parameter. Values can be found in [15].

- the tangential stress at the leading edge is zero; from there the algorithm proceeds in the longitudinal direction and builds up the stress. This is done line by line in the lateral direction till the whole contact area is covered.

We adapted the formulas from [15]; in each element (i,j):

- Assume there is no slip, $\mathbf{s}(i,j) = 0$
- Calculate the tangential stress as:

$$\boldsymbol{\sigma}(i,j) = \boldsymbol{\sigma}(i-1,j) - \frac{k}{L}\mathbf{c}(i,j) \tag{5.5}$$

where $k = \frac{dx}{V}$, $L$ is the flexibility parameter and $\mathbf{c}$ is the rigid body slip.

- Check whether $\left|\boldsymbol{\sigma}(i,j)\right| \geq \mu p_z(i,j)$, where $p_z$ is the normal contact pressure and $\mu$ is the friction coefficient, if this logic expression is true the element is in slip else the element is in adhesion.
- In case of slip:

$$\boldsymbol{\sigma}(i,j) = \frac{\boldsymbol{\sigma}(i,j)}{\left|\boldsymbol{\sigma}(i,j)\right|}\mu p_z(i,j) \tag{5.6}$$

- In case of slip, the slip ($s$) equals:

$$\mathbf{s}(i,j) = \mathbf{c}(i,j) - \frac{\partial \mathbf{u}(i,j)}{\partial x}V = \mathbf{c}(i,j) - L\frac{\boldsymbol{\sigma}(i,j) - \boldsymbol{\sigma}(i-1,j)}{dx}V \tag{5.7}$$

else: $\mathbf{s}(i,j) = 0$

- Update the tangential forces and the moment

$$F_x = F_x + \sigma_x(i,j)dxdy \tag{5.8}$$

$$F_y = F_y + \sigma_y(i,j)dxdy \tag{5.9}$$

$$M_z = M_z + \left(\sigma_x(i,j)y - \sigma_y(i,j)x\right)dxdy \tag{5.10}$$

- go to the next element in the longitudinal direction (i=i+1). Once the trailing edge is reached: start with the next line in the lateral direction at the leading edge (j=j+1) with the tangential stress equal to zero.

## 5.4. COMPARISON OF METHODS FOR FRICTIONAL POWER

To compare the different methods of frictional power calculation we define a wheel/rail contact with lateral displacement of the wheelset of 3.5 mm, which means there is contact on the gauge corner of the rail where the contact angle is 35° (so a spin creepage of $1.26\,\mathrm{m}^{-1}$). The normal contact problem is solved with the Hertzian theory resulting in a contact ellipse of 17 mm in the longitudinal direction and 3.8 mm wide in the lateral direction. In Figure 5.1 the frictional power is shown without lateral creepage for a range of longitudinal creepages (Figure 5.1a) and without longitudinal creepage for a range of lateral creepages (Figure 5.1b). The friction coefficient was set to 0.4 and the train speed was 20 m/s. It can be seen that:

- the relative difference between the methods is large at small creepage. This probably related to inaccuracies in the slip/stress distribution calculate by FastSim.
- at zero lateral and longitudinal creepage the power calculated with the T$\gamma$ method without spin is zero, therefore in such cases one of the other methods has to be used.
- at higher creepages, the relative error between the methods becomes small. The absolute error, on the contrary, seems to remain constant, especially for the case without lateral creepage.
- at small creepages there is a small peak in the frictional power for the stress-slip method and the $T\gamma$ method with spin. This is probably related to the fact that FastSim has poor handling of cases where the spin creepage is the dominant creepage; reported in [16]
- at small lateral creepages the $T\gamma$-method without spin results in a negative power, however, when spin is included the frictional power is always positive. The underlying reason is that for creepages around zero, FastSim still predicts a lateral creep force which is caused by spin.

Figure 5.2 shows the same case calculated with Kalker's full theory. It can be seen that the frictional power with T$\gamma$ method with spin and the one with the stress-slip method are very close to each other. This is because the Kalker's full theory is based on the principle of virtual work [15], so that it ensures the energy conservation. Therefore the small difference between T$\gamma$ method with spin and the stress-slip method is attributed to numerical error. The difference with the T$\gamma$ method without spin is larger than it was with FastSim, it can therefore be concluded that when using Kalker's full theory for solving the contact problem there is no point in using equation 5.1.

To show the differences between FastSim and Kalker's full theory two cases are analyzed separately: pure spin and spin combined with a longitudinal creepage of 0.005. Figure 5.3 shows the local slip on the longitudinal line in the center of the contact area. As should be expected from the formulation of FastSim (see Section 5.3.1), the solutions found with FastSim have an adhesion zone (slip is zero) at the trailing edge (positive longitudinal position); for the case with pure spin this adhesion zone is smaller than for the case with longitudinal creepage. In the case of pure spin there is another adhesion zone

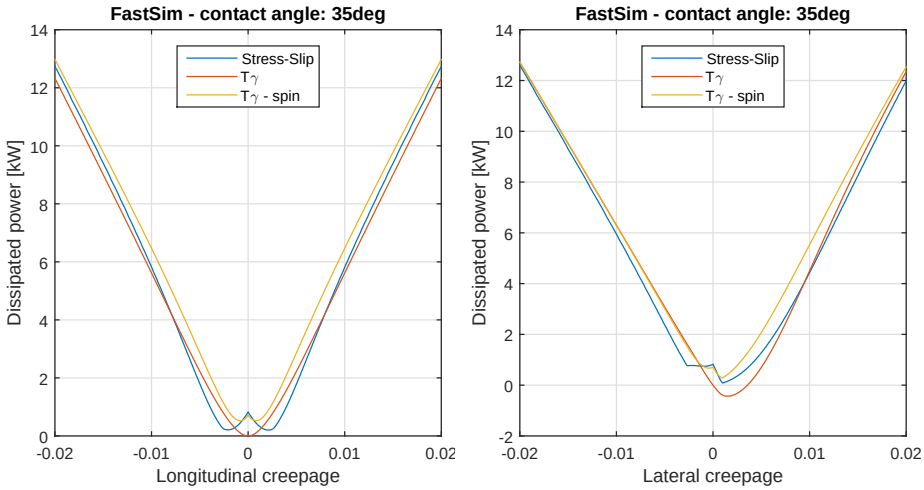


(a) (b)

Figure 5.1: The frictional power using the stress-slip method (Equation 5.3, stress and slip calculated using FastSim), T$\gamma$ method and T$\gamma$ method with spin (Equations 5.1 and 5.2, creep forces and moment calculated with FastSim), for a wheel-rail contact with a contact angle of 35°; (a) without lateral creepage and (b) without longitudinal creepage; with a friction coefficient of 0.4 and a train speed of 20 m/s

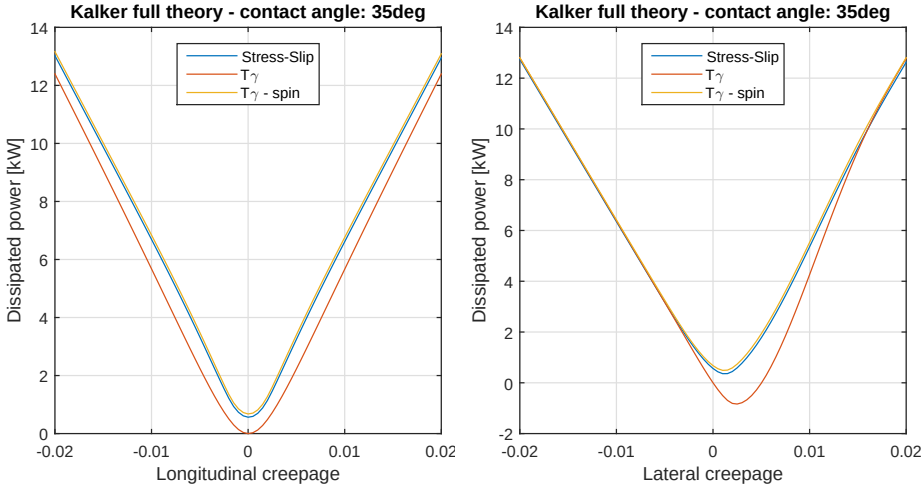


(a) (b)

Figure 5.2: The frictional power using the stress-slip method (Equation 5.3, stress and slip calculated using Kalker's full theory), T$\gamma$ method and T$\gamma$ method with spin (Equations 5.1 and 5.2, creep forces and moment calculated with Kalker's full theory), for a wheel-rail contact with a contact angle of 35°; (a) without lateral creepage and (b) without longitudinal creepage; with a friction coefficient of 0.4 and a train speed of 20 m/s.

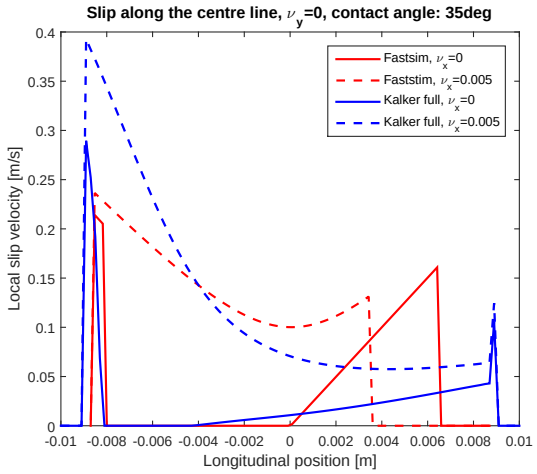


Figure 5.3: Comparison of the slip at the center line of the contact area; a pure spin case and a case with spin and a longitudinal creepage of 0.005, both cases with FastSim and Kalker's full theory. For Kalker full theory with $\nu_x = 0.005$, there is indeed no adhesion, so full slip. This was said nowhere said in the text.

within the contact patch. The slip calculated using Kalker's full theory is different: there is no adhesion zone at the trailing edge, in the pure spin case there is still an adhesion zone within the contact area, but it is smaller than with FastSim.

Figure 5.4 shows the magnitude of the tangential stress on the longitudinal line in the center of the contact area. In the slip zone the tangential stress is on the traction boundary, which is elliptical for FastSim an nearly elliptical for Kalker's full theory.

## 5.5. FRICTIONAL POWER THROUGH SIMULATIONS

### 5.5.1. THEORETICAL OPTIMIZATION OF THE FRICTION COEFFICIENT IN CASE OF TRACTION.

#### STRAIGHT TRACK

The methods described in the previous section can be used to search for the optimum friction coefficient and so to help choosing an adequate friction modifier. In cases where no acceleration or braking of the train is required the optimal friction coefficient is zero. When traction is required the friction coefficient needs to be large enough to allow the traction force to be transferred between the wheel and the rail. On the other hand the friction coefficient should not be too high because that increases the frictional energy. This optimization problem can be solved in a theoretical way for trains on straight track, as on a straight track we can assume the wheelset is in the center of the track, so that the contact angle between the wheel and the rail is known a priori. Moreover the yaw angle of the wheelset is negligible so that the lateral creepage is negligible. The longitudinal creepages are unknown; however, the longitudinal creep force is known, since that is the required traction force. FastSim always calculates the creep forces based on the creepages. So for this case, with two creepages (lateral and spin) and one creep force (longi-

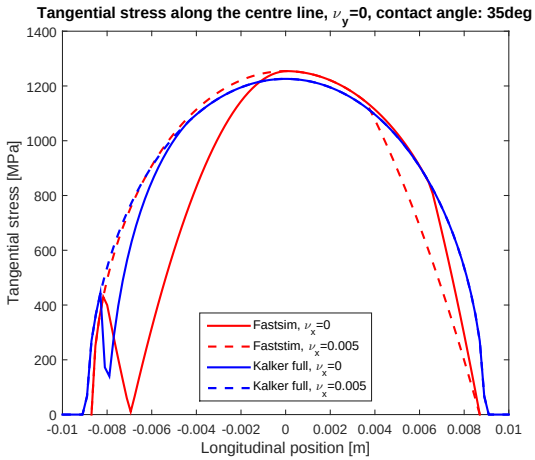


Figure 5.4: Comparison of the magnitudes of the tangential stress at the center line of the contact area; a pure spin case and a case with spin and a longitudinal creepage of 0.005, both cases with FastSim and Kalker's full theory.

tudinal) given, the contact method needs to be iterated (e.g. using the secant method) until the correct traction force is found.

Figure 5.5a shows the relative energy loss compared to the minimum energy loss, at the optimum friction coefficient, in percentage, as function of the friction coefficient, for a number of different traction forces with traction coefficient between 0.03 and 0.07. The traction coefficient is defined as the traction force on the wheel divided by the vertical wheel load.

While a friction coefficient equal to the traction coefficient is theoretically enough to transfer the traction force, friction coefficient close to the traction coefficient give rise to a higher energy dissipation. This is because traction forces close to the traction bound (determined by the friction coefficient) correspond to a high longitudinal creepage. A high friction coefficient gives high energy dissipation because the spin creepage now correspond to a higher creep moment. This increase is small when on a straight track where the spin creepage is small. Somewhere in between there is an optimum friction coefficient, high enough to transfer the traction force without to much longitudinal creepage, while still low enough to limit the creep moment. In Figure 5.5a it can be seen that with a traction coefficient of 0.03 the energy is minimal at a friction coefficient of 0.055 (80% higher), with a traction coefficient of 0.06 the optimum friction coefficient is 0.24 (4 times higher). With a traction coefficient higher than 0.06 the optimum friction coefficient swiftly increases: with a traction coefficient of 0.07 the energy dissipation is minimal at a friction coefficient of 0.81 (11.6 times higher), while higher traction coefficients (not shown in the Figure) have an optimum friction coefficient higher than what can be obtained in real live; sand can be used as a friction modifier to get closer to the optimum [7]. Overall the optimum friction coefficient is at least 80 % higher than the traction coefficient.

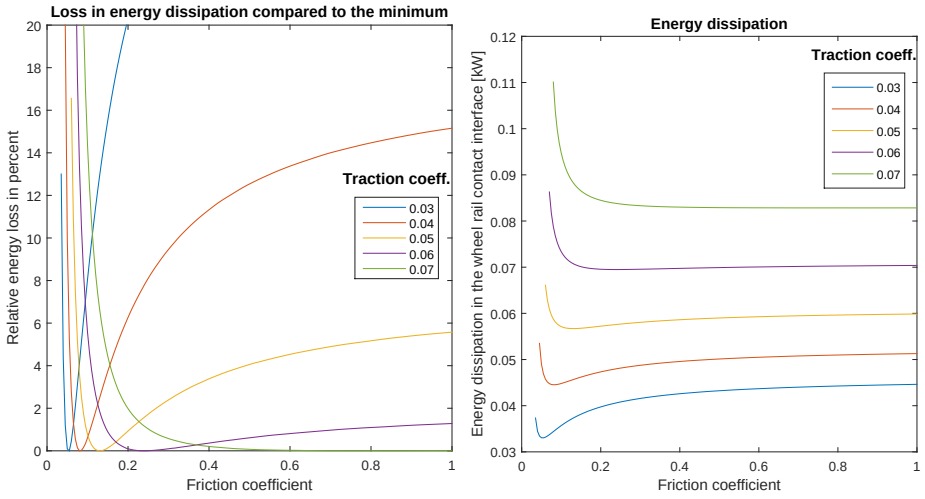


(a) (b)

Figure 5.5: The extra frictional energy dissipated in the wheel/rail contact compared to the minimum energy dissipation, corresponding with the optimum friction coefficient, in percent (a) and the absolute frictional power (b), for a wheel of a train on a straight track; with a friction coefficient of 0.4 and a train speed of 20 m/s.

It should be noted though, that for these small traction coefficients, the energy dissipation is quite small in absolute number (see Figure 5.5b), so that the benefits of controlling the friction are small when the required traction effort is not so high.

### CURVED TRACK

The theoretical friction coefficient optimization on curved track requires more assumptions than optimization on straight track. The wheelset position: the lateral displacement of the wheelset (so the contact angle) and the yaw angle of the wheelset (so the lateral creepage), are obtained from a dynamic simulation of a vehicle passing at 100 km/h through a 500 m radius track. It is then assumed that this wheelset position does not depend on the friction coefficient and that the traction force is evenly transmitted by the inner and the outer wheels. Both assumptions are, in fact, severely violated as will be explained in the next section, but they do allow to obtain a reasonable estimate of the energy dissipation as a function of the friction and traction coefficients, without the need for a large number of vehicle dynamic simulations. Figure 5.6 shows that the amount of energy that can be saved with the optimal choice of the friction coefficient is substantial and that even a small change in friction coefficient of 0.1 can result in additional energy losses of 20% (see Figure 5.6a). In Figure 5.6b it can be seen that a traction coefficient of 0.1 corresponds with an optimal coefficient of friction of 0.14, while a traction coefficient of 0.5 corresponds with an optimal friction coefficient of 0.81. It is therefore concluded that the optimum friction coefficient is 40 % to 60 % higher than the traction coefficient.

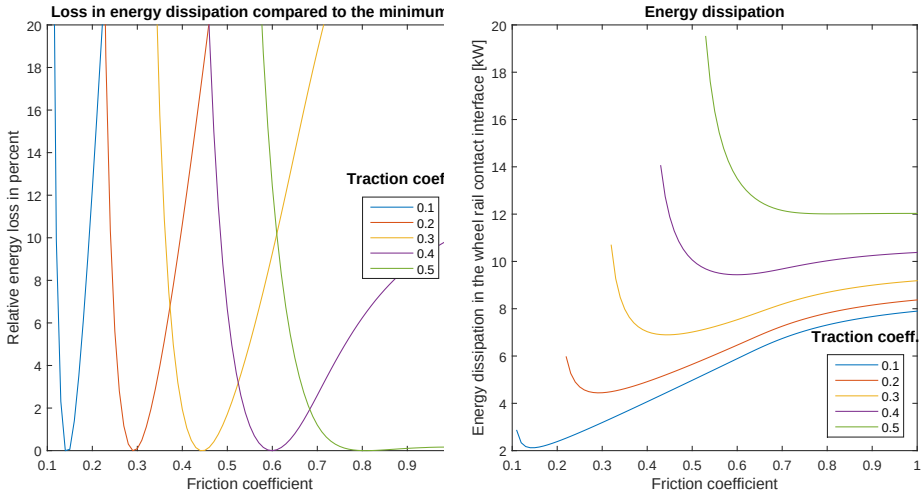


(a) (b)

Figure 5.6: The extra frictional energy dissipated in the wheel/rail contact compared to the energy dissipation with the optimum friction coefficient, in percent (a) and the absolute frictional power (b), for the outer wheel of a train negotiating a curve; with a friction coefficient of 0.4 and a train speed of 20 m/s.

### 5.5.2. FRICTIONAL POWER FROM VEHICLE DYNAMIC SIMULATIONS

*This section is a summary of the work done for the master thesis of Guillermo Idárraga Alarcón [1], published at the Contact mechanics conference 2015 [17]*

The main advantage of vehicle dynamic simulations is that there is no need to make assumptions regarding the wheelset position and the distribution of the traction force between the inner and the outer wheels, such as in Section 5.5.1. The disadvantage is that for each combination of traction and friction coefficient a new simulation and post-processing are required. Therefore, in this work we limit ourselves to a fixed traction coefficient of 0.2, defined as the traction force per wheelset divided by the axle load. This is the traction at which energy measurements were performed (see Section 5.6). Moreover, friction coefficients between 0.2 and 0.7 in steps of 0.05 were chosen.

Figure 5.7 shows the dissipated power per axle obtained from a vehicle simulation with the vehicle and track described in Section 5.2. In 5.7a it can be seen that the power dissipated on the first wheelset of the vehicle does not reach a local minimum, but is continuously increasing with the friction coefficient. It has to be noted here that the steps in friction coefficient were large so that a local minimum might be overlooked. In fact, there has to be a local minimum, as for even lower friction coefficients, the traction cannot be transferred and the wheel would fully slip (and the numerical simulation might diverge), which would definitely result in a very high energy dissipation. However, such a minimum would occur when the friction coefficient is close to the traction coefficient, whereas in the analytical analysis of the previous section we concluded that the friction coefficient is optimum at a value significantly higher than the traction coefficient. This difference might be due to the assumptions made in the theoretical analysis are violated:

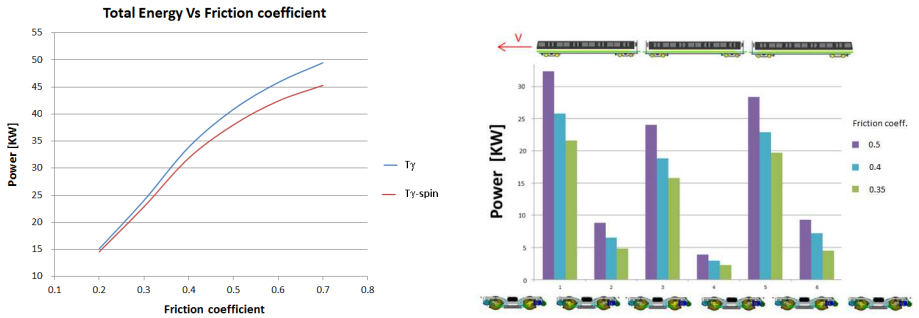


(a) (b)

Figure 5.7: The frictional power of the first wheelset of a vehicle curving with traction; calculated with FastSim with the $T\gamma$ method with and without spin (a) and the distribution of the frictional power over the wheelsets of the train.

- in Figure 5.8a it can be seen that the traction is not evenly distributed between the inner and the outer wheel and that this distribution changes with the friction coefficient. At high friction coefficients the outer wheel has high longitudinal creep force acting as traction, whereas the longitudinal creep force on the inner wheel acts in the other direction. This, to certain extend, resembles the case of no traction, where due to the difference in the rolling radius the left and the right wheel have opposing longitudinal creepages and creep forces. In the case of a low friction coefficient, the traction force on the outer wheel is limited, so that a part of the traction must also be transmitted by the inner wheel.
- in Figure 5.8b it can be seen that the lateral creepage is not constant with the friction coefficient: the higher the friction coefficient the lower the creepages. This is caused by a large difference between the inner and outer longitudinal creep force which creates a steering moment on the wheelset at high friction.

It can be concluded that for the theoretical analysis to be accurate enough it needs to be extended. Now it is essentially a longitudinal balance of the wheel, in future also the longitudinal balance of a wheelset so that the distribution of the traction between the wheels is accounted for. Further extensions could also include the lateral and yaw balance.

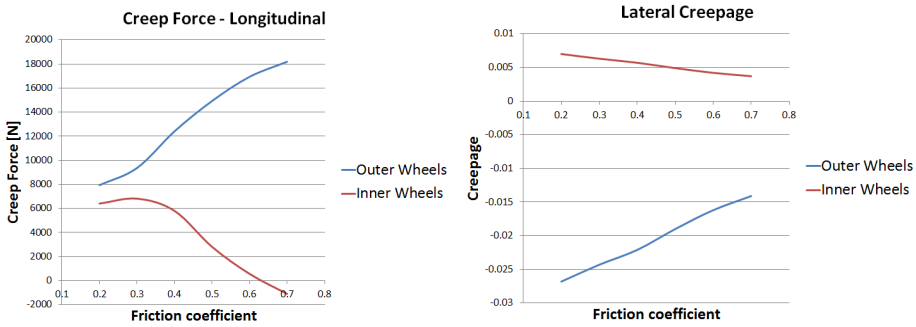


(a) (b)

Figure 5.8: The longitudinal creep force (a) and the lateral creepage (b) on the inner and outer wheel of the first wheelset of a vehicle curving with traction.

## 5.6. COMPARISON WITH VEHICLE DYNAMIC SIMULATIONS AND MEASUREMENTS

*This section is a summary of the work done for the master thesis of Guillermo Idárraga Alarcón [1], published at the Wear of Materials conference 2015 [18]*

It is not possible to directly measure the power consumed between the wheel and the rail, but it is possible to measure the electrical power transmitted to the train engine. This power is not only dissipated in the wheel/rail contact but also by:

1. Engine losses
2. Gear losses
3. Suspension loses
4. Aerodynamic loses: these can be roughly be estimated as

$$P_{\text{drag}} = \rho_{\text{air}} A_f C_d V^3 \tag{5.11}$$

where $\rho_{\text{air}}$ is the density of air, $A_f$ is the frontal area of the train, $C_d$ is a drag constant found in literature, and $V$ is the vehicle speed.

5. Potential power which can be estimated as

$$P_{\text{pot}} = mgV\frac{\partial h}{\partial x} \tag{5.12}$$

where $m$ is the vehicle mass, $g$ the gravity constant and $\frac{\partial h}{\partial x}$ the slope of the track

6. The kinetic power which can be estimated as

$$P_{\text{kin}} = mVa \tag{5.13}$$

where $a$ is the vehicle acceleration.

When we assume that the first three powers are small and if we subtract the last three from the measured engine power, we can assume that the resulting power is dominated by the frictional power. Moreover, this approach allows to compare the results of different measurements at different vehicle speed. Note that the formulas are rough approximations so that only runs with a fairly similar velocity profile can be compared.

From the measured and simulated power listed in Table 5.1, it can be seen that the trend from the simulations and the measurements correspond: lower friction coefficient means lower power. It was, however, not possible to quantitatively reproduce the power levels. This could be related to either the modeling in the simulations (e.g. the wheel and rail profiles used for the simulation might differ from those of the measured train and wheel) or to inaccuracies in the measurements.

Table 5.1: Measured and simulated energy consumption

| Friction coefficient | Measured power [kW] | reduction [%] | Simulated power [kW] | reduction [%] |
|---|---|---|---|---|
| 0.5 (dry) | 118 | - | 106 | - |
| 0.4 (post lubrication) | 108 | 9.4 | 84.3 | 21 |
| 0.35 (lubricated) | 99.7 | 15 | 68.7 | 36 |

## 5.7. CONCLUSIONS

Several methods have been described to calculate the frictional energy. These methods are based on the creepages and creep forces ($T\gamma$) at a reference point, with or without the spin moment being considered, or based on integral of the product of the local slip and tangential stress. The methods have been applied using FastSim or Kalker's full theory. It is concluded that for Kalker's full theory the $T\gamma$ with spin and the stress-slip approach result in the almost same frictional power. Another conclusion is that one has to be careful with the results from FastSim for cases where the spin creepage is dominant.

These methods have been applied in a theoretical analysis based on the longitudinal force balance of one wheel. For a straight track this theoretical analysis can be used to find the friction coefficient at which the frictional power is the smallest, and replace vehicle dynamic simulations for that purpose. It was concluded that both in curves and on straight track the optimal friction coefficient is significantly higher than the traction coefficient. However, in curves this approach cannot be used as some of the assumptions made were found to be in disagreement with vehicle dynamic simulations.

Finally, it is possible to compare measurements from the electric power consumption of the engines with simulations of the frictional power. The match between these has shown the same trend with respect to the frictional power as function of the friction coefficient, but a quantitative comparison is difficult due to uncertainties in both inputs to the vehicle model and the measurements.



## REFERENCES

[1] G. I. Alarcón, *The influence of rail lubrication on wear and energy dissipation in wheel/rail contact*, Master's thesis, National University of Colombia (2015).

[2] J. J. Kalker, *A fast algorithm for the simplified theory of rolling contact,* Vehicle System Dynamics **11**, 1–13 (1982).

[3] J. J. Kalker, *Three Dimensional Elastic Bodies in Rolling Contact* (Kluwer Academic Publishers, 1990).

[4] Y.-S. Ham, D.-H. Lee, S.-J. Kwon, W.-H. You, and T.-Y. Oh, *Continuous measurement of interaction forces between wheel and rail,* International Journal of Precision Engineering and Manufacturing **10**, 35–39 (2009).

[5] E. Kasa and J. Nielsen, *Dynamic interaction between train and railway turnout: full-scale field test and validation of simulation models,* Vehicle System Dynamics **46**, 521–534 (2008).

[6] M. Ishida and N. Abe, *Experimental study on rolling contact fatigue from the aspect of residual stress,* Wear **191**, 65–71 (1996).

[7] E. Gallardo-Hernandez and R. Lewis, *Twin disc assessment of wheel/rail adhesion,* Wear **265**, 1309–1316 (2008).

[8] A. Matsumoto, Y. Sato, H. Ohno, M. Shimizu, J. Kurihara, T. Saitou, Y. Michitsuji, R. Matsui, M. Tanimoto, and M. Mizuno, *Actual states of wheel/rail contact forces and friction on sharp curves – continuous monitoring from in-service trains and numerical simulations,* Wear **314**, 189–197 (2014).

[9] P. Lukaszewicz, *Running resistance - results and analysis of full-scale tests with passenger and freight trains in sweden,* Proceedings of the Institution of Mechanical Engineers Part F Journal of Rail and Rapid Transit **222**, 183–192 (2007).

[10] P. Lukaszewicz, *A simple method to determine train running resistance from full-scale measurements,* Proceedings of the Institution of Mechanical Engineers Part F Journal of Rail and Rapid Transit **222**, 331–337 (2007).

[11] J. VanderMarel, D. T. Eadie, K. D. Oldknow, and S. Iwnicki, *A predictive model of energy savings from top of rail friction control,* Wear **314**, 155 (2014).

[12] R. Lewis and U. Olofsson, *Mapping rail wear regimes and transitions,* Wear **257**, 721–729 (2004).

[13] F. Braghin, R. Lewis, R. Dwyer-Joyce, and S. Bruni, *A mathematical model to predict railway wheel profile evolution due to wear,* Wear **261**, 1253–1264 (2006).

[14] S. Iwnicki, *Handbook of railway vehicle dynamics* (Taylor and Francis, 2006).

[15] J. J. Kalker, *Rolling contact phenomena—linear elasticity,* Proceedings of the CISM International Centre for Mechanical Sciences **411**, 1–183 (2001).

[16] A. Alonso, J. G. Giménez, and L. M. Martín, *Spin moment calculation and its importance in railway dynamics,* Tribology International **91**, 755–768 (2009).

[17] G. I. Alarcón, N. Burgelman, J. M. Meza, A. Toro, and Z. Li, *The influence of friction coefficient and wheel/rail profiles on energy disspation in the wheel/rail contact,* Proceedings of the 10th Contact Mechanics conference, Colorado Springs, USA (2015).

[18] G. I. Alarcón, N. Burgelman, J. M. Meza, A. Toro, and Z. Li, *The influence of rail lubrication on the energy dissipation in the wheel/rail contact: a comparison of simulation results with field measurements,* Wear **330**, 533–539 (2015).

# 6

# Fast Estimation of the Derailment Risk of a Braking Train in Curves and Turnouts

*When a train runs through a turnout or a sharp curve, very high lateral forces or high impact forces occur between the wheels and rails. The lateral forces increase when the couplers between the wagons are loaded in compression, i.e., a rear locomotive pushing a train or a front locomotive braking a train. This study quantifies these effects for a train that begins braking when steadily curving and for a train that brakes upon entering a turnout. Our approach allows distinguishing between the effects of braking and the transient effects of entering the turnout. The dynamic derailment quotient is mapped as a function of the vehicle speed and the braking effort. Such a map should be useful when defining the emergency braking protocols for long trains. Then the dynamic derailment coefficient obtained from the dynamic simulations are compared to results from quasi statics. This allows to determine a dynamic multiplication coefficient that can be used on the quasi static derailment coefficient to obtain a first estimate of the dynamic derailment coefficient. Furthermore, the effect of the coupler design on the lateral forces is investigated.*

This chapter has been accepted for publication in the International Journal of Heavy Vehicle Systems.

## 6.1. INTRODUCTION

### 6.1.1. BACKGROUND ON LONGITUDINAL-LATERAL TRAIN DYNAMICS.

The effects of braking and traction on long trains have often been studied from the longitudinal dynamics point of view [1]. The longitudinal problem can be solved with just one degree of freedom per vehicle, thereby limiting the calculation effort even for long trains. Many authors have published longitudinal coupler models that include nonlinear springs, slack and/or friction [2–6]. Others have studied the combination of the longitudinal and vertical problems [7] including the wheel unloading due to bogie or carbody pitch and bounce. The pitch and bounce modes are excited because the centers of gravity of the vehicles are often higher than the couplers, particularly when the wagons are loaded [1]. The lateral forces in long trains were first studied by El-Sibaie [8], who conducted an experimental analysis of the problem. The lateral coupler forces on one test wagon were controlled by actuators on the adjacent vehicle; then, the train ran through a curve, while the forces on the wheels were measured using an instrumented wheelset. This approach allows monitoring of the relationship between vehicle speed and coupler force, and the derailment quotient. Cole et al. [9] (amongst others) combined simulations of longitudinal train dynamics with quasi-statics to obtain the lateral forces; the coupler angles were calculated using an approach suggested by [10]. Xu et al. [11, 12] combined a detailed model of three vehicles with a simple model (1 degree of freedom) for most vehicles; this approach reduced the total degrees of freedom and so the calculation effort. The vehicles modeled in detail were the locomotives and the adjacent wagons because it is between them that the highest coupler forces occur. They concluded that the rotation limit for the coupler best be set to 4°.

This paper features simulations of a train consisting of a locomotive followed by seven wagons, each of which is modeled with 42 degrees of freedom, thus including all lateral, vertical and longitudinal motions and rotations. The model is of a passenger train; therefore the secondary suspension is soft compared to freight vehicles, and the results obtained are useful for operators of passenger trains. This work could be particularly applicable in designing pulling/pushing policies for passenger trains in shunting yards. Shunting yards have many turnouts, that often receive insufficient maintenance; therefore most derailments happen there. Although the paper does not address long freight trains, our methodology and estimation/mapping could be useful for heavy-haul operators.



### 6.1.2. BACKGROUND ON VEHICLE-TURNOUT INTERACTION

The interactions between trains and tracks are most violent at turnouts due to the complex geometry and structure. Improperly designed or maintained turnouts can cause discomfort to passengers, damage to cargo, or even a derailment. Maintenance and repair of turnouts are a major cost driver for many infrastructure managers.

Lateral train-track interaction force is high in turnouts due to their small curve radii, and it might be increased further by the compressive forces in the couplers of a train due to braking or traction. A high lateral force may lead to deformation of the control mechanism of a switch, and a lateral shift of the entire track. A deformed stretch bar of the control mechanism may lead to incorrect positioning of switch blades. All of these may

result in malfunctioning of turnouts, causing wheel climb and subsequent derailment. Wear and head checking are other common consequences of high wheel-rail contact forces.

There are many aspects to the modeling of vehicle-turnout interactions, and different authors have focused on different aspects. Menssen and Kik [13] were among the first to address the numerical simulation of a rail vehicle passing through a turnout. Some of the most recent work in vehicle-turnout interaction has been performed by Kassa and Nielsen [14] and Alfi and Bruni [15]. They focused on the detailed modeling of a single vehicle passing a turnout, with flexibilities to account for high frequency phenomena. Other authors have focused on the wheel-rail contact in turnouts, which is complex due to the profiles of the switch blade and the crossing. Wiest et al. [16] and Shu et al. [17] focused on the normal contact problem, while Burgelman et al. [18] considered the tangential problem. To the authors' knowledge, all the models in the literature to date have included a single vehicle coasting through a turnout. Work on train-turnout interaction rather than vehicle-turnout interaction appears lacking, particularly analysis of the influence of the coupler forces on the lateral train dynamics and on the derailment quotient.

The goals of this paper are to establish a simple method to quickly assess the derailment risk by estimating the derailment quotient, and to validate this method using vehicle dynamic simulations with a detailed model of a locomotive followed by seven wagons. To this end, quasi-statics is used to obtain a first guess of the derailment quotient. Because quasi-statics does not require any simulation, this can be performed easily for any combination of curve radius, braking force, number of vehicles, etc. Then, simulations are performed to calculate the maximum derailment quotient of a locomotive followed by seven wagons on a curve or a turnout. This dynamic derailment quotient is used to define a dynamic multiplication coefficient to be used with the static derailment quotient. Mapping the derailment quotient as function of speed and braking effort can provide a tool to train operators formulate upon their braking protocols. Assessing the derailment risk without long and complex vehicle simulations might be especially interesting when a fast estimate is required for a train configuration different from those in typical daily operations.

Relating the results from quasi-static calculation with measured or simulated results in order to obtain a fast way of estimating the dynamic forces has been investigated before. The dynamic wheel-rail forces on curves and straight track including track irregularities have been mapped in [19] based on results from [20] and [21]. Grassie [22] published a relation between the quasi-static load and the dynamic vertical track forces as a transfer function which is basically a wavelength-depended multiplication factor. Dietrich et al. [23] have investigated the effect of cross wind; they concluded that the allowable cross wind was just 3 m/s lower when calculated with quasi-statics compared to calculated using a vehicle dynamic simulation.

The assumptions made in the quasi-static analysis are violated in reality. But the results will still be valid, as long as it is possible to define a dynamic multiplication coefficient which allows obtaining a reasonable estimate of the dynamic force in a usable range of vehicle speeds and traction/braking efforts. This means that all contributions to the dynamic lateral force that scale approximately linearly with the traction/braking

effort and quadratically with the vehicle speed are accounted for.

## 6.2. THE MODEL

### 6.2.1. TRACK MODEL

Two models are used: one for a curved track with a transition and one for a turnout without a transition. The curve is modelled with the same radius as the turnout: 260 m and without cant. This way we can analyse separately the transient responses from braking and from entering the turnout. In reality, a curve will; always have a certain cant except for some trams that share the tramway with road vehicles. The diverging route was modelled, meaning that there is no transition curve between the straight track and the curvature of the turnout. The rail profiles used for the blade of the turnout were obtained through measurements on a 1:9 turnout, which had been in regular service for some years [24]. This turnout was described as heavily worn and was on the limit of the safety criteria for profile change.

### 6.2.2. VEHICLE MODEL

The vehicles modeled are those of the VIRM trains of the Dutch Railways. Each vehicle has 42 degrees of freedom (dof): 6 dof for each of the wheelsets, the bogie frames and the carbody. All major nonlinearities in the primary and secondary suspension are considered, including the friction dampers, the bump stops and the airsprings. The model has been validated by comparing the hunting wavelength obtained from simulations with wavelengths observed from wear patterns on the rails [25]. The wheel-rail contact was treated using the multi-Hertzian approach for the normal contact problem and the FASTSIM algorithm for the tangential contact problem.

### 6.2.3. TRAIN CONFIGURATION

The configuration of the train is shown in Figure 6.1. The passage of a locomotive followed by 7 identical wagons is simulated through a curve and a turnout. A braking force is applied to the wheels of the locomotive when the first wagon enters the turnout, which is implemented in the model as an actuator applying a moment between the axle boxes and the wheelsets. The wheelsets of the wagons do not apply traction or braking. The train is modelled with of 336 degrees of freedom (8x42). For the simulations in this chapter, with a simulation times from 5 s to 10 s, the computation time was found to be around 10 min on a common computer.



### 6.2.4. COUPLING OF THE COACHES

The VIRM vehicles are coupled with Scharfenberg couplers. This type of coupler does not transfer any yaw moment when coupler angles are small. It is modeled as one spring in parallel with a damper, positioned in the center-line of the vehicles; the force-displacement curves of the non-linear springs have been obtained from [2]. Buffers and chain couplers, used mostly in freight vehicles, consist of a center chain that transfers the pulling forces and one buffer on each side, transferring pushing forces. The buffers and chain coupler are modeled as two spring/damper pairs, one on each side. This type of coupler transfers a yaw moment between the carbodies.

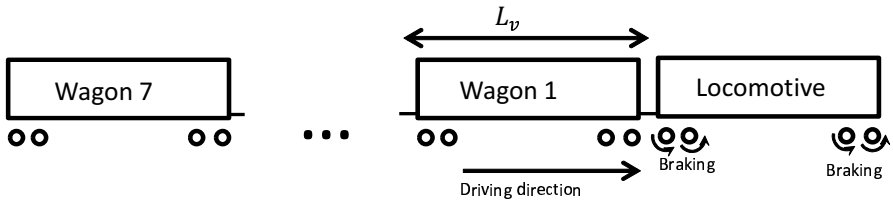


Figure 6.1: Overview of the train and the applied traction and braking.

### 6.2.5. QUASI-STATIC DERAILMENT QUOTIENT

If all energy dissipation from wheel-rail contact, the suspension elements and air resistance is neglected, the effect of braking is to consume the kinetic energy of the train and dissipate it in the brakes. Because all the vehicles are subject to the same deceleration, the force in each coupler is proportional to the total mass of the vehicles behind it. Therefore, the coupler forces will be largest in the coupling between the locomotive and the first wagon:

$$F_{c1} = \frac{7m_{\text{wag}}}{7m_{\text{wag}} + m_{\text{loc}}} F_{\text{braking}} \tag{6.1}$$

with

$$F_{\text{braking}} = \mu\, g\, m_{\text{loc}} \tag{6.2}$$

where $\mu$ is the braking coefficient defined as the braking force per wheelset divided by the axle load, $g$ is the gravity constant, $m_{\text{loc}}$ is the mass of the locomotive (here 88 000 kg), $m_{\text{wag}}$ is the mass of a wagon (here 80 000 kg), $F_{\text{braking}}$ is the total braking force applied by the locomotive, and $F_{c1}$ is the force in the first coupler.

Because the coupling does not transfer a yaw moment, the resultant force of the coupler on a wagon is always in the direction of the coupler. Define $\phi$ as the coupler angle, i.e., the angle between the coupler and the vehicle (see Section 6.2.6); the lateral component of the coupler force becomes:

$$F_{\text{lat},c1} = F_{c1} \sin\phi \tag{6.3}$$

This lateral force is distributed among the wheelsets of the vehicle. Assuming that these forces are distributed uniformly by the wheelsets of the bogies adjacent to the coupler (because the other bogie must carry the lateral force introduced by the other coupler) and assuming that the lateral load due to the centripetal force is uniformly distributed, the lateral force, $Y$, per wheelset on the wheelsets of the leading bogie of the first wagon becomes:

$$Y = \frac{F_{c1} \sin\phi}{2} + \frac{m_{\text{wag}}}{4}\left(\frac{V^2}{R} - g\epsilon\right) \tag{6.4}$$

where $V$ is the velocity of the train, $\epsilon$ is the cant angle, and $R$ is the curve radius. The derailment quotient is the ratio of the lateral force to the vertical force, $Q$, of the outer wheel in the turnout. If we assume that the lateral force is transferred to the track by the outer wheel and neglect the lateral force on the inner wheel, the lateral force on the

outer wheel is $Y$. The vertical force on the outer wheel can be estimated by quasi-statics as follows:

$$Q = \frac{m_{\text{wag}}}{8} g + \frac{m_{\text{wag}}}{4} \left( \frac{V^2}{R} - g\epsilon \right) \frac{h}{l} \tag{6.5}$$

where $h$ is the height of the center of gravity of the vehicle above the rail top, and $l$ is the track width.

### 6.2.6. COUPLER ANGLE CALCULATION

The magnitude of the coupler angle affects the lateral component of the coupler forces. Simson [10] has proposed an approach to calculate the coupler angle that can be extended for a transition curve or a turnout. If we ignore the displacements in the bogie suspension and the stiffness of the coupler, then the bogie pivot center is located above the center of the track, and the coupler has a fixed length. Hence the coupler angle becomes independent of forces and velocities and depends only on geometric variables: dimensions of the vehicles (the distance between the bogies, the distance between the bogie and the coupler pivot and the length of the coupler itself) and the track curvature. In the case of a curve transition or a turnout, the local track curvature needs to be known at each point of the track where the two vehicles adjacent to the coupler are. The general case is shown in Figure 6.2

$$L = B_i + B_{i+1} + D \tag{6.6}$$

where $L$ is the distance between the centers of the two bogies of adjacent vehicles (assuming small angles), $B_i$ and $B_{i+1}$ are the overhangs, i.e., the distances between the centers of the bogies and the pivots of the coupler link, and $D$ is the distance between the two coupler pivots.

The angle between the carbodies of the two vehicles, $\theta$, can be calculated as follows:

$$\theta = \alpha + \beta + 2\gamma \tag{6.7}$$

where $\alpha$ and $\beta$ are the angles between each vehicle and the tangent to the track in the bogie pivot adjacent to the coupler (i.e., points $r_i$ and $f_{i+1}$, see Figure 6.2) and $\gamma$ is the angle between the two tangents to the track in $r_i$ and $f_{i+1}$. These angles can be calculated using integrals along the track (d$s$):

$$\alpha = \frac{1}{2A_i} \int_{r_i}^{f_i} \int_{r_i}^{s} \frac{1}{R_{\text{local}}} \, \mathrm{d}s \, \mathrm{d}s \tag{6.8}$$

$$\beta = \frac{1}{2A_{i+1}} \int_{f_{i+1}}^{r_{i+1}} \int_{f_{i+1}}^{s} \frac{1}{R_{\text{local}}} \, \mathrm{d}s \, \mathrm{d}s \tag{6.9}$$

$$\gamma = \frac{1}{2} \int_{f_{i+1}}^{r_i} \frac{1}{R_{\text{local}}} \, \mathrm{d}s \tag{6.10}$$

where $A_i$ is half the distance between the two bogie pivots of vehicle $i$.

If the curve radius is piecewise constant between the bogie pivots then $\alpha$, $\beta$ and $\gamma$ can be calculated as:

$$\alpha = \frac{A_i}{R_i}, \qquad \beta = \frac{A_{i+1}}{R_{i+1}}, \qquad \gamma = \frac{L}{2R_l} \tag{6.11}$$

where $R_i$ is the curve radius between $f_i$ and $r_i$, and $R_l$ is the radius between $f_{i+1}$ and $r_i$.

The coupler angles (see [10]) are the angles between the coupler and vehicle $i$, $\phi_i$, or vehicle $i+1$, $\phi_{i+1}$:

$$\phi_i = \frac{L(\gamma+\alpha) - B_{i+1}\theta}{D}, \qquad \phi_{i+1} = \frac{L(\gamma+\beta) - B_i\theta}{D} \tag{6.12}$$

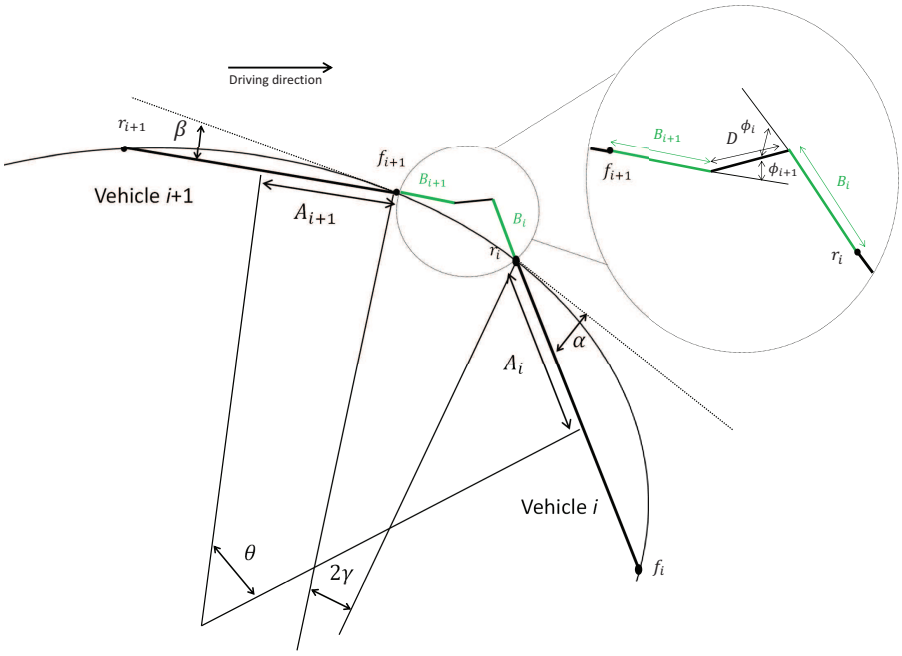


Figure 6.2: The coupler angle in a curve with varying radius.

### 6.2.7. COUPLER ANGLE IN A CURVE AND UPON ENTERING THE TURNOUT

For a curve with constant radius $R$ and two geometrically identical vehicles, the angle a coupler makes with the centerlines of the wagons to which it is attached is: $\phi = \frac{L_v}{2R}$, where $L_v$ is the length of one wagon including the couplers (see Figure 6.1). This equation is a simplification of equation (6.12); the two coupler angles are identical and depends only on the total vehicle length and the curve radius. For the vehicle in this study and a 260 m curve, the resulting coupler angle is 2.75°. Connecting two vehicles with a different geometry would result in a larger coupler angle.

A turnout consists of a straight part followed, without transition, by a curve with a constant radius. Therefore it is not necessary to evaluate the integrals of equations (6.8-6.10); equation 6.11 can be used instead. When a train passes a 1:9 turnout, the largest

coupler angle occurs upon entering the turnout when the first vehicle is in the turnout ($R_1 = 260\,\text{m}$) and the two bogies of the second vehicle are still on the tangent track ($R_2 = \infty$), while the overhang of the second vehicle is already in the turnout ($R_l = 260\,\text{m}$); this situation is drawn in Figure 6.3. The resulting maximum coupler angle for the case study of this paper is 7.14° between the locomotive and the coupler; the angle between the coupler and the first wagon is smaller and acts in the other direction; i.e., the resulting lateral force from braking pushes the wagon inwards. Due to symmetry, a reverse situation will exist upon leaving the turnout, but the lateral force will be smaller because the quasi-static lateral force on the locomotive will be zero. Therefore this study focuses only on entering of turnout.

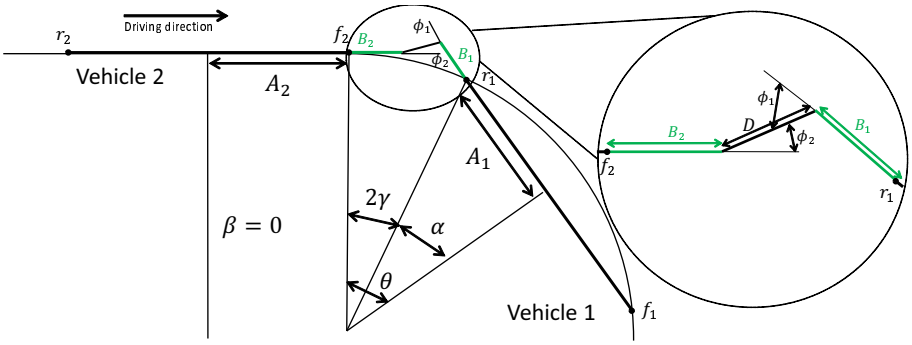


Figure 6.3: The coupler angle with vehicle 1 in the turnout and vehicle 2 with the leading bogie just at the beginning of the turnout.

## 6.3. Results

### 6.3.1. Quasi-statics

#### Curving

The derailment quotients calculated from equations (6.4) and (6.5) are plotted in Figure 6.4a as functions of the train velocity and the braking coefficient applied by the locomotive. The influence of the train velocity is larger than that of the braking; however the latter is not insignificant. A train entering a turnout at 40 km/h, the maximum allowed speed in a 1:9 turnout, with the highest possible braking of the locomotive (i.e. braking coefficient = 0.6) creates a higher derailment quotient on the wheel than a train coasting (braking coefficient = 0) through the same turnout at 55 km/h.

#### Turnout

In a turnout the coupler angle is much larger; therefore, compared to a curve the influence of the braking coefficient on the derailment quotient is also much larger. The derailment quotient is shown in Figure 6.5a. The quasi-static derailment quotient of a train entering a turnout at 40 km/h, the maximum allowed speed in such a turnout, surpasses the derailment quotient of a train running through the turnout at 80 km/h with a moderate braking coefficient of 0.2.

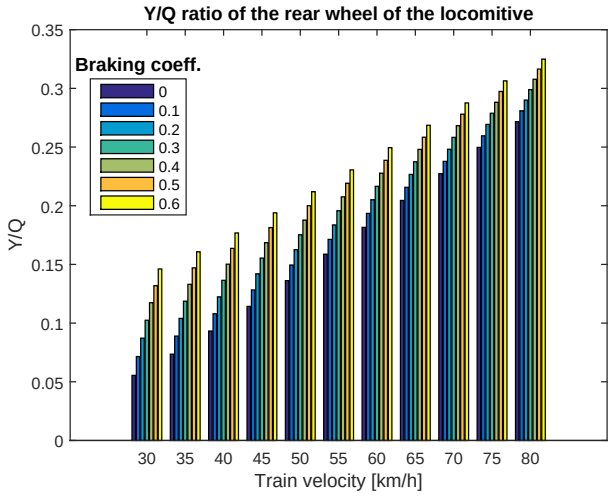


(a)

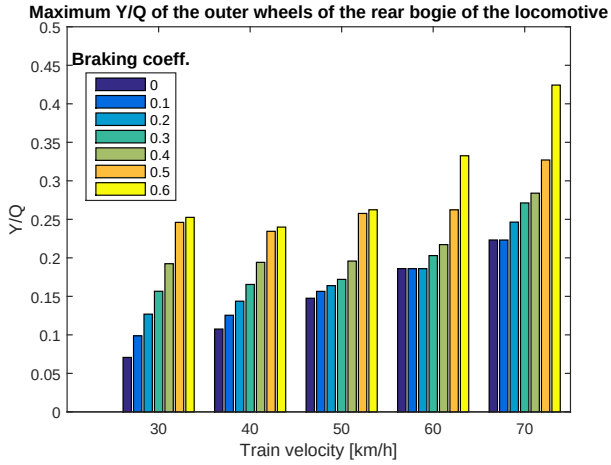


(b)

Figure 6.4: The maximum derailment quotient of the outer wheels of the rear bogie of the locomotive in a curve, (a) calculated with equations (6.4) and (6.5), (b) obtained from dynamic simulations. The braking coefficient, ranges from 0 (no braking) to 0.6 (only achievable on dry track/perfect conditions). The velocity is swept from 30 km/h to 80 km/h; 40 km/h is the maximum speed allowed in a 1:9 turnout.



### 6.3.2. THE VEHICLE EIGENMODES

To understand the dynamic behavior of the train, a rigid body modal analysis was performed for a train with Scharfenberg couplers and a train with buffer-and-chain couplers (see Table 6.1). Most of the eigenmodes are identical except for the carbody sway, roll and yaw modes, where the yaw moment between the carbodies transferred by the couplers plays a role. Because of the yaw stiffness between the carbodies, the motions

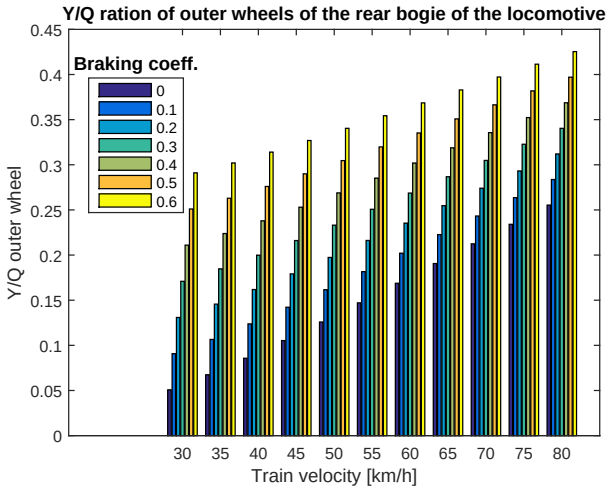


(a)

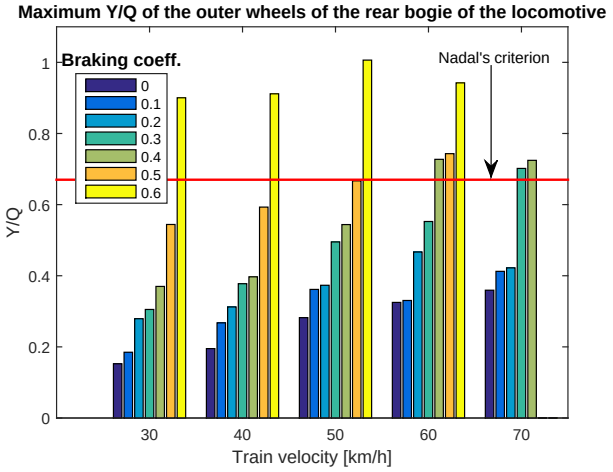


(b)

Figure 6.5: The maximum derailment quotient of the outer wheels of the rear bogie of the locomotive in a 1:9 turnout, (a) calculated with equations (6.4), (6.5) and (6.12), (b) obtained from dynamic simulations. The braking coefficient ranges from 0 (no braking) to 0.6 (only achievable on dry track/perfect conditions). The velocity is swept from 30 km/h to 80 km/h; 40 km/h is the maximum allowed speed in a 1:9 turnout. The horizontal line is the maximum derailment quotient according to Nadal (calculated with flange angle 65°, and friction coefficient 0.6.)

of the vehicles influence one another; therefore there is a range of frequencies for the carbody yaw and sway modes rather than one specific frequency. This range represents a number of closely related eigenmodes in which the adjacent vehicles move in phase or in anti-phase.

In the longitudinal carbody modes the train acts as a number of masses in series connected with springs. One can see this eigenmode as a standing longitudinal wave in the train. In the case of a discrete number of masses in series, the eigenfrequencies are close to multiples of the first standing wave. Unlike the other eigenmodes, which depend mostly on the vehicle properties, the longitudinal eigenmodes strongly depend on the train configuration, i.e., the number of vehicles; when the train is longer the eigenfrequency of the first longitudinal carbody mode will decrease in proportion to the number of vehicles.

Table 6.1: The eigenmodes and eigenfrequencies of the whole train model.

| Eigenmode | Frequency in Hz | |
|---|---|---|
| | Scharfenberg | buffer-and-chain |
| Carbody sway of the wagons | 0.42 | 0.36-0.37 |
| Carbody sway of the locomotive | 0.48 | 0.37 |
| Carbody roll of the wagons | 0.67-0.68 | 0.62 |
| Carbody bounce of the wagons | 0.79 | 0.79 |
| Carbody bounce of the locomotive | 0.84 | 0.84 |
| Carbody yaw of the wagons | 0.84 | 0.84-0.89 |
| Carbody pitch of the wagons | 1.1-1.2 | 1.1-1.2 |
| Carbody pitch of the locomotive | 1.2 | 1.2 |
| Carbody longitudinal through the couplers | 2.4-4.7-6.8-8.7 | 2.4-4.7-6.8-8.7 |
| Bogie pitch of the wagons | 5.9 | 5.9 |
| Bogie roll of the wagons | 9.3 | 9.3 |
| Bogie higher modes | >10 | >10 |

### 6.3.3. TRAIN SIMULATIONS

The quasi-statics do not include some 'quasi statics' effects such as wheel unloading due to static carbody pitch. The static carbody pitch originates from the coupler forces that are not the same height above the rail as the center of mass of the vehicles; moreover, the locomotive static carbody pitch also originates from the braking forces on the wheels. To quantify the effects of the quasi-static assumption, a number of dynamic simulations were performed for two cases: first, a train steadily curving and then suddenly applying a braking force (Section 6.3.3.1), and second, a train braking upon entering a turnout (Section 6.3.3.2). Each case was simulated with 7 different coefficients of braking and 5 different initial train speeds.

The cases of a curve and a turnout allow studying the different dynamic effects, which are composed of the eigenmodes of the train. These dynamic effects can be split into two parts: first the dynamic effect due to application of braking, which changes the longitudinal acceleration of the vehicles, and second, the dynamic effect due to the curve transition, which changes the lateral acceleration of the vehicles.

#### DERAILMENT QUOTIENT WHILE CURVING

To study the influence of the dynamics in a turnout we have simulated the case of a train running at 40 km/h through a 260 m curve (see Figure 6.6). After the transient phe-

nomena from entering the curve have died out, braking is applied to the wheels of the locomotive. Prior to braking, the wheels of the leading bogie of the first wagon carry the lateral load due to the centripetal force. The average of the force can be calculated from equation (6.4), but it is non-uniformly distributed in that the outer front wheel carries a much higher load than the outer rear wheel. The average lateral force from the simulation is 9.5 kN, as predicted by quasi-statics. This quasi-static lateral force corresponds to a quasi-static derailment quotient of 0.05 (see Figure 6.4a), while the derailment quotient from the simulation is 0.11 (see Figure 6.4b). When the braking takes effect, the lateral force increases on both wheels but more on the rear wheel. Because the vehicle loses speed, the centripetal force decreases, and so does the lateral force on the wheels. The maximum simulated lateral force is 29.5 kN for the train with buffer-and-chain couplers and 27.5 kN with Scharfenberg couplers, whereas the quasi-static approach predicted 16.7 kN. This difference from the quasi-static approach is partly because the front wheel transfers most of the load and partly due to dynamic effects. The difference in the lateral force between the two types of couplers is small, approximately 7.3%. The maximum derailment quotient in the case of braking is 0.09 from the quasi-statics and 0.195 from the dynamic simulations. From Figure 6.7a it can be concluded that the simulated dynamic derailment quotient is not higher than 2 times the quasi-static derailment quotient. This dynamic multiplication factor may be used to make a conservative estimate of the derailment quotient based on quasi-statics.

As the vehicles steadily curve the eigenmode that will be most excited, when braking starts is the longitudinal vibration of the carbodies. One can observe this eigenmode as a standing longitudinal wave in the train. The oscillation in Figure 6.6b has resonance frequencies at approximately 2.4 Hz, 4.7 Hz, 6.8 Hz and 8.7 Hz, which is close to the longitudinal eigenmodes (see Table 6.1). A second eigenmode that is excited is the vehicles' pitch mode. The eigenmode analysis predicts its eigenfrequency at 1.1 Hz, and indeed, in the simulation an oscillation at 1.1 Hz can be observed.

### Derailment quotient when entering a turnout

When a train brakes upon entering the turnout, lateral (roll, yaw, sway) as well as longitudinal modes are excited in the coupling. The eigenfrequencies corresponding to these modes are close to one another (see Table 6.1), therefore it is not possible to identify these eigenmodes in the frequency domain as could be done in the case of braking while steadily curving.



Figure 6.8 shows the lateral force on the outer wheels of the leading bogie of the locomotive when entering a 1:9 turnout at 40 km/h. When the wheels enter the turnout the contact on the outer wheel changes from one point contact to two-point contact: one at the wheel flange and one at the wheel tread. When the wheel flange makes contact with the rail there is an impact force. This impact force is important when considering wheel-rail wear or impact noise. However, if the goal is to assess the derailment risk, peak forces lasting less than 50 ms can be ignored [1]. This 50 ms threshold was used to create Figure 6.5b.

The derailment quotients are compared with a threshold as defined by Nadal's criterion (horizontal line in Figure 6.5b). In this case the criterion was calculated using a friction coefficient of 0.6, corresponding to dry conditions and a wheel flange angle of

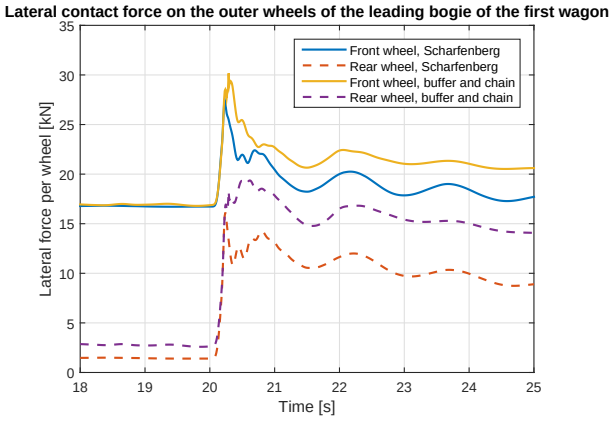


(a)

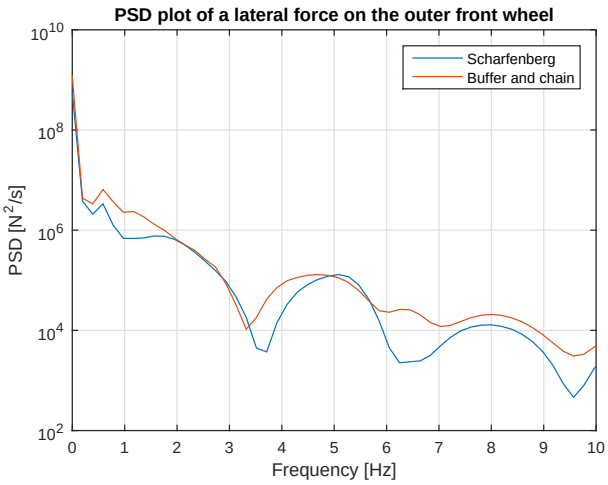


(b)

Figure 6.6: The lateral force on the outer wheels of the leading bogie of the first wagon in curve at 40 km/h. The vehicle is dynamically simulated steadily curving in a 260 m radius curve. At time 20 s the locomotive starts braking with a braking coefficient of 0.4.



65°, corresponding to a worn wheel profile. At 70 km/h not all simulations converged due to the high lateral forces so that derailment occurred. Several assumptions made in vehicle simulations do not hold at these high derailment quotients, especially the assumptions made for the wheel-rail contact calculations, such as planar contact and low spin creepage. Because the assumptions made in the simulation are violated, it is possible that some combinations of vehicle speed and braking converge in the simulation while in reality they would lead to derailment. Indeed, some simulations resulted in a derailment quotient higher than Nadal's maximum, such as all cases with a braking co-

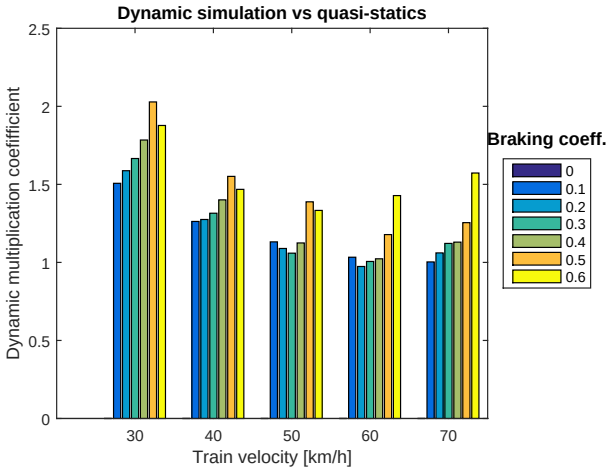


(a)

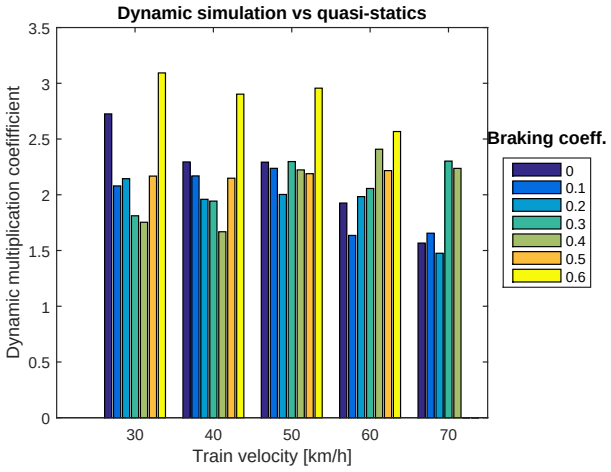


(b)

Figure 6.7: The ratio between the Y/Q ratios of from the dynamic simulation and from the quasi-static calculations (the dynamic multiplication coefficient), (a) for the curve, and b for the turnout.

6

efficient of 0.6 (irrespective of the speed) and braking coefficients of 0.4 and 0.5 at speeds higher than 70 km/h.

When the first wagon enters the turnout the locomotive starts braking. The dynamic effects of entering the turnout and the application of braking are combined. Entering a curve gives a sudden change in the lateral acceleration. Therefore, the lateral carbody modes are excited: the carbody sway, roll and yaw modes. They cause extra lateral force on the wheels; the maximum lateral force when applying braking after steadily curving is 29.5 kN, while the maximum lateral force when braking (with braking coefficient of 0.4)

upon entrance to the turnout is 48.4 kN, ignoring peaks in the force shorter than 50 ms. These lateral forces correspond to a derailment quotient of 0.20 without braking and 0.41 with braking (see Figure 6.5b). In the quasi-static calculations shown in Figure 6.5a these derailment quotients are, respectively, 0.085 and 0.23, which means that taking account of the dynamics increases the lateral force by 135% for a train coasting through the turnout and by 78% for braking with a braking coefficient of 0.4. Another observation is that the quasi-static derailment quotient in Figure 6.5a changes linearly with the braking coefficient. For the dynamic simulations, the increase in derailment quotient is irregular, though generally faster than linear with the braking coefficient. In fact, in the case of a braking coefficient of 0.6, the Nadal criterion is always exceeded even at low speed. From Figure 6.7b we can conclude that the derailment quotient from simulation is at most 3 times larger than the derailment quotient estimated from quasi-statics. So a dynamic multiplication coefficient of 3 can be used to obtain a conservative estimate of the dynamic derailment coefficient once the quasi static derailment coefficient has been calculated.

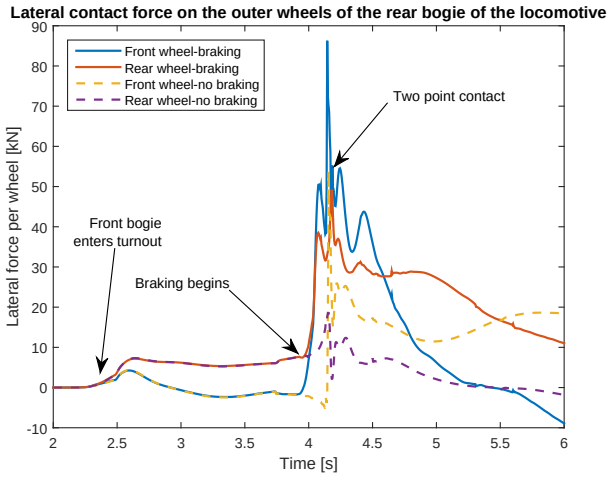


Figure 6.8: The lateral force on the outer wheels of the rear bogie of the locomotive when entering a 1:9 turnout obtained through vehicle dynamic simulation. Just before the rear bogie of the locomotive enters the turnout, the locomotive starts braking with a braking coefficient of 0.4.



## 6.4. DISCUSSION AND FURTHER RESEARCH

Seventy (2x5x7) vehicle simulations have been performed through a curve and a turnout, each with 5 different vehicle speeds and 7 different braking coefficients. Each simulation resulted in a maximum derailment quotient, that can be compared with the results from quasi-static calculatio to determine a dynamic multiplication coefficient. For braking while curving, the dynamic multiplication coefficient is 2.5, whereas for braking in a turnout the dynamic multiplication coefficient is 2.2. Moreover, in a turnout braking coefficients higher than 0.5 result in derailment irrespective of the vehicle speed. A con-

servative approach would be to adhere to a dynamic multiplication coefficient of 2.5 for all cases, while limiting the braking coefficient to 0.5. This outcome does not mean that a higher braking coefficient cannot be achieved, only that it should not be applied by the leading locomotive in a turnout. In an emergency situation the braking is usually applied all the wheels of a train, however attention needs to be paid to the timing with which the different braking systems are applied. Future research is needed to determine these dynamic multiplication coefficients for different turnouts, different curve radii and different train configurations. An experimental validation of the proposed approach can be achieved by measuring the Y/Q ratio by instrumented wheelsets or by measuring the displacement in the primary suspension [26]. The measures can then be used to validate the vehicle/train model. The determination of the dynamic multiplication coefficients would still needs to be obtained through vehicle dynamic simulations with a validated vehicle. This because the determination of the dynamic multiplication coefficient would require a vast number of simulations (different speeds, train composition, traction/braking effort), which would not be practically possible with measurements.

The case of braking is relevant for the scenario of a train entering a turnout at a speed higher than allowed and trying to correct that by strong braking. Because this is potentially a dangerous scenario, this chapter has chosen the braking scenario to show the methodology; however, the same methodology can be used for a trailing locomotive that initiates traction (acceleration). This scenario also results in compressive coupler forces and subsequently increased lateral forces from between wheel and rail. The quasi-static analysis would result in the same forces at the most loaded coupler, which in this case is the coupler between the locomotive and the last of the wagons.

The lateral forces originating from centripetal forces or from the lateral coupler forces can cause derailment, but also vehicle rollover due to wheel unloading. The common criterion for wheel unloading is that the vertical dynamic force on one wheel should be at least 60% of the normal wheel load (half the axle load). For a fast estimate of this vertical dynamic load the same methodology could be used as for the derailment coefficient in this chapter: making use of the moments cause by the centripetal force and lateral coupler force a quasi static vertical force can be calculated. This quasi-static vertical force can then be compared to dynamic vertical forces obtained through dynamic vehicle simulation to obtain a dynamic multiplication coefficient that is valid in a sufficiently large range of vehicle speed and traction/braking effort. Similarly as for the derailment coefficient it will be necessary to define a different dynamic multiplication coefficient for the case of a turnout (no transition curve) and for normal curves.



The train model here was of a passenger train consisting of a locomotive and 7 wagons; however, our methodology and the estimation/mapping method could be extended to long freight trains and provide a tool for heavy haul operators. Using a full model for each vehicle would generate a large number of degree of freedom in long trains and corresponding calculation time. This drawback can be avoided using the approach of [11]: a long train modeled with one degree of freedom per vehicle, with only the vehicles of interest are modeled in detail.

## 6.5. CONCLUSIONS

We propose a methodology to assess the increase in derailment risk due to pushing or braking a train through an estimate of the derailment quotient obtained by multiplying a derailment quotient calculated from quasi-statics by a dynamic multiplication coefficient. These derailment quotients can be compared to the Nadal criterion to assess the derailment risk. Based on vehicle dynamic simulations, the dynamic multiplication coefficient is estimated as 2 in curves and 3 in turnouts. and the braking coefficient of the locomotive should be limited to 0.5.

The derailment quotient has been mapped as function of speed and braking or traction (as a braking coefficient or as a total braking force). These maps are easy to interpret and do not require deep knowledge of the train dynamics; accordingly, they can be used by operators to determine a braking/traction strategy, either automated in a control system, or as guidelines to drivers. Two different couplers were considered: one transferring only force in the coupler direction and one that also transfers moment between the carbodies. The effect of the type of couplers on the lateral wheel-rail force was found to be small, approximately 8 %.

## REFERENCES

[1] C. Cole, *Longitudinal train dynamics,* in *Handbook of Railway Vehicle Dynamics*, edited by S. Iwnicki (Taylor and Francis, 2006) p. 239–278.

[2] C. Cole and Y. Sun, *Simulated comparisons of wagon coupler systems in heavy haul trains,* Proceedings of the Institution of Mechanical Engineers, Part F: Journal of Rail and Rapid Transit **220**, 247–256 (2006).

[3] V. K. Garg and R. V. Dukkipati, *Dynamics of railway vehicle systems* (Academic Press, 1984).

[4] T. Geike, *Understanding high coupler forces at metro vehicles,* Vehicle System Dynamics **45**, 389–396 (2007).

[5] S. Mohammadi and A. Nasr, *Effects of power unit location on in-tain longitudinal forces during brake application,* Int. J. of Vehicle Systems Modelling and Testing **5**, 176–196 (2010).

[6] M. Anseri, E. Esmailzadeh, and D. Younesian, *Longitudinal dynamics of freight trains,* Int. J. of Heavy Vehicle Systems **16**, 102–131 (2009).

[7] M. McClanachan, C. Cole, D. Roach, and B. Scown, *An investigation of the effect of bogie and wagon pitch associated with longitudinal train dynamics,* Vehicle System Dynamics **33**, 374–385 (2000).

[8] M. El-Sibaie, *Recent adcancements in buff and draft testing techniques,* Proceedinges of the 1993 IEEE/ASME joint conference **11**, 1–13 (1993).

[9] C. Cole, M. M. Spiryagin, and Y. Q. Sun, *Assessing wagon stability in complex train systems,* International Journal of Rail Transportation **1**, 193 (2013).

[10] S. Simson, *Three axle locomotive bogie steering, simulation of powered curving performance passive and active steering bogies*, Ph.D. thesis, Central Queensland University (2009).

[11] Z. Xu, W. Ma, Q.Wu, and S. Luo, *Coupler rotation behaviour and its effect on heavy haul trains,* Vehicle System Dynamics **51**, 1919–1838 (2013).

[12] Z. Xu, W. Ma, Q.Wu, and S. Luo, *Analysis of the rotation angle of a coupler used on heavy haul locomotives,* Proceedings of the Institution of Mechanical Engineers, Part F: Journal of Rail and Rapid Transit **228**, 835–844 (2013).

[13] R. Menssen and W. Kik, *Running through a switch - simulation and test,* Vehicle System Dynamics **23**, 378–389 (1994).

[14] E. Kassa and J. Nielssen, *Dynamic train-turout interaction in an extended frequency range using a detailed model of track dynamics,* Journal of Sound and Vibration **320**, 893–914 (2009).

[15] S. Alfi and S. Bruni, *Mathematical modeling of train-turnout interaction,* Vehicle System Dynamics **47**, 551–574 (2009).

[16] M. Wiest, E. Kassa, W. Daves, and J. Nielsen, *Assessment of methods for calculating contact pressure in wheel-rail/switch contact,* Wear **265**, 1439–1445 (2008).

[17] X. Shu, N. Nilson, C. Sasaoka, and J. Elkins, *Development of a real-time wheel/rail contact model in nucars and apllication to diamond crossing and turnout design simulations,* Vehicle System Dynamics **44**, 251–260 (2006).

[18] N. Burgelman, Z. Li, and R. Dollevoet, *A new rolling contact method applied to conformal contact and the train-turnout interaction,* Wear **321**, 94–105 (2014).

[19] C. Esveld, *Modern Railway Track* (MRT-productions, 2010) pp. 62–64.

[20] O. for Research and E. of the International Union of Railways, *Dynamic vehicle/track interaction phenomena from the point of track maintenance*, Tech. Rep. ORE D161 rp3 (1987).

[21] S. Jovanovic and C. Esveld, *Ecotrack: an objective condition-based decision support system for long-term track m&r planning directed towards the reduction of life cycle costs,* in *7th international Heavy Haul conference* (2001).

[22] S. L. Grassie, *Models of railway track and vehicle/track interaction at high frequencies: Results of benchmark test,* Vehicle System Dynamics **25**, 243 (1996).

[23] B. Dietrichs, M. Ekequist, S. Stichel, and H. Tengstrand, *Quasi-static modelling of wheel-rail contact reactions due to crosswind effects for various types of high speed rolling stock,* Proceedings of the Institution of Mechanical Engineers, Part F: Journal of Rail and Rapid Transit **218**, 133 (2004).

[24] B. Dirks and P. Wiersma, *Meting railprofiel tongbeweging van wissels 105A en 271 te Eindhoven*, Tech. Rep. (DeltaRail, 2007).

[25] O. Arias-Cuevas, Z. Li, and C. Esveld, *Simulation of the lateral dynamics of a railway vehicle and its validation based on rail wear measurements,* in *Proceedings of the ECCOMAS Thematic Conference on Multibody* (2007).

[26] A. Matsumoto, Y. Sato, H. Ohno, M. Shimizu, J. Kurihara, T. Saitou, Y. Michitsuji, R. Matsui, M. Tanimoto, and M. Mizuno, *Actual states of wheel/rail contact forces and friction on sharp curves – continuous monitoring from in-service trains and numerical simulations,* Wear **314**, 189–197 (2014).

# 7

# CONCLUSIONS AND RECOMMENDATIONS

## 7.1. CONCLUSIONS FROM THE EFFECT OF THE CONTACT METHOD ON THE VEHICLE SIMULATION

Chapters 2 and 3 quantified the effect of the contact method on the vehicle dynamic simulation. Chapter 2 focused on the position of the contact point, whereas Chapter 3 focused on the calculation of the tangential contact forces.

In Chapter 2, a method was presented to fast and accurately calculate the exact longitudinal position of the contact point: Wang's method, which was validated using a 3d mesh. Then a vehicle simulation was performed using the exact contact point location rather than assuming the contact takes place on the center line of the wheelset as is commonly done in vehicle software. However, it was concluded that even though the extra computational time is small, also the benefits are small, as the simulations have shown that the influence of the longitudinal position of the contact point on the vehicle simulation is negligible.

In Chapter 3, a number of different methods for solving the tangential contact problem and calculating the creep forces have been compared with each other with regard to their performance in online vehicle simulations. The simulation set-up introduced in this article may be too complex and too slow to be used for the simulation of vehicle dynamics on extended pieces of track. However this set-up allows for some theoretical investigations of the simulation process and more specifically the contact search and contact force algorithms. This set-up can also be useful for short simulations when a high accuracy is needed, for example for situations where extreme contact conditions (large contact angles, multiple contact points, etc.) are expected so that more accurate and time-consuming methods are needed.

By coupling a vehicle simulation software with Matlab we created a versatile tool that enables to investigate the influence of the wheel/rail interaction on the vehicle simulation. In this study only the influence of the creep forces was investigated, but future work could include the comparison of different methods to determine the contact point positions and different methods for the normal contact problem. Also online simulations using the Kalker's CONTACT or a extension thereof, such as WEAR (Chapter 4), will be possible.

It is concluded that the interpenetration models of Kik-Piotrowski, Linder and Stripes predict a better curving behaviour, lower creepages (12% lower) and creep forces (3% lower), than the elliptical model FastSim. Another finding is that, for curving the difference in the dynamic behaviour of the vehicle between the non-elliptical methods and FastSim is small for small contact angles, but significant for larger contact angles. This shows the need to use more accurate contact models for simulations of a vehicle negotiating a curve. From the simulations about hunting, it is concluded that the Kik-Piotrowski method results in a15% shorter wavelength, compared with the other models. The more sophisticated non-Hertzian method in this study, Stripes, results in a vehicle behaviour similar to those obtained with the other non-elliptical methods, especially Linder. Therefore, for the cases investigated in this study the need to use Stripes was not shown. There are, however, more extreme contact conditions, such as wheel/rail contact with heavily worn profiles, multiple-point contact, or contact on changing profiles, such as on the switch blade or frog in a turnout. For these extreme conditions, it might be

necessary to use a more complex method such as Stripes or even CONTACT or WEAR in the vehicle simulation.

## 7.2. CONCLUSIONS FROM CONTACT BETWEEN THE WHEEL AND THE SWITCH BLADE

In Chapter 4, to assess the contact stresses between the wheel and the switch blade of turnout we presented WEAR, a contact method designed to deal with complex contact geometry and with conformal contact.

WEAR was compared with CONTACT for the case of conformal contact. First, the difference in the calculation of the longitudinal rigid body slip between WEAR and CONTACT was compared analytically and demonstrated with a theoretical case of a rail with a constant rail radius. The relative error in the calculation of the longitudinal rigid body slip is 10-40% when assuming a planar contact patch, whereas the relative error on the lateral rigid body slip is 10-50%. Second, the case with real wheel and rail profiles was investigated. This case had contact angles ranging from 8° to 35°. The results show that the way in which the rigid body slip is calculated has a significant influence on the lateral local slip (i.e., up to 60 %) and longitudinal local slip (i.e., up to 37 %). In the case of two-point contact with contact on the rail head and gauge corner, CONTACT underestimates the local slip at the contact patch on the gauge side.

WEAR has shown to be able to capture and solve two-point contact problems occurring when the wheel transits from the stock rail to the switch blade. It can also capture an implicit (sub-)contact patch. The creep forces and shapes of the contact areas calculated with WEAR are reasonable and realistic. Moreover, WEAR converged in all cases; this robustness is required if the method is to be applied to online creep force calculations in vehicle dynamics simulations.

## 7.3. CONCLUSIONS REGARDING THE CALCULATION OF THE DISSIPATED POWER IN THE WHEEL/RAIL INTERFACE

In Chapter 5, several methods have been described to calculate the frictional energy. These methods are based on the creepages and creep forces ($T\gamma$ approach) at a reference point, with or without the spin moment being considered, or based on integral of the product of the local slip and tangential stress (stress-slip approach). The methods have been applied using FastSim or Kalker's full theory. It is concluded that for Kalker's full theory the $T\gamma$ with spin and the stress-slip approach result in almost the same frictional power. Another conclusion is that one has to be careful with the results from FastSim for cases where the spin creepage is dominant.

These methods have been applied in a theoretical analysis based on the longitudinal force balance of one wheel. For a straight track this theoretical analysis can be used to find the friction coefficient at which the frictional power is the smallest, and replace vehicle dynamic simulations for that purpose. It was concluded that both in curves and on straight track the optimal friction coefficient is significantly higher than the traction coefficient. However, in curves this approach cannot be used as some of the assumptions made were found to be in disagreement with vehicle dynamic simulations.

Finally, it is possible to compare measurements from the electric power consumption of the engines with simulations of the frictional power. The match between these has shown the same trend with respect to the frictional power as function of the friction coefficient, but a quantitative comparison is difficult due to uncertainties in both the measurements and the inputs to the vehicle model.

## 7.4. CONCLUSIONS FROM LONGITUDINAL TRAIN DYNAMICS

In Chapter 6, we have proposed a methodology to quickly assess the increase in derailment risk due to pushing or braking a train in a curve or turnout. An estimate of the derailment quotient is obtained by multiplying a derailment quotient calculated from quasi-statics with a dynamic multiplication coefficient. The dynamic coefficient was determined by comparing results from quasi-statics with those obtained with vehicle dynamic simulations as 2 for curves and 3 for turnouts. These dynamic derailment quotients can be compared to the Nadal criterion to assess the derailment risk.

The derailment quotient has been mapped as function of speed and braking or traction (as a braking coefficient or as a total braking force). These maps are easy to interpret and do not require deep knowledge of the train dynamics; accordingly, they can be used by operators to determine a braking/traction strategy, either automated in a control system, or as guidelines to drivers. Two different couplers were considered: one transferring only force in the coupler direction and the other also transfers moment between the carbodies. The lateral wheel/rail force obtained with the two types of couplers was found to be slightly different, approximately 8%.

## 7.5. RECOMMENDATIONS FOR FUTURE RESEARCH

As could be seen in the previous sections there are still some gaps in the simulation of train-turnout interaction and in the understanding of the phenomena happening at the interface.

### 7.5.1. RECOMMENDATIONS REGARDING THE SIMULATION OF LONG TRAINS

During the research we found the following opportunities for further research:

- It should be possible to extend the mapping approach presented in Chapter 6, so to include different turnouts, different types of vehicle couplers and different train configurations. Through extensive vehicle simulations, it should be possible to obtain a table of multiplication coefficients which then can be employed together with the quasi-static approach presented in Chapter 6.

- Another issue with long trains in curves is unloading of the outer wheels. A quick estimate of the risk associated to wheel unloading could be obtained using the approach presented in Chapter 6.

- Until now train couplers are mainly optimized for their behaviour in longitudinal direction. It will be interesting for train designers to include the influence of the couplers on the lateral forces in trains.

### 7.5.2. RECOMMENDATIONS REGARDING THE SIMULATION OF CONTACT IN TURNOUTS

During the research we found the following opportunities for further research:

- It will be interesting to couple Kalker's full theory, or a extension thereof such as WEAR, online with a vehicle simulation. This might be done with the methodology presented in Chapter 3. However, if WEAR is to be used online in a vehicle simulations some aspects of its algorithm would need to be updated:
  - The contact search should be separated from the main algorithm, so that the creepages are defined in a known reference point.
  - The effect of the non-planar contact patch has been accounted for in the calculation of the longitudinal rigid slip and the spin contribution to the lateral rigid slip. However, for the lateral rigid slip, the dependence on the local contact angle was not yet included. This could be accounted for with an approximate formula or by calculating all the rigid slip from the position and the velocity of the center of the wheelset rather than the three creepages in a reference point in the contact area.

  A dynamic coupling between the WEAR and the vehicle simulation will allow to evaluate the influence of the contact model on the wheelset's motion, and so obtain more accurate values for both the creepages and the tangential stress in the contact patch.
- A direct numerical validation can be done by comparing with results obtained with a model such as WEAR with a finite element model, such as that of [1, 2].
- Once WEAR is sufficiently validated it can be applied:
  - To obtain a better estimate of the stability of a vehicle traveling of an track with irregularities. A better estimate of the creep force is also important when considering derailment at switch blades.
  - To rolling contact fatigue: the location of the maximum tangential stress and its direction may be used to prediction RCF initiation
  - To profile wear and energy consumption in tight curves: WEAR should be especially suitable when conformal contact occurs.
- Although track flexibility and the wheel/rail contact have been extensively covered in the literature, the relation between between them is still to be investigated. Track flexibility could have an influence on the contact point location in the simulation and so on the train/turnout interaction.
- The electrical energy consumed by the trains engines is an indirect measure of the energy dissipated in the wheel/rail contact, which in its turn is related to wheel and rail material wear. Therefore a continuous measurement of the electrical energy consumed by the engines may give a continuous indication of the wear rate of the wheels and the rails.

## REFERENCES

[1] X. Zhao and Z. Li, *The solution of frictional wheel-rail rolling contact with a 3d transient finite element model: validation and error analysis,* Wear **271**, 444 (2011).

[2] X. Zhao and Z. Li, *A three-dimensional finite element solution of frictional wheel–rail rolling contact in elasto-plasticity,* Journal of Engineering Tribology **229**, 96 (2014).

# A

# OVERVIEW OF CONTACT METHODS

*This Appendix is meant to give an overview of all the contact methods used in this thesis. Many contact methods have been described in the literature using different notations; Moreover, many authors have been quit brief on the exact implementation of their method, as they were bound by the 'article style of writing' (limited number of pages; focus on 'why', not on 'how'). Therefore, this chapters intends to provide sufficient information for the implementation in a consistent notation, without investigating the results obtained with these methods.*

## A.1. WHEEL/RAIL CONTACT

The contact between the wheel of a train and the rail is a rolling contact between two bodies, the wheel and the rail which are stiff, meaning the deformation of the bodies is small compared to the size of the bodies. Because of the small deformation in the contact bodies, the contacting area is also small compared to the size of those bodies. This makes the nature of this contact very different than, for example, the contact between a car tire and a road. Owing to the small deformations the energy loss in the contact area is also small compared to that for road vehicles. However, the small contact area still needs to carry a large load, which results in large contact stresses. These stresses, together with the local slip between the wheel and the rail materials, cause the material wear of the wheel and rail and may cause material fatigue, or so-called Rolling Contact Fatigue (RCF).

Models have been developed to relate the relative position and velocity of a wheel to the contact forces and the stress and slip in the contact area. Most methods divide the rolling contact problem into three sub-problems: the contact location problem, the normal contact problem and the tangential contact problem. Only more advanced methods such as Kalker's full theory [1], derivations thereof [2] and finite element models [3, 4] can consider the coupling between the normal and the tangential problems.

### A.1.1. CONTACT POINT LOCATION

Most contact methods require a reference point to start from. Planar contact methods then assume that the entire contact area is on the plane tangential to the rail surface through that point. Moreover, most methods determine the relative motion between the wheel and the rail from the motion at that point. There can be multiple contact points per wheel/rail pair. These contact points can be treated as sub-contact areas with the same reference point (interpenetration methods, Kalker's full theory). In this case, it is assumed that the sub-contact areas are in the same plane. Another possibility is to define a different reference point for each contact. In this case there are multiple contact problems per wheel/rail contact, which are solved separately but are coupled through the position of the wheelset (determining the overlap between the wheel and rail profile and thereby the penetration depth) and the resulting contact forces, which must fulfil the equilibrium of force of the wheelset.

In a vehicle simulation, the total resultant force and resultant moments of all contact points at the centre of the wheelset are to be known. For the resulting moments, it is necessary to know the location of the contact forces. Although it would be possible to calculate the moments by integrating the normal and tangential stresses in the contact areas, it is more common to first calculate the resultant forces at each contact point and then calculate the resulting moments using the contact points' locations. It is commonly assumed that the contact areas are in the vertical plane through the wheel axis; this assumption is further investigated in Chapter 2.

## A.2. THE NORMAL CONTACT PROBLEM

First, there is the normal contact problem, in which the relation between the position of the two contact bodies (i.e., wheel and rail) and the normal pressure distribution be-

tween the bodies must be determined. The position between the bodies is often defined using the penetration depth (Figure A.1a), the maximum distance of the overlap of the bodies if they were considered undeformable.

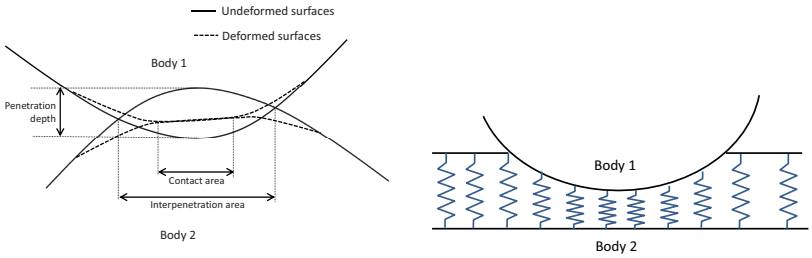


(a) (b)

Figure A.1: (a) The penetration depth and the deformed and undeformed surfaces of the contacting bodies, and (b) a Winkler foundation



### A.2.1. WINKLER FOUNDATION

A simple method for determining the contact pressure would be to assume that the local contact pressure is proportional to the local penetration depth (Figure A.1b). For two spheres pressed against each other, this assumption would result in a parabolic contact pressure distribution. This approach is, however, never used for wheel/rail contacts as it is experimentally and analytically proven to be inaccurate. Moreover, there is no need for such a method, because the Hertzian method (explained in the next section) already offers a calculation time short enough for any application.

### A.2.2. HERTZIAN CONTACT

In 1881, Hertz published his theory on the contact between elastic bodies [5]. The main assumptions of the theory are as follows:

- The material of the bodies is elastic.
- The stress field in the bodies can be approximated by stress fields in an infinite half-space.
- The contact area is small compared to the local curvature of the contacting bodies.
- The curvatures are constant inside the contact patch.

With these assumptions, the Hertzian theory predicts a planar elliptical contact patch and an ellipsoidal contact pressure distribution. The size of the contact area (the semi-axes of the ellipse: $a$ and $b$) and the penetration depth ($d$) can be calculated from the normal contact force ($F_n$) and the local curvatures of the contacting bodies as follows (with the notation of [6]).

The relative curvatures of the contacting bodies in longitudinal and lateral directions respectively are:

$$A = \frac{1}{2r_{wy}} \tag{A.1}$$

and

$$B = \frac{1}{2}\left(\frac{1}{R_{wx}} + \frac{1}{R_{rx}}\right) \tag{A.2}$$

with $R_{wy}$ the rolling radius of the wheel, $R_{wx}$ the local radius of the wheel profile in lateral direction and $R_{rx}$ the local radius of the rail profile in lateral direction. If the rail profile is known as a function $z_r(y)$ then the local radius of the rail profile can be found as:

$$R_{rx} = \frac{\left(1 + z_r'^2\right)^{3/2}}{z_r''} \tag{A.3}$$



where $z' = \frac{\partial z_r(y)}{\partial y}$. $R_{wx}$ can be found in a similar way.

The contact ellipse is defined by its semiaxis $a$ and $b$:

$$a = m\left(\frac{3}{2}F_n\frac{1-\nu^2}{E}\frac{1}{A+B}\right)^{1/3} \tag{A.4}$$

$$b = n\left(\frac{3}{2}F_n\frac{1-\nu^2}{E}\frac{1}{A+B}\right)^{1/3} \tag{A.5}$$

The penetration depth, $d$, can be found as

$$d = r\left(\left(\frac{3}{2}F_n\frac{1-\nu^2}{E}\right)^2(A+B)\right)^{1/3} \tag{A.6}$$

$n$, $m$, and $r$ are non-dimensional coefficient which can be tabled as function of $\theta = \frac{|B-A|}{B+A}$.

A table can be found in [6] page 91 as well as an analytical approximation of the tables. With these, the contact area is known, the contact pressure is an ellipsoid with maximum contact pressure $\sigma_{\max} = \frac{3F_n}{2\pi ab}$.

### A.2.3. INTERPENETRATION METHODS

The interpenetration methods estimate the contact area based on an area in which the bodies overlap if they are considered undeformable (Figure A.1a). This area is larger than the real contact area. This problem is solved by employing a virtual penetration depth instead of the real penetration depth. This virtual penetration depth is assumed to be proportional to the real penetration. The contact area is then assumed to be the area in which the two bodies overlap when they approach each other by the virtual penetration depth [7].

It is then assumed that the contact pressure distribution is elliptic in the longitudinal distribution and proportional to the contact patch width in the lateral distribution.

The Piotrowski [8], Linder [9] and use the contact pressure based on the interpenetration area with a virtual penetration 0.55 times the real penetration. The Linder method use this area directly while the Piotrowski method first applies a correction function on the obtained area.

### PIOTROWSKI METHOD

*All formulas in this section are adapted from Piotrowski [8]*

The following describes Piotrowski's algorithm to obtain the normal contact force (and the normal contact pressure) based on a prescribed penetration, $d$:

1. shift the wheel profile vertically so that just one point is in contact. Then move the wheel profile down with $d\,tz = 0.55d\cos\delta$.

2. determine the elements in the overlapping region (find the indices where $z_w < z_r$, then remove all other elements from the $y_r$, $z_w$ and $z_r$ vectors). Now calculate the y-coordinates in the frame in a reference frame tangential to the contact patch (see Figure A.2) at the reference point using the contact angle at that reference point $y = \frac{y_r - y_r 0}{\cos\delta}$ (see Figure A.3a). This formula is base on the assumption that the local penetration is small compared to the contact area, which is always the case.

3. Calculate the width of the contact area, $W = y_{\max} - y_{\min}$, the local penetration, $d_l = (z_r - z_w)\cos\delta$ (see Figure A.3b). So that the length of the contact area becomes, $L = 2L_{l,\max}$. Relocate the origin of the reference frame so that $y = 0$ where $d_l$ is maximum.

4. Calculate the corrected width, $W_c$, and length, $L_c$, of the contact area

$$L_c = \sqrt{\frac{LW}{\beta}} \tag{A.7}$$

$$W_c = \sqrt{LW\beta} \tag{A.8}$$

where $\beta$ is described empirically:

$$\beta = \begin{cases} (0.5837(W/L)^2 - 0.1053(W/L)^4 + 0.5184W/L)^{-1} & (W/L) \leq 1 \\ 0.5837(L/W)^2 - 0.1053(L/W)^4 + 0.5184L/W & (W/L) > 1 \end{cases} \tag{A.9}$$

5. Use the corrected Width and length to find the corrected lateral positions as

$$y_c = y\left(1 + \frac{W_c - W}{W}\right) \tag{A.10}$$

Calculate the local length, $L_l$, of the contact area as:

$$L_c = 2\sqrt{2R_c d_l} \tag{A.11}$$

With $R_c$ the corrected Hertzian radius of curvature in longitudinal direction:

$$R_c = \frac{1}{8d_0}L_c^2 \tag{A.12}$$

6. When the contact shape is known, the contact pressure distribution is supposed to be elliptical in the rolling direction and proportional to the local longitudinal width of the contact area, so that the normal contact force becomes:

$$F_n = \frac{\pi E \delta}{2(1-\nu^2)} \frac{\sum_{y=y_{\min}}^{y_{\max}} \sum_{x=-L_l(y)}^{L_l(y)} \sqrt{L_l^2 - x^2}}{\sum_{y=y_{\min}}^{y_{\max}} \sum_{x=-L_l(y)}^{L_l(y)} \frac{\sqrt{L_l^2-x^2}}{\sqrt{x^2+y^2}}} \tag{A.13}$$

The contact pressure distribution is:

$$\sigma_z(x,y) = \sigma_0 \frac{L_l(y)}{L} \sqrt{1 - \left(\frac{2x}{L_l(y)}\right)^2} \tag{A.14}$$

An expression for $p_0$ as function of the penetration and the contact shape can be found in [8]:

$$\sigma_0 = \frac{F_n \sqrt{2Rd_0}}{\sum_{y=y_{\min}}^{y_{\max}} \sum_{x=-L_l(y)}^{L_l(y)} \sqrt{L_l^2 - x^2}} \tag{A.15}$$

Where $E$ is the Young's modulus and $\nu$ the Poisson ratio of the contacting bodies, assuming the bodies are made of the same material.

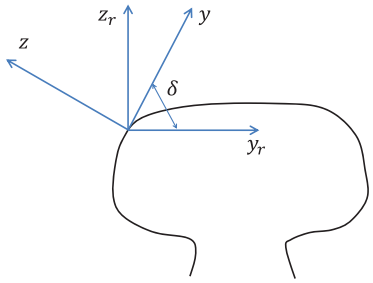


Figure A.2: The horizontal reference frame: $(y_r, y_r)$ and the reference frame tangential to the rail surface at the reference point: $(y, y)$

### LINDER METHOD

*All formulas in this section are adapted from Linder's PhD-thesis [9]*

The following describes Linder's algorithm to obtain the normal contact force (and the normal contact pressure distribution) based on a prescribed penetration, $d$:

1. shift the wheel profile vertically so that just one point is in contact. Then move the wheel profile down with $0.55d$.

2. determine the elements in the overlapping region (find the indices where $z_w < z_r$, then remove all other elements from the $y_r$, $z_w$ and $z_r$ vectors). Now calculate

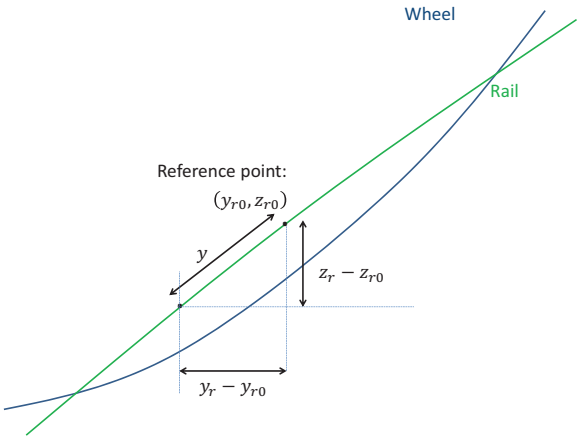


(a)

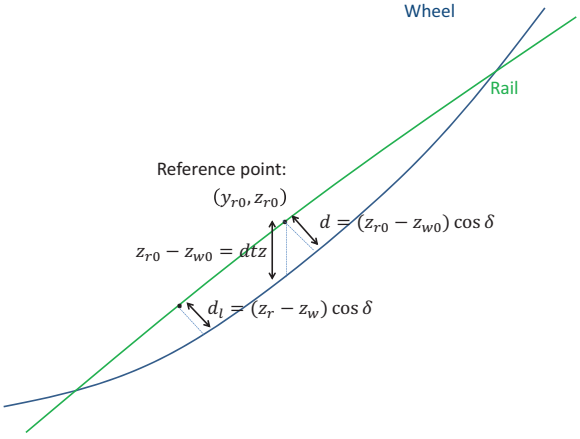


(b)

Figure A.3: (a) y-coordinate reference frame tangential to the contact patch as function of the rail coordinates ($y_r$ and $y_r 0$) and the contact angle ($\delta$) and (b) the local penetration ($d_l$) and the vertical penetration ($dtz$) as function of the wheel and rail coordinates ($z_w$ and $z_r$) and the contact angle.

the y-coordinates in the frame in a reference frame tangential to the contact patch (see Figure A.2) at the reference point using the contact angle at that reference point $y = \frac{y_r - y_r 0}{\cos\delta}$ (see Figure A.3a).

3. Calculate the width of the contact area, $W = y_{\max} - y_{\min}$, the local penetration, $d_l = (z_r - z_w)\cos\delta$ (see Figure A.3b). So that the length of the contact area becomes,

$L = 2L_{l,\max}$. The local length of the contact area, $L_l = 2\sqrt{2R_r d_l - d_l^2}$. Now relocate the origin of the reference frame so that it is in the middle of the contact area ($y = 1/2(y_{\max} + y_{\min})$)

4. In each line of elements in the rolling direction an equivalent ellipse is defined (see Figure A.4). The width of these equivalent ellipses is constant throughout the whole contact area and set equal to the contact width (semi-axis $b_{\text{ell}} = W/2$). The length of each ellipse is determined as (with $i = 1 : m$, $m$ the number of elements in lateral direction):

$$a_{\text{ell}}(i) = \frac{L_l(i)}{2} \frac{b_{\text{ell}}}{\sqrt{b_{\text{ell}}^2 - y(i)^2}} \tag{A.16}$$

For each line also an equivalent penetration is defined as:

$$d_{\text{ell}}(i) = z_m(i) + \sqrt{b_{\text{ell}}^2 + z_m(i)^2} \tag{A.17}$$

with:

$$z_m(i) = \frac{y(i)^2 + d_l'(i)^2 - b_{\text{ell}}^2}{2d_l'(i)} \tag{A.18}$$

where $d_l'(i) = d_l(i)/0.55$. While the contact area was based on the virtual penetration the Hertzian ellipse in each longitudinal line is based on a real penetration.

5. From $a_{\text{ell}}$, $b_{\text{ell}}$ and $d_{\text{ell}}$ the equivalent normal force of the each ellipse can be calculated as:

$$F_{\text{ell}}(i) = \frac{\pi}{3} a_{\text{ell}} d_{\text{ell}}(i) \frac{E}{(1-\nu^2)F(e(i))} \tag{A.19}$$

with $F(e)$ the elliptical integral (*ellipke* in Matlab) of:

$$e(i) = \sqrt{1 - \left(\frac{a_{\text{ell}}(i)}{b_{\text{ell}}}\right)^2} \tag{A.20}$$

These are the formulas for $a < b$, for $a > b$ a and be should be exchanged.

6. with the normal force in each equivalent ellipse we can calculate the maximum pressure in each line in the lateral direction as:

$$\sigma_{\max}(i) = \frac{3N_{\text{ell}}}{2a_{\text{ell}} b_{\text{ell}} \pi} \sqrt{1 - \frac{y(i)^2}{b_{\text{ell}}^2}} \tag{A.21}$$

7. With the maximum contact pressure in each line, the total contact force can be calculated as:

$$F_n = \sum_{i=1}^{m} \frac{\pi}{2} \sigma_{\max}(i) L_l(i) dy \tag{A.22}$$

The contact pressure distribution can be found as:

$$\sigma_z(i,j) = \sigma_{\max}(i) \sqrt{1 - \left(\frac{2x(i)}{a_{\text{ell}}(i)}\right)^2 - \left(\frac{y(i)}{b_{\text{ell}}}\right)^2} \tag{A.23}$$

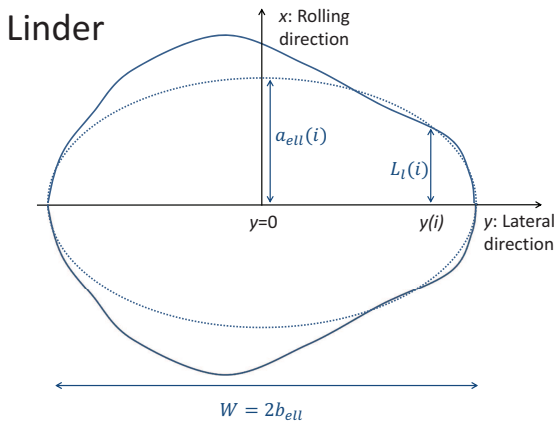


Figure A.4: The contact area and an equivalent ellipse as used in the Linder method.



### STRIPES METHOD

*All formulas in this section are adapted from Ayasse and Chollet [10]*

The Stripes method [10] does not use a fixed virtual penetration but one dependent on the local curvatures of the wheel and the rail: A and B (as defined in equations A.1 and A.2).

The following describes Stripes algorithm to obtain the normal contact force (and the normal contact pressure distribution) based on a prescribed penetration, $d$:

1. calculate the local contact angle in each point on the wheel and the rail surface. Then take the average of these: $\delta_i$
2. calculate the local curvatures A and B (using Equations A.1 and A.2) in each point.
3. Calculate the virtual penetration $d'$ as:

$$d' = \frac{n^2}{r_0\left(1+\left(\frac{n}{m}\right)^2\right)}d \tag{A.24}$$

   where $n$, $m$ and $r$ are based on the curvature $A_0$ and $B_0$ in a reference point.
4. The vertical penetration, $dtz$ (See Figure A.3b), can be obtained through a first order approximation

$$dtz = \frac{d'}{\cos\delta_0} \tag{A.25}$$

   where $\delta_0$ is the contact angle at the reference point.
5. shift the wheel profile vertically so that just one point is in contact. Then move the wheel profile down with $dtz$.

6. determine the elements in the overlapping region (find the indices where $z_w < z_r$, then remove all other elements from the $y$, $z_w$ and $z_r$ vectors). Now calculate the y-coordinates in the frame in a reference frame tangential to the contact patch (see Figure A.2) at the reference point using the contact angle at that reference point $y = \frac{y_r - y_r 0}{\cos\delta}$ (see Figure A.3a). Then calculate the width of the contact area, $W = y_{\max} - y_{\min}$. The local penetration is calculated with the local contact angle rather than the reference contact angle (such as with Piotrowski and Linder): $d_{li} = \frac{(z_{ri} - z_{wi})}{\cos\delta_i}$.

7. The AB correction performed later can give sharp variation for wheel/rail profiles with discontinuities of the curvatures. These can be avoided by smoothing of B, with filter based on the Boussinesq approach (use *bvp4c* in Matlab):

$$\frac{dB_f}{ds} = \frac{B - B_f}{\frac{3}{2} l_0} \tag{A.26}$$

A

where $B_{fi}$ is the smoothed version and $l_0$ is a characteristic length defined by:

$$l_0 = \left( \frac{3}{2} F_n \frac{1 - \nu^2}{E} \frac{1}{A + B} \right)^3 \tag{A.27}$$

8. Sometimes (especially when the contact area consists of several sub-contact areas) $B_i$ can be negative. To avoid numerical problems, set all negative $B_{fi}$ to a small positive value.

9. calculate the local $n_i$, $m_i$ and $r_i$ from each local ellipse from the local curvatures $A_i$ and $B_i$ from the tables in [6] page 91.

10. Calculate the corrected local curvatures $A_{ci}$

$$A_{ci} = \frac{(A_i + B_i)(n_i/m_i)^2}{1 + (n_i/m_i)^2} \tag{A.28}$$

11. calculate the local with of the contact area as

$$W_{li} = 2\sqrt{\frac{d_{li}}{A_{ci}}} \tag{A.29}$$

12. the Stripes method suggests to use two different contact pressures distributions.

    - An elliptical distribution:

$$\sigma_z(x, y) = \frac{1}{\pi} \frac{1 + \left(\frac{n_i}{m_i}\right)^2}{n^3} \frac{E}{1 - nu^2} \frac{2 d_{li}}{W_{li}} \sqrt{1 - \left(\frac{x}{a_i}\right)^2} \tag{A.30}$$

      where $k_i = \delta_i / \delta_0$. The elliptical distribution is used to determine the normal force.

Or a parabolic distribution which should be used to determine the traction bound for tangential contact methods:

$$\sigma_z(x,y) = \frac{4}{3\pi}\frac{1+\left(\frac{n_i}{m_i}\right)^2}{n^3}\frac{E}{1-nu^2}\frac{2d_{li}k_i}{W_{li}}\left(1-\left(\frac{x}{a_i}\right)^2\right) \tag{A.31}$$

## A.3. THE TANGENTIAL CONTACT PROBLEM

Once the normal contact pressure is known, the tangential problem may be solved. The tangential problem consists of the relation between the relative motion of the two bodies and the tangential stresses/forces on the contact surfaces. This motion is the slip between the wheel and the rail. For contact between a wheel and a rail, it is often assumed that the tangential contact problem is independent of the vehicle speed, such that the tangential forces depend on the relative slip, the so-called creepage, rather than the real slip.



### A.3.1. CREEPAGES

The creepage is the relative slip between the wheel and the rail. The longitudinal ($\eta$), lateral ($\nu$) and spin ($\psi$) creepage can be defined as follows:

$$\nu_x = \frac{V_w - \omega R_{loc}}{V_{\text{ref}}} \tag{A.32}$$

$$\nu_y = \frac{V_{\text{lat}}}{V_{\text{ref}}} \tag{A.33}$$

$$\Psi = \frac{\Omega_n}{V_{\text{ref}}} \tag{A.34}$$

were:

- $V_{\text{ref}}$ is the reference speed, normally the forward velocity of the centre of mass of the wheelset.
- $V_w$ is the forward velocity of the wheel.
- $\omega$ is the rotational velocity of the wheelset
- $R_{\text{loc}}$ is the local rolling radius of the wheel.
- $V_{\text{lat}}$ is the lateral velocity of the wheel.
- $\Omega_n$ is the projection of the rotational velocity of the wheelset on the normal to the local rail surface.

Creepage is a local property for each point in the contact area; therefore, they may also be referred to as relative rigid body slip because it is essentially a local relative velocity between the wheel and the rail when both are considered undeformable. The creepages can be calculated for each of the points in the contact area directly or more often

for one reference point after which the local creepages are calculated from the reference point.

In case the vehicle is stead curving the creepages can be approximated as follows:

$$\nu_x = \frac{y\gamma}{R_w} - \frac{l}{2R_{\text{curve}}} \tag{A.35}$$

With $R_w$ the nominal radius of the wheel and $R_{\text{curve}}$ the curve radius. This equation assumes a constant conicity, $\gamma$, of the wheel and a linear relation between the longitudinal creepage and crepe force. It also requires the knowledge of $y$, the lateral displacement of the wheelset.

$$\nu_y = \frac{\alpha}{\cos\delta} \tag{A.36}$$

$$\psi = \frac{\sin\delta}{R_w} \tag{A.37}$$

with:

- $\alpha$: the yaw angle of the wheelset.
- $\delta$: the contact angle.

Equation A.36 is often reported in the literature (e.g., [6]) as $\nu_y = \alpha$. However, $\alpha$ is the horizontal/lateral component of slip of the wheel on the rail, whereas we are interested in the slip in the plane tangential to the contact area, hence the division by $\cos\delta$. The division by $\cos\delta$ does not require much computational effort, as the contact angle needs to be known in any case to solve the contact problem. Moreover this addition makes the formula more versatile: It covers not only tread contact but also flanging contact.

### A.3.2. CREEP-FORCE CURVE

The relation between the creepages and the creep force can be obtained experimentally through a twin-disk test. This test es easiest to perform for the longitudinal creepage/creep force. The creep curve in Figure A.5, shows that at low creepage the relation is linear therefore,n the creep force reaches a maximum and then becomes constant or decreases slightly with the creepage. In the linear regime, the contact area is partially in slip, in that part of the area there is adhesion, no slip. This situation occurs normally on the leading edge of the contact area, whereas the other part is in slip. After the creep force reaches its maximum, the contact area is in full slip. For this case, often Coulomb friction is used such that the tangential force equals the friction coefficient times the normal force. Alternatively, a speed-dependent friction coefficient might be used to match the falling creep force observed experimentally.

In railways, during traction or braking of a train, it is desirable to reach the maximum tangential force and the corresponding creepage. For all other cases, the creepages are desired to be small because they cause slip and hence energy loss.

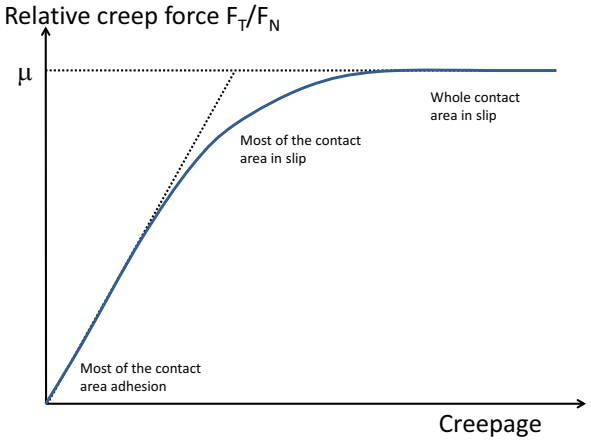


Figure A.5: The creep force relative to the normal force as function of the creepage.



### A.3.3. CALCULATION OF THE RIGID SLIP

The rigid slip is the local slip that would occur between the two contacting bodies if they were considered undeformable. For most contact methods (except the analytical ones presented in Section A.3.4) the rigid slip needs to be known at each point in the contact area, assuming the contact area is planar the rigid slip can be calculated from the creepages at one reference point. Figure A.6 shows that the rigid slip $(c_x(x,y), c_y(x,y))$ can be calculated when the creepages $(v_{x0}, v_{y0}, \Psi_0)$ at the origin of the reference frame are known:

$$c_x(x,y) = V(v_{x0} + y\Psi_0) \tag{A.38}$$

$$c_y(x,y) = V(v_{y0} - x\Psi_0) \tag{A.39}$$

where $V$ is the reference velocity and $y_n$ is tangential distance from the reference point (see Figure A.2).

In addition to calculating the local slip from the slip at the reference point, these equations also change a dimensionless parameter (creepage) into a parameter with the dimension of velocity (the rigid slip). This transformation is performed because in the following sections we define equations using the displacements and velocities rather than their dimensionless counterparts, as some other authors do. Note that these equations are only valid when the contact area is planar; the rigid slip for conformal contact is further discussed in Chapter 4 and Sections A.3.6.1 and A.3.8.

### A.3.4. ANALYTICAL METHODS

Analytical methods estimate the creep force as a function of the creepages. The basic methods assume that the creep forces are proportional to the creepages [1], whereas other methods assume more complex relations [11, 12].

The linear approach is as follows:

$$F_x = -GabC_{11}v_x \tag{A.40}$$

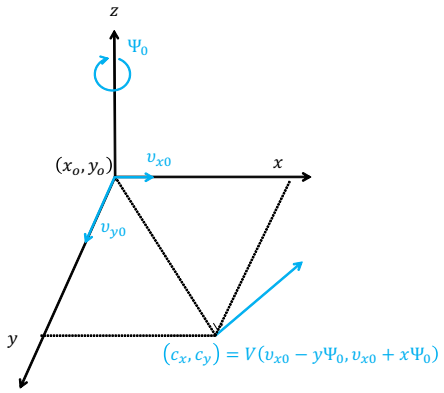


Figure A.6: Schematic drawing of the rigid slip ($c_x$,$c_y$) as function of the creepages ($v_{x0}$,$v_{y0}$,$\Psi_0$) in the origin of the reference frame.



$$F_y = -GabC_{22}v_y - G(ab)^{2/3}C_{23}\Psi \tag{A.41}$$

$$M_z = G(ab)^{2/3}C_{23}v_y - G(ab)^2C_{33}\Psi \tag{A.42}$$

with

- $F_\eta$: the longitudinal creep force.
- $F_v$: the lateral creep force.
- $M_n$: the spin moment around the normal to the contact area.
- $C_{11}$, $C_{22}$, $C_{23}$ en $C_{33}$: so called Kalker's coefficients or creepage coefficients that depend on the size of the contact area (semi-axis a en b) and the Poisson coefficient.

### A.3.5. KALKER'S COEFFICIENTS

$C_{11}$, $C_{22}$, $C_{23}$ en $C_{33}$ can be found in tables (in [13] page 26 or in [6] page 100). Alternatively $C_{11}$, $C_{22}$ and $C_{23}$ can be obtained through empirical formulas as (assuming the material is steel, so the Poisson coefficient is 0.27):

$$C_{11} = 3.2893 + \frac{0.975}{b/a} - \frac{0.012}{(b/a)^2} \tag{A.43}$$

$$C_{22} = 2.4014 + \frac{1.3179}{b/a} - \frac{0.02}{(b/a)^2} \tag{A.44}$$

$$C_{23} = 0.4147 + \frac{1.0184}{b/a} + \frac{0.0565}{(b/a)^2} - \frac{0.013}{(b/a)^3} \tag{A.45}$$

These equations are sufficiently accurate when $1/25 < b/a < 25$.

### A.3.6. FASTSIM

*All formulas in this section are adapted from Kalker [13]*

FastSim is based on the simplified theory of Kalker [14, 15]; its two main assumptions are as follows:

- The tangential contact stress is proportional to the local tangential displacement. The ratio between them is called the flexibility parameter. Note that this assumption is the tangential equivalent of the Winkler foundation (Section A.2.1).
- The tangential stress at the leading edge is zero; from there, the algorithm proceeds in the longitudinal direction and builds up the stress. This procedure is performed line per line in the lateral direction till the whole contact area is covered.

$$u_{x,y} = L\sigma_{x,y} \tag{A.46}$$

$$L = \frac{L_1 |v_x| + L_2 |v_y| + L_3 |\Psi| \sqrt{ab}}{\sqrt{v_x^2 + v_y^2 + ab\Psi^2}} \tag{A.47}$$

where:

$$L_1 = \frac{8a}{3GC_{11}} \tag{A.48}$$

$$L_2 = \frac{8a}{3GC_{22}} \tag{A.49}$$

$$L_3 = \frac{\pi a^2}{4G\sqrt{ab}C_{23}} \tag{A.50}$$

We adapted the formulas from [13]; in each element (i,j):

- Assume there is no slip ($\mathbf{s}(i,j) = 0$)
- Calculate the tangential stress as:

$$\boldsymbol{\sigma}(i,j) = \boldsymbol{\sigma}(i-1,j) - \frac{k}{L}\mathbf{c}(i,j) \tag{A.51}$$

  where $k = \frac{dx}{V}$, $L$ is the flexibility parameter and $\mathbf{c}$ is the rigid body slip, found with equations A.38 and 1.8.

- Check whether $|\boldsymbol{\sigma}(i,j)| \geq \mu p_z(i,j)$, where $p_z$ is the normal contact pressure and $\mu$ is the friction coefficient, if this logic expression is true the element is in slip else the element is in adhesion.
- In case of slip:

$$\boldsymbol{\sigma}(i,j) = \frac{\boldsymbol{\sigma}(i,j)}{|\boldsymbol{\sigma}(i,j)|}\mu p_z(i,j) \tag{A.52}$$

- Update the tangential forces

$$F_x = F_x + \sigma_x(i,j)dxdy \tag{A.53}$$

$$F_y = F_y + \sigma_y(i,j)dxdy \tag{A.54}$$

- go to the next element in longitudinal direction, once the trailing edge is reached: start with the next line in lateral direction at the leading edge with the tangential stress zero.

### MODIFIED FASTSIM FOR INTERPENETRATION METHODS

The interpenetration methods introduced in Section A.2.3 also be used for the solution of the tangential contact problem. All these methods rely on an extension of the FastSim method; specifically, they apply the FastSim algorithm on the contact pressure distribution found using the interpenetration approach. There are two mean factors to consider: the flexibility parameter and the rigid body slip.



- The flexibility parameter is either held constant throughout the entire contact area (the Kik-Piotrowski method [16]) or the contact area is divided in longitudinal strips each with its own flexibility parameter (the Linder and Stripes methods).

- The Kik-Piotrowski and the Linder methods calculate the rigid body slip using equations A.38 and A.39, as in the original FastSim method, whereas the Stripes method accounts for non-planar contact areas, which have a varying spin creepage as [10]:

$$c_x(x,y) = V\left(\nu_{x0} + \frac{y}{R_0}\sin\delta_l\cos\delta_y\right) \tag{A.55}$$

$$c_y(x,y) = V\left(\nu_{y0} - x\frac{\sin\delta_l}{R_0}\right) \tag{A.56}$$

  where $\delta_0$ is the contact angle in the reference point (the point where $\nu_{x0}$ and $\nu_{y0}$ are defined) and $\delta_y$ is the local contact angle. This approach is assumes the local curvatures of the wheel and rail are constant in the contact area.

  However, the author of this dissertation suggest using the following instead:

$$c_x(x,y) = V\left(\nu_{x0} + \frac{z_r - z_{r0}}{R_0}\right) \tag{A.57}$$

$$c_y(x,y) = V\left(\nu_{y0}\frac{\cos\delta_0}{\cos\delta_y} - x\frac{\sin\delta_y}{R_0}\right) \tag{A.58}$$

  where $z_r - z_{r0}$ is the vertical difference with the reference point. Equation A.57 is exact, whereas Equation A.58 assumes the lateral creepage is caused only from the horizontal velocity of the wheel (the vertical velocity of the wheel and the roll angle rate are assumed negligible).

A last difference with Stripes compared to the others is that the change in contact angle in the contact area is accounted for when calculating the total contact forces:

$$F_y = \sum\sum \sigma_y \cos(\delta_y - \delta_0) - \sigma_z \sin(\delta_y - \delta_0) \tag{A.59}$$

$$F_z = \sum\sum \sigma_y \sin(\delta_y - \delta_0) + \sigma_z \cos(\delta_y - \delta_0) \tag{A.60}$$

$F_y$ is still the total force tangential to the contact area at the reference point in lateral direction, however, it does not only include frictional components, but also a component from the normal contact pressure, $\sigma_z$. Similarly, the normal force at the reference, $F_n$, now also include a frictional component originating from $\sigma_y$.

### A.3.7. KALKER'S FULL THEORY

*All formulas in this section are adapted from Kalker [13]*

Kalker's full theory was developed by Kalker over a long period, beginning with publications in 1966 and 1968 [17, 18] and culminating in the publication of a book in 1990 [1]. In 2001 Kalker wrote a more accessible summary of his work for a course at the International Centre for Mechanical Sciences [13].

To solve the normal and the tangential problem to have a relation between the local displacements and stresses must be established. Whereas in the simplified theory the local stress is proportional with the local displacement, in the full theory the local displacement is a function of the stress at all other points in the contact area. When the material is assumed to be linear elastic the displacements in a point $(x, y)$ can be expressed as function of the stresses in each element J (J=1:N; N the number of elements) with the use of influence numbers ($A$) as follows:

$$u_x(x,y) = \sum_{J=1}^{N} \left( A_{xJx}(x,y)\sigma_{xJ} + A_{xJy}(x,y)\sigma_{yJ} \right) \tag{A.61}$$

$$u_y(x,y) = \sum_{J=1}^{N} \left( A_{yJx}(x,y)\sigma_{xJ} + A_{yJy}(x,y)\sigma_{yJ} \right) \tag{A.62}$$

$$u_z(x,y) = \sum_{J=1}^{N} \left( A_{zJz}(x,y)\sigma_{zJ} \right) \tag{A.63}$$

Note that the normal and the vertical displacement and forces are decoupled. This is the true as long as the half-space assumption holds and contact between bodies with the same material is considered. The half-space assumption means that the boundary conditions are for the real body, but the elasticity equations are solved for a half-space. This is a good approximation as long as the contact area is small with respect to the minimum radius curvature of near the contact.

With the half-space assumption the influence numbers can be calculated analytically through the Boussinesq-Cerruti equations [19, 20] (Also found in [21]):

$$A_{xJx}(x,y) = \left[ \left[ \frac{y\ln(x+r) + (1-\nu)x\ln(y+r)}{\pi G} \right]_{x-x_J-\Delta x}^{x-x_J+\Delta x} \right]_{y-y_J-\Delta y}^{y-y_J+\Delta y} \tag{A.64}$$

$$A_{xJy}(x,y) = A_{yJx}(x,y) = \left[\left[\frac{-\nu r}{\pi G}\right]_{x-x_J-\Delta x}^{x-x_J+\Delta x}\right]_{y-y_J-\Delta y}^{y-y_J+\Delta y} \tag{A.65}$$

$$A_{yJy}(x,y) = \left[\left[\frac{x\ln(y+r)+(1-\nu)y\ln(x+r)}{\pi G}\right]_{x-x_J-\Delta x}^{x-x_J+\Delta x}\right]_{y-y_J-\Delta y}^{y-y_J+\Delta y} \tag{A.66}$$

$$A_{zJz}(x,y) = \left[\left[\frac{(1-\nu)(x\ln(y+r)+y\ln(x+r))}{\pi G}\right]_{x-x_J-\Delta x}^{x-x_J+\Delta x}\right]_{y-y_J-\Delta y}^{y-y_J+\Delta y} \tag{A.67}$$

with $r = \sqrt{x^2+y^2}$, and $\Delta x$ and $\Delta y$ the element sizes.

With the relation between the stresses and the local displacements defined, the normal and the tangential contact is split. To calculate the contact pressure distribution from the penetration:

A

1. Define and mesh a potential contact area: P.
2. Calculate the undeformed distance between the two bodies: $d(I)$ $(I = 1:N)$, where d is negative where the rigid bodies overlap and positive elsewhere.
3. Set $\sigma_z(I) = 0$
4. Call the contact area C and the exterior E. Set initially all elements in the exterior.
5. Calculate the normal distance between the surfaces, $e(I)$, as the sum of the undeformed distance and the normal displacement $u_z$

   $$e(I) = d(I) + u_z(I) = d(I) + \sum_{J=1}^{N}\left(A_{zJz}(x_I, y_I)\sigma_{zJ}\right) \tag{A.68}$$

   This gives N linear equations which have to be solved for $\sigma_z$. Once $\sigma_z$ is known $u_z$ can be determined.
6. For elements in the exterior: $\sigma_z(I) = 0$, for elements in the contact area: $e(I) = 0$. This gives N equations which can be solved for $\sigma(i,j)$.
7. For elements in the contact area: check if $\sigma_z(I) > 0$, if not place element in exterior and set $\sigma(I) = 0$ and return to point 5.
8. For elements in the exterior: check if $e(I) > 0$, if not place element in contact area and return to point 5.
9. Ready.

For engineering purposes it is enough to know that the algorithm has been proven empirically to always converge. Nevertheless a mathematical proof of convergence, using variational theory, can be found in Kalker's book [1].

To calculate the penetration from the normal force, introduce another unknown, the penetration depth, $d_p$. The algorithm works the same as described above except that in

the equation in point 3 $d(I)$ must replaced by $d(I)+d_p$, and that vertical balance of force is added to the equations:

$$F_n = \sum_{I=1}^{N} \sigma_z(I) \tag{A.69}$$

So in total there wil be $N+1$ linear equations for $N+1$ unknowns.

The algorithm for the tangential problem works very similar:

1. set $\sigma_{x,y} = 0$
2. initially all elements are assumed to be in adhesion
3. The slip is given as:

$$s_x(i,j) = c_x(i,j) + \frac{u_x(i,j) - u_x(i-1,j)}{\Delta x} V \tag{A.70}$$

$$s_y(i,j) = c_y(i,j) + \frac{u_y(i,j) - u_y(i-1,j)}{\Delta x} V \tag{A.71}$$

   where $c_x$ and $c_y$, are the rigid slip which can be calculate with the use of equations A.38 and A.39. $u_x$ and $u_y$ can be substituted using equations A.61 and A.62, so that the unknowns in this equations are $s_x$, $s_y$, $p_x$ and $p_y$. Note that in these equations $s$, $c$ and $u$ are written with the indices (i,j) i=1:n, j=1:m, n and m the number of elements in longitudinal and lateral direction respectively. This is done here to facilitate the derivatives in the equations above. However, the equations of the influence numbers are in vector form (with index I=1:N, N=n*m). It is therefore necessary to convert between the two notations (using the *reshape* function in Matlab). Alternatively a matrix could be constructed containing the element number of the neighboring elements for each element.

4. For elements in adhesion: $s_{x,y}(i,j) = 0$, whereas for elements in slip the magnitude of the tangential stress is proportional to the normal contact pressure and the direction of the tangential is the same but in opposite sense than the slip. This can be expressed using the following nonlinear equations:

$$\sqrt{\sigma_x(i,j)^2 + \sigma_y(i,j)^2} = \mu\sigma_z(i,j) \tag{A.72}$$

   and

$$\frac{\sigma_x(i,j)}{\sigma_y(i,j)} = \frac{s_x(i,j)}{s_y(i,j)} \tag{A.73}$$

   This gives 2N equations which combines with the equations in point 3 for a total of 4N equations for 4N unknowns: $s_x$, $s_y$, $\sigma_x$ and $\sigma_y$. As some of these equations are non-linear they need to be solved through an iterative procedure (e.g. the Newton-Raphson method.

5. For elements in the adhesion area: check if $\sqrt{\sigma_x(i,j)^2 + \sigma_y(i,j)^2} < \mu\sigma_z(i,j)$, if not place elements in slip area and return to point 3

A

6. For elements in the slip area: check if slip is in opposite direction than traction, if not place elements in the adhesion area and return to point 3

7. Ready.

Similar to the algorithm for the normal problem, an inverse algorithm exists for the tangential problem. In this algorithm one ore two of the creep forces are prescribed and the lateral and/or longitudinal creepage is sought. The alhorithm is structured the same as above. The rigid slip, $c$, in equations A.70 and/or A.71 remains function of $v_x$ and/or $v_y$ so that there are one or two unknowns in the equations to be solved in step 4. There are also one or two extra equations: the balance of force in longitudinal and or lateral direction:

$$F_{x,y} = \sum_{i=1}^{n} \sum_{j=1}^{m} \sigma_{x,y}(i,j) \tag{A.74}$$



### A.3.8. EXTENSION FOR CONFORMAL CONTACT

In conformal contact the contact area is not longer planar; therefore the following three aspects of the original Kalker full theory need to be reconsidered:

- The influence numbers in Kalker's full theory are based on the half-space assumption. Conformal contact is better approximated as a quarter space. Unfortunately the influence numbers for a quarter space cannot be calculated analytically; instead, finite element simulations can be used [2].

- The contact forces are obtained through integration of the contact stress, using the same equations as for the Stripes method (A.59 and A.60). Therefore the normal force will contain a frictional component and the lateral creep force will contain a component originating from the contact pressure. The lateral creep force and the normal contact become dependent on the location of the contact point through the contact angle in that point; however, the resultant force remains independent of the choice of reference point.

- The rigid slip can not longer be calculated with equations A.38 and A.39. Li [2] used the following equations:

$$c_{x_n} = V\left(v_{x0} + \frac{z_r - z_{r0}}{R_0} + y_n \sin\delta_l \Psi_{\text{kin}}\right) \tag{A.75}$$

$$c_{y_n} = V\left(v_{y0} - x\frac{\sin\delta_l}{R_0} - x\cos\delta_l \Psi_{\text{kin}}\right) \tag{A.76}$$

  Where $x$, $y$ are the x and y coordinates in a coordinate system following the surface of the rail, $z_r$ is the vertical coordinate, and $\delta_l$ is the local contact angle. However, the author of this dissertation suggest using the following instead:

$$c_x(x,y) = V\left(v_{x0} + \frac{z_y - z_0}{R_0} + (y - y_0)\Psi_{\text{kin}}\right) \tag{A.77}$$

$$c_y(x,y) = V\left(v_{y0}\frac{\cos\delta_0}{\cos\delta_l} - x\frac{\sin\delta_l}{R_0} + x\cos\delta_l \Psi_{\text{kin}}\right) \tag{A.78}$$

where y is the horizontal coordinate from the reference point and $\Psi_{kin}$ is the kinematic spin, which is zero for the case of a vehicle steady curving and proportional to the first derivative of the wheelset's yaw angle ($\dot{\gamma}$) otherwise ($\Psi_{kin} = \frac{\dot{\gamma}}{V}$). Here, the influence of the non-planar contact area on the kinematic spin has been accounted for. This influence is small as the kinematic spin is small anyway, but it comes at virtually no extra computational effort. Another factor is that the influence of the local contact angle on the lateral creepage is now accounted for.

Note that in the case $\Psi_{kin} = 0$ the equations above simplify to the equations from the Stripes methods A.57 and A.58.

## REFERENCES


[1] J. J. Kalker, *Three Dimensional Elastic Bodies in Rolling Contact* (Kluwer Academic Publishers, 1990).

[2] Z. Li, *Wheel-Rail Rolling Contact and its Application to Wear Simulation*, Ph.D. thesis, Delft University of Technology (2002).

[3] X. Zhao and Z. Li, *The solution of frictional wheel-rail rolling contact with a 3d transient finite element model: validation and error analysis,* Wear **271**, 444 (2011).

[4] X. Zhao and Z. Li, *A three-dimensional finite element solution of frictional wheel–rail rolling contact in elasto-plasticity,* Journal of Engineering Tribology **229**, 96 (2014).

[5] H. Hertz, *Über die berührung fester elastischer körper,* Journal für die reine und angewandte Mathematik **91**, 156–171 (1881).

[6] S. Iwnicki, *Handbook of railway vehicle dynamics* (Taylor and Francis, 2006).

[7] M. Sh. Sichani, R. Enblom, and M. Berg, *Comparison of non-elliptic contact models: towards fast and accurate modelling of wheel/rail contact,* Wear **314**, 111–117 (2014).

[8] J. Piotrowski and H. Chollet, *Wheel/rail contact models for vehicle system dynamics including multi-point contact,* Vehicle system dynamics **43**, 455–483 (2007).

[9] C. Linder, *Verschleiss von Eisenbahnrädern mit Unrundheiten*, Ph.D. thesis, ETH Zurich (1997).

[10] J. Ayasse and H. Chollet, *Determination of the wheel rail contact patch for semi-hertzian conditions,* Vehicle System Dynamics **43**, 159–170 (2005).

[11] Z. Y. Shen, J. K. Hedrick, and J. A. Elkins, *A comparison of alternative creep force models for rail vehicle dynamic analysis,* Vehicle System Dynamics **12**, 79–83 (1983).

[12] O. Polach, *A fast wheel-rail forces calculation computer code,* Vehicle System Dynamics **33**, 728 (1999).

[13] J. J. Kalker, *Rolling contact phenomena—linear elasticity,* Proceedings of the CISM International Centre for Mechanical Sciences **411**, 1–183 (2001).

[14] J. J. Kalker, *A simplified theory for non-hertzian contact,* Vehicle System Dynamics **12**, 43–45 (1983).

[15] J. J. Kalker, *A fast algorithm for the simplified theory of rolling contact,* Vehicle System Dynamics **11**, 1–13 (1982).

[16] J. Piotrowski and W. Kik, *A simplified theory of wheel/rail contact mechanics for non-hertzian problems and its application in railway vehicle simulations,* Vehicle System Dynamics **46**, 27–48 (2008).

[17] J. J. Kalker, *Rolling with slip and spin in the presence of dry friction,* Wear **9**, 20–38 (1966).

[18] J. J. Kalker, *The tangential force transmitted by two elastic bodies rolling over each other with pure creepage,* Wear **11**, 421–430 (1968).

[19] J. Boussinesq, *Application des potentiels à l'étude de l'équilibre et du mouvement des solides élastiques,* Gauthier-Villars **Paris** (1885).

[20] V. Cerruti, *Accademia dei lincei,* Mem. fis. mat. **Rome** (1882).

[21] G. M. L. Gladwell, *Contact problems in the classical theory of elasticity* (Sijthoff and Noordhoff, 1980).

# ACKNOWLEDGMENT

A PhD research is not possible without the support of many people.

First, I would like to thank my co-promotor, Zili Li, for his supervision. I am especially grateful for getting the opportunity to define the research topic and the chance to follow my ideas and for letting me teach. Further, I would like to thank my promotor, Rolf Dollevoet, for his support and feedback and prof. Molenaar to be my promotor in the first years.

Many thanks to Maider, Milli and Alfredo for the many lunch and tea discussions we had.

Further I would like to thank everyone involved in the PMnIDEA project, it taught me a lot about international cooperation. I am grateful to Jan Moraal for introducing me to nightly measurements on the track as well as the axle box acceleration measurements. Such experiences were not directly linked to my research, but gave me the opportunity to broaden my knowledge.

I also thank to staff of the Railway engineering group at TUDelft: Jacqueline, Jan-Willem, Marco, Jurjen, Zhiwei, Dirk, Valeri and Michael, and my office mates Xin, Shaoguang and Zilong, and my many current and former phd colleagues.

From outside Delft I would like to thank Matin and his supervisor for the fruitful cooperation with Stockholm, and Guillermo for our cooperation and for introducing me to Colombia.

Tenslotte wil ik mijn ouders, Erik en Friedi bedanken voor alle steun.

*Delft, November 2015*

# CURRICULUM VITÆ

## Nico BURGELMAN

13-10-1984 Born in Ghent, Belgium.

## EDUCATION

1996–2002 High school
Atheneum Mariakerke

2002–2005 Bachelor in Electromechanical Engineering
University Ghent

2005–2007 Master in Electromechanical Engineering
University Ghent

2008–2010 Master in Mechanics of Solids and Fluids
Chalmers University of Technology
*Thesis:* Tuning a Concrete Sleeper to Replace a Timber Sleeper: Study of Vertical Dynamics
*Promotor:* Prof. dr. J. Nielsen
Winner SWEDTRAIN's master thesis competition 2009

2010–2015 PhD at Department of Railway Engineering
Delft University of Technology

## WORK EXPERIENCE

2007 Trainee-ship in Khujand, Tajikistan, through the International Association for the Exchange of Students for Technical Experience (IAESTE)
2008 High school teacher for mathematics and physics (15-18 year old students)
2010 Researcher at Chalmers (continuation of the master thesis)
2015-... Specialist mechanics at Dekra Rail (Utrecht)

## SIDE WORK DURING THE PHD-PROJECT

| | |
|---|---|
| 2011 | Invited Speaker at 4th VIGrade users conference<br>"Influence of traction on lateral force in long trains" |
| 2012 | European project: PMnIDEA (key innovation 4, writing for deliverable 3.5)<br>Inspection technologies for the assessment of track quality<br>(focus on long wave track irregularities).<br>Partners: Mermec, D'Appolinia, ATAC and Politecnico di Milano. |
| 2013–2015 | Teaching and organizing practical sessions<br>for "Structural Design of Railway Track" (course code: CIE4870) |
| 2014 | Guest lecture: "How to reduce the cost of maintaining railway track"<br>for the Transport Institute at TUDelft |
| 2014 | Guest lecture: "General Introduction to Railways"<br>for a Spring course of Board of European Students in Technology (BEST) |
| 2014–2015 | Supervision (+member of the examination committee)<br>of the master thesis of Guillermo Alarcon:<br>"The influence of rail lubrication on energy dissipation in the<br>wheel/rail contact: A comparison of simulation results<br>with field measurements" |

# List of Publications

## Journal articles

5. **N. Burgelman**, Z. Li, R. Dollevoet, *Effect of the Longitudinal Contact Location Vehicle Dynamic Simulation*, Submitted for publication in Mathematical problems in Engineering.

4. **N. Burgelman**, Z. Li, R. Dollevoet, *Fast Estimation of the Derailment Risk of a Braking Train in Curves and Turnouts*, Accepted for publication in International Journal of Heavy Vehicle Systems.

3. G. I. Alarcón, **N. Burgelman**, J. Meza, A. Toro, Z. Li *The influence of rail lubrication on energy dissipation in the wheel/rail contact: A comparison of simulation results with field measurements*, Wear 330, 533-539 (2015).

2. **N. Burgelman**, M. Sichani, R. Enblom, M. Berg, Z. Li, R. Dollevoet, *Influence of wheel–rail contact modelling on vehicle dynamic simulation*, Vehicle System Dynamics 53, 1190-1203 (2015).

1. **N. Burgelman**, Z. Li, R. Dollevoet, *A new rolling contact method applied to conformal contact and the train–turnout interaction*, Wear 321, 94-105 (2014).

## Conference articles

5. C. Shen, Z. Wei, **N. Burgelman**, R. Dollevoet, Z. Li *Effects of wheelset flexibility on the simulation of vehicle-track interaction at crossings*, Proceedings of 24nd International Symposium on Dynamics of Vehicles on Roads and Tracks, Graz, Austria (2015).

4. G. I. Alarcón, **N. Burgelman**, J. Meza, A. Toro, Z. Li *The influence of friction coefficient and wheel/rail profiles on energy dissipation in the wheel/rail contact*, Proceedings of 10th International Conference on Contact Mechanics and Wear of Rail/Wheel Systems, Colorado Springs, USA (2015).

3. **N. Burgelman**, M. Sichani, Z. Li, R. Dollevoet, R. Enblom, M. Berg, *Comparison of wheel/rail contact models applied for online vehicle dynamic simulation*, Proceedings of 23nd International Symposium on Dynamics of Vehicles on Roads and Tracks, Qingdao, China (2013).

2. **N. Burgelman**, Z. Li, R. Dollevoet, *A new rolling contact method applied to train-turnout interaction*, Proceedings of 9th International Conference on Contact Mechanics and Wear of Rail/Wheel Systems, Chengdu, China (2012).

1. **N. Burgelman**, Z. Li, R. Dollevoet, *Some Preliminary Results in Simulation of Interaction between a Pushed Train and a Turnout*, Proceedings of 22nd International Symposium on Dynamics of Vehicles on Roads and Tracks, Manchester, UK (2011).

## THESES

2. **N. Burgelman**, *Concrete sleeper tuned to replace a timber sleeper*, Master Thesis, Chalmers University of Technology (2009).

1. **N. Burgelman**, *Studie en modellering van pull-out proeven*, Master Thesis, Ghent University (2007).